LUND UNIVERSITY

Laser-driven particle acceleration - Experimental investigations

Lindau, Filip

2007

[Link to publication](#)

Total number of authors:
1

Laser-driven particle acceleration

Experimental investigations

Filip Lindau

Doctoral Thesis
2007

Lund University

Cover: CR-39 detector plate showing energy-dependent beam direction of laser-accelerated protons.

ABSTRACT

This thesis describes experimental studies of laser-driven particle acceleration. With the focused intensity of today's high-power lasers exceeding $10^{18}\,\mathrm{W/cm^2}$, extremely high-gradient accelerators are possible. A number of experiments have been performed using two different laser systems, the Lund multi-TW laser and the Vulcan laser at CLF/RAL, UK, to study aspects ranging from laser system optimization and acceleration physics to detection and analysis methods.

In one series of experiments, electrons were accelerated in underdense plasmas. As an intense laser pulse propagates in the plasma, a large-amplitude plasma wave is driven up in its wake. The longitudinal electric field in this wake can exceed $100\,\mathrm{GV/m}$. Relativistic electrons, injected from the background plasma, surf on the wave. By carefully controlling acceleration conditions, such as plasma density, laser pulse duration and focusing, short bursts of $\sim 100\,\mathrm{MeV}$ electrons with a small energy spread ($\frac{\Delta E}{E} \sim 0.1$) were generated. Details of the acceleration mechanism were elucidated by studying the dependence of the electron beam on laser and plasma properties. It was found that for a range of plasma density–laser intensity combinations, quasi-mono-energetic beams are reliably produced. Using linearly polarized laser radiation, the spatial profile of the electrons acquires an elliptical shape that can be controlled by the direction of the laser polarization. This implies that there is a direct interaction between the laser pulse and the bunch of accelerated electrons, and that the electrons are originating from the small region occupied by the laser. It was also found that the contrast of the laser has a significant impact on the stability of the electron beam.

In a second series of experiments, protons and other ions were accelerated from solid foil targets, a few μm thick, irradiated by a high-power laser. Since the protons are not relativistic, a stationary potential is needed to accelerate them. This was accomplished by allowing electrons, heated by the laser, to establish an electrostatic sheath on the back surface of the target foil. The strength of this field amounts to TV/m, accelerating protons to MeV energies over a very short distance. The laser contrast was again found to be an important parameter in the acceleration. The pedestal of amplified spontaneous emission (ASE) preceding the main pulse launches a shock wave into the target that could potentially destroy the back surface. However, by controlling the level and duration of the ASE, a regime in which the back surface is plastically deformed by the shock wave can be established, leading to an energy-dependent

deflection of the proton beam. Using a plasma mirror to improve the contrast further, targets as thin as 20 nm were used for proton acceleration. The conversion efficiency and maximum proton energy were found to increase significantly for these thin targets. In another experiment, the scaling of the maximum proton energy was studied at extreme laser intensities. The maximum energy was found to have a square root dependence on the laser intensity, but with a much lower energy than predicted by previous 1D plasma expansion models. Heating the target removes the protons and leads to efficient acceleration of heavier ions. Properties of these accelerated ions, such as charge state, energy, etc., were experimentally characterized.

While not strictly a particle acceleration experiment, the final section of this thesis concerns a soft X-ray laser generated by transient excitation of ions in a laser-produced plasma. A technique called GRIP was employed to efficiently transfer energy to the desired ion charge state. The process involves setting up a smooth plasma gradient with one pulse, and pumping the plasma to population inversion with another pulse, impinging on the plasma at a grazing angle of incidence. The output energy of the soft X-ray laser was optimized with respect to a number of parameters. The details of high repetition rate operation of this laser were also studied, and the importance of the pointing stability of the driving lasers was established.

Populärvetenskaplig sammanfattning

Den snabba laserutvecklingen under de senaste tjugo åren har gjort det möjligt att alstra, och sedan förstärka, extremt korta laserpulser. När en sådan puls fokuseras till en mikrometerstor strålfläck, kan intensiteten överstiga $10^{18}\,\mathrm{W/cm^2}$. Elektroner som utsätts för de elektromagnetiska fälten i laserpulsen kommer då att accelereras till relativistiska hastigheter. Men fälten växlar hela tiden riktning, och är därför inte lämpade för riktad acceleration av laddade partiklar. Ett sätt att så att säga likrikta laserenergin är att använda ett plasma, d.v.s. en gas med fria elektriska laddningar. Ett plasma bildas automatiskt om ett strålmål placeras i närheten av laserfokus, eftersom all materia som där kommer i pulsens väg omedelbart joniseras. I ett plasma kan starka elektriska fält upprätthållas, något som kan utnyttjas för partikelacceleration. Jämfört med konventionella partikelacceleratorer, där man använder sig av radiovågor i resonanta kaviteter, kan man i ett plasma ha tusentals gånger starkare fält. Det innebär att en viss partikelenergi uppnås på en motsvarande kortare accelerationssträcka. Detta är en mycket värdefull egenskap, eftersom man idag behöver enorma anläggningar för att nå intressanta energier. Laseraccelererade partiklar har även andra unika egenskaper, så som pulslängder motsvarande den genererande laserns och mycket god strålkvalitet.

Arbetet bakom denna avhandling har varit inriktat på att använda multi-terawatt-lasern vid högeffektslaserfaciliteten, Lunds tekniska högskola, och Vulcan-lasern vid CLF/RAL, England, för att experimentellt studera acceleration av laddade partiklar.

Genom att använda olika strålmål kan olika typer av partiklar accelereras. Vid passage genom en gas kommer lasern att generera en plasmakanal, där det bildas en longitudinell våg som färdas med laserpulsen. På denna våg kan elektroner accelereras, likt en surfare på en havsvåg. Elektronerna kan nå energier överstigande $100\,\mathrm{MeV}$ på mindre än en millimeter. Om laserns och plasmats egenskaper omsorgsfullt kontrolleras, kan elektronerna koncentreras i en mycket kort puls med liten energispridning.

Genom att istället fokusera lasern på en mycket tunn folie av t.ex. aluminium, kommer en stråle av högenergetiska (MeV) protoner—som ju är 1836 gånger tyngre än elektroner—att emitteras från foliens baksida. Protoner kan inte accelereras direkt i en plasmakanal, eftersom de p.g.a. av sin stora massa är

för långsamma och bara skulle översköljas av vågen (jfr analogin med surfaren). När laserpulsen träffar folien, reflekteras den på ytan, och värmer samtidigt upp elektroner (till temperaturer motsvarande 10^{10} K) i det plasma som bildas där. Elektronerna åker rakt genom folien och kommer ut på baksidan. Där bildar de ett gigantiskt elektrostatiskt fält som i sin tur accelererar protoner eller andra positiva joner på ytan. Situationen liknar nu istället en skidåkare som åker nedför en mycket brant backe. Accelerationsprocessen har den egenskapen, att protonernas riktning blir parallell med ytans normal. Genom att deformera ytan med en chockvåg, som också genereras av lasern, kan protonernas riktning styras.

Slutligen har ett experiment med en röntgenlaser genomförts. Svårigheten att uppnå lasring ökar dramatiskt med kortare våglängd. Det beror på att livstiden för det exciterade tillståndet är starkt våglängdsberoende. Under många år har det krävts mycket stora lasersystem, med höga pulsenergier, för att erhålla lasring i röngenområdet. Det innebär stora kostnader och låg pulsrepetitionsfrekvens. Genom förbättrad pumpning har det nyligen blivit möjligt att använda kompakta system, som det vid högeffektslaserfaciliteten i Lund. I experimentet studerades bl.a. röntgenlaserns egenskaper vid en pulsrepetitionsfrekvens på 10 Hz.

List of Publications

This thesis is based on the following papers, which will be referred to by their Roman numerals in the text.

I **Laser-wakefield acceleration of monoenergetic electron beams in the first plasma-wave period**
S. P. D. Mangles, A. G. R. Thomas, M. C. Kaluza, O. Lundh,
F. Lindau, F. S. Tsung, Z. Najmudin, W. B. Mori, C.-G. Wahlström and
K. Krushelnick.
Phys. Rev. Lett. **96**, 215001 (2006).

II **Effect of laser contrast ratio on electron beam stability in laser wakefield acceleration experiments**
S. P. D. Mangles, A. G. R. Thomas, M. C. Kaluza, O. Lundh,
F. Lindau, A. Persson, Z. Najmudin, C.-G. Wahlström, C. D. Murphy,
C. Kamperidis, K. L. Lancaster, E. Divall and K. Krushelnick.
Plasma Phys. Control. Fusion **48**, B83 (2006).

III **On the stability of laser wakefield electron accelerators in the monoenergetic regime**
S. P. D. Mangles, A. G. R. Thomas, O. Lundh, F. Lindau, M. C. Kaluza,
A. Persson, C.-G. Wahlström, K. Krushelnick and Z. Najmudin.
Phys. Plasmas **14**, 056702 (2007).

IV **Particle acceleration using the Lund multi-terawatt femtosecond laser**
J. Mauritsson, C. Delfin, F. Lindau, V. Lokhnygin, K. Osvay,
A. Persson, A. Sjögren and C.-G. Wahlström.
*Atoms and Plasmas in Super-Intense Laser Fields, SIF, Bologna,
Conference Proceedings* **88**, 389 (2004).

V **Laser-accelerated protons with energy-dependent beam direction**
F. Lindau, O. Lundh, A. Persson, P. McKenna, K. Osvay, D. Batani and C.-G. Wahlström.
Phys. Rev. Lett. **95**, 175002 (2005).

VI **High-intensity laser-driven proton acceleration: influence of pulse contrast**
P. McKenna, F. Lindau, O. Lundh, D. Neely, A. Persson and C.-G. Wahlström.
Phil. Trans. R. Soc. A **364**, 711 (2006).

VII **Enhanced proton beams from ultrathin targets driven by high contrast laser pulses**
D. Neely, P. Foster, A. Robinson, F. Lindau, O. Lundh, A. Persson, C.-G. Wahlström and P. McKenna.
Appl. Phys. Lett. **89**, 021502 (2006).

VIII **Scaling of proton acceleration driven by petawatt-laser–plasma interactions**
L. Robson, P. T. Simpson, P. McKenna, K. W. D. Ledingham, R. J. Clarke, T. McCanny, D. Neely, O. Lundh, F. Lindau, C.-G. Wahlström and M. Zepf.
Nature Physics **3**, 58 (2007).

IX **Lateral electron transport in high-intensity laser-irradiated foils diagnosed by ion emission**
P. McKenna, D. C. Carroll, R. J. Clarke, R. G. Evans, K. W. D. Ledingham, F. Lindau, O. Lundh, T. McCanny, D. Neely, A. P. L. Robinson, L. Robson, P. T. Simpson, C.-G. Wahlström and M. Zepf.
Phys. Rev. Lett. **98**, 145001 (2007).

X **Influence of shockwaves on laser-driven proton acceleration**
O. Lundh, F. Lindau, A. Persson, P. McKenna, D. Batani and C.-G. Wahlström.
(2007) *Submitted to Phys. Rev. E.*

XI Comparison of forward and backward directed beams of low- and medium-mass ions driven by petawatt laser–plasma interactions

P. McKenna, F. Lindau, O. Lundh, D. C. Carroll, R. J. Clarke,
K. W. D. Ledingham, T. McCanny, D. Neely, L. Robson, P. T. Simpson,
C.-G. Wahlström and M. Zepf.
Manuscript in preparation.

XII Detection of short lived radioisotopes as a fast diagnostic for intense laser–solid interactions

R. J. Clarke, K. W. D Ledingham, P. McKenna, L. Robson,
T. McCanny, D. Neely, F. Lindau, O. Lundh, C.-G. Wahlström,
P. T. Simpson and M. Zepf.
Appl. Phys. Lett. **89**, 141117 (2006).

XIII Optimization toward a high-average-brightness soft-x-ray laser pumped at grazing incidence

K. Cassou, S. Kazamias, D. Ros, F. Plé, G. Jamelot, A. Klisnick,
O. Lundh, F. Lindau, A. Persson, C.-G. Wahlström, S. de Rossi,
D. Joyeux, B. Zielbauer, D. Ursescu and T. Kühl.
Opt. Lett. **32**, 139 (2007).

XIV Quantitative study of 10 Hz operation of a soft X-ray laser—energy stability and target considerations

F. Lindau, O. Lundh, A. Persson, K. Cassou, S. Kazamias, D. Ros,
F. Plé, G. Jamelot, A. Klisnick, S. de Rossi, D. Joyeux, B. Zielbauer,
D. Ursescu, T. Kühl and C.-G. Wahlström.
Manuscript in preparation.

Abbreviations

ASE	Amplified spontaneous emission
B field	Magnetic field
CCD	Charge-coupled device
CPA	Chirped pulse amplification
E field	Electric field
EMP	Electromagnetic pulse
EOS	Equation of state
FWHM	Full width at half maximum
GRIP	Grazing incidence pumping
ICF	Inertial confinement fusion
Linac	Linear accelerator
LWFA	Laser wakefield acceleration
MCP	Micro-channel plate
OAP	Off-axis parabola
OD	Optical density
PIC	Particle-in-cell
RCF	Radiochromic film
RF	Radio frequency
RFS	Raman forward scattering
SMLWFA	Self-modulated laser wakefield acceleration
TLD	Thermoluminescent dosimeter
TNSA	Target normal sheath acceleration
(S)XRL	(Soft) X-ray laser

CONTENTS

Papers

INTRODUCTION

Following the rapid development of short-pulse, high-power lasers during the past two decades, the intensity achievable in a focused laser beam can now be as high as $10^{21}\,\mathrm{W/cm^2}$. The corresponding peak electric field, $E_0 = \sqrt{2c\mu_0 I}$, reaches $10^{14}\,\mathrm{V/m}$. This extremely high field strength will exert very strong forces, and thus acceleration, on any charged particle in the laser focus. However, since this is an oscillating field, it is not directly suited for directed particle acceleration. By going through an intermediate step, and first transferring the laser energy to a plasma, the high energy density of the oscillating fields in the laser pulse can be put to use. If the plasma conditions are properly manipulated (in terms of density, gradient, temperature, charge state, etc.), the same laser can be used to generate beams of electrons (Chapter 3), protons and heavier ions (Chapter 4). Beams of coherent soft X-ray photons can also be produced from such manipulated beams of laser-produced plasmas, and although the main topic of this thesis is charged particle acceleration with lasers, an experiment using soft X-ray lasers is included (Chapter 5).

The driving forces for developing laser-driven accelerators can be summarized as: smaller, cheaper, better. Conventional accelerators, using RF electromagnetic fields in resonant cavities, are limited by the maximum accelerating gradient that can be achieved. At field strengths above $\sim 200\,\mathrm{MV/m}$, field ionization of the materials making up the accelerating structures becomes inevitable. Once started, the ionization grows quickly when the freed electrons hit the walls, and an arc discharge is produced. This basic limitation, and the fact that most interesting applications need high-energy particles, leads to the large-scale structures normally associated with high-energy accelerator facilities. For example, the main accelerator at the Stanford Linear Accelerator Center, SLAC, brings electrons up to $50\,\mathrm{GeV}$ energy after $3\,\mathrm{km}$ (Figure 1.1). Of course, size and cost go hand in hand, and extending the energy frontier beyond the upcoming $14\,\mathrm{TeV}$ at the CERN Large Hadron Collider (LHC), will be very expensive indeed.

In contrast, a plasma can support electric fields that are many orders of magnitude larger than those found in conventional accelerators, in principle allowing a correspondingly more compact accelerator to be built. For example,

Figure 1.1: Aerial view of SLAC. The linac is $3\,\mathrm{km}$ long (photo courtesy of Stanford Linear Accelerator Center).

on the back of thin foil solid targets irradiated by a high-intensity laser, electric fields of the order of several TV/m have been measured during laser–plasma experiments [1] (see also Paper IX). In these fields, ions can be accelerated to MeV energies over only a few μm. An attractive characteristic of laser-accelerated particle beams (in particular for protons), is the possibility of achieving very low emittance (i.e. good beam focusability) compared to conventional accelerators [2]. The lasers used have very short pulse durations (typically tens of femtoseconds) and the particle beams generated have the potential of becoming equally short. In Paper I a pulse duration for accelerated electrons of less than 25 fs was inferred.

A bonus with laser-driven acceleration is that laser pulses perfectly synchronized to the particles automatically become available. There are many experiments in which this is of considerable use, either as a pump or a probe. For example, synchronized pulses allow direct imaging of electric fields in a laser-produced plasma [3].

Some of the applications suggested for laser-based accelerators are fast ignition for fusion energy and proton therapy. In the fast ignition approach to inertial confinement fusion (ICF), a spark ignites the fusion burn in an already laser-compressed target. A laser-generated beam of high-energy protons or electrons could provide that spark with the required timing accuracy [4]. Proton cancer therapy is a very good way of treating tumors in sensitive areas, such as the brain. This is because protons do much less damage to surrounding tissue, than e.g. X-rays. Currently, very few hospitals, worldwide, can afford the cost of dedicated proton therapy facilities. However, if laser-baser proton acceleration could reach the required dose and particle energies, it would have considerable impact on the availability of radiation therapy.

1.1 Basic plasma physics

At the extreme levels of focused intensity delivered by high-power, short-pulse lasers, atoms are immediately ionized. All subsequent interactions between the electromagnetic wave and matter then takes place in an ionized medium, i.e. in a plasma. The field of plasma physics is huge and complex, and will not be covered in detail here (for more details, see the textbooks [5–8]). This section presents a few of the relevant basic concepts needed to understand particle acceleration. Note that SI units will be used throughout this thesis, unless otherwise explicitly stated.

In a cold, unmagnetized plasma the electrons oscillate at the electron plasma frequency. The electrostatic force from charge separation provides the restoring force. The oscillations do not set up a traveling wave, but rather act as a natural resonance frequency of the plasma [9],

$$\omega_p = \sqrt{\frac{q_e^2 n_e}{\varepsilon_0 m_e}}, \tag{1.1}$$

where q_e is the charge, n_e the number density and m_e the mass of electrons. Ions in the plasma have their own plasma frequency, depending on their charge state, number density and mass. At intensities below $\sim 10^{21}\,\text{W/cm}^2$, i.e. for all relevant laser conditions, the difference in mass between ions and electrons means that ion motion will be small.

The equation for the plasma frequency can be extended to conditions where the electrons have relativistic energies according to [10]

$$\omega_p = \sqrt{\frac{q_e^2 n_e}{\varepsilon_0 \langle \gamma \rangle m_e}}, \tag{1.2}$$

where

$$\gamma = 1/\sqrt{1 - \frac{v_e^2}{c^2}} \tag{1.3}$$

is the Lorentz factor, v_e is the electron velocity and c the speed of light in vacuum. $\langle \gamma \rangle$ denotes the cycle average of the motion.

The plasma frequency determines the index of refraction in the simplest case (cold, unmagnetized plasma) of electromagnetic wave propagation [9],

$$n = \sqrt{\mu_r \varepsilon_r} = \sqrt{1 - \frac{\omega_p^2}{\omega_0^2}} = \sqrt{1 - \frac{q_e^2 n_e}{\varepsilon_0 m_e \omega_0^2}}, \tag{1.4}$$

where ω_0 is the frequency of the wave. The value of n is less than unity, which means that the phase velocity, v_{ph} is given by

$$v_{ph} = \frac{c}{n} > c.$$

The group velocity of light propagating in the plasma

$$v_{gr} = \frac{\partial \omega}{\partial k} = c \sqrt{1 - \frac{\omega_p^2}{\omega_0^2}} \tag{1.5}$$

is, however, always less than c, although approaching it as the electron density is decreased. We will find this to be important when discussing electron acceleration in Section 3.3.

The expression for n leads to two different regimes, depending on the sign of $\left(1 - \omega_p^2/\omega_0^2\right)$. For $\omega_0 > \omega_p$, the refractive index is a real number, and the electromagnetic wave can propagate in the plasma. Due to the density dependence of ω_p, this condition is called an *underdense* plasma. When the reverse is true, i.e. $\omega_0 < \omega_p$, the refractive index becomes imaginary and the plasma is called *overdense*. A propagating wave is no longer supported by the plasma, and the wave is reflected at the boundary where the density is equal to the *critical density* and $\omega_0 = \omega_p$. This resonance condition leads to efficient coupling between the electromagnetic field and the plasma, as will be further discussed in Section 4.2. An evanescent wave extends into the plasma on a scale length called the skin depth,

$$l_s = \frac{c}{\omega_p} \left(1 - \frac{\omega_0^2}{\omega_p^2} \cos^2 \theta\right)^{-\frac{1}{2}}, \tag{1.6}$$

where θ is the angle of incidence [7]. At solid density, the skin depth for visible radiation is on the order of $10\,\text{nm}$.

The dependence of the plasma frequency on the relativistic electron mass makes it possible to increase the critical density for sufficiently intense laser pulses. In this way an overdense plasma can be effectively pushed into underdense conditions, transmitting the laser pulse in what is known as induced transparency [11]. For a wavelength of $800\,\text{nm}$ the critical density is $1.7 \times 10^{21}\,\text{cm}^{-3}$. In comparison, the atomic density (the electron density can be several times higher depending on the ionization stage) in most solids is $\sim 10^{23}\,\text{cm}^{-3}$.

As the Coulomb force is quite strong, large separation of charges in a plasma is efficiently suppressed. The average charge separation depends on the amount of kinetic energy available, i.e. the temperature. A characteristic length scale, the Debye length, is defined as the distance at which the electrostatic potential equals the thermal energy [5],

$$kT_e = \frac{q_e^2 n_e \lambda_D^2}{\varepsilon_0} \Rightarrow \lambda_D = \sqrt{\frac{\varepsilon_0 kT_e}{q_e^2 n_e}}. \tag{1.7}$$

For an electron temperature $kT_e = 1\,\text{MeV}$ and an electron density $n_e = 1 \times 10^{19}\,\text{cm}^{-3}$—typical values for underdense plasma experiments—the Debye length is $\lambda_D = 2.4\,\mu\text{m}$. At the critical density for $800\,\text{nm}$ light, $\lambda_D = 0.2\,\mu\text{m}$, i.e. much shorter than the laser wavelength.

Plasma expansion into the surroundings is often well described by an exponentially decreasing density distribution,

$$n = n_0 e^{-x/l}. \tag{1.8}$$

The characteristic length l is called the density *scale length* of the plasma and is defined as

$$l = n_e / \left|\frac{\mathrm{d}n_e}{\mathrm{d}z}\right|. \tag{1.9}$$

LASER SYSTEMS AND EXPERIMENTAL FACILITIES

2.1 Introduction

The acceleration experiments presented in this thesis have been carried out on two different laser systems, each described here. One is the multi-terawatt laser at the high-power laser facility in Lund, Sweden, and the other is the Vulcan laser at the Central Laser Facility (CLF) at the Rutherford Appleton Laboratory (RAL) in Oxford, England. They represent quite different types of lasers. The Lund laser has a high repetition rate and low pulse energy, while the Vulcan laser is a single-shot laser with high pulse energy. The ways in which the lasers are operated are also very different. The smaller Lund laser is directly handled by the researchers themselves, allowing complete control of all parameters. Testing different pulse durations, contrast levels, etc. is therefore easily done. At Vulcan, the laser is run by dedicated staff, adding an extra level between the experimenters and the laser.

2.1.1 Ultra-short pulses

The quest for higher laser intensities necessarily leads to attempts to decrease the laser pulse duration. As the duration is related to the inverse of the frequency bandwidth via a Fourier transform, the ideal is a laser with a large bandwidth. A laser oscillator cavity is resonant at integer multiples (longitudinal modes) of half the laser wavelength. To realize a short pulse, the modes also need to be locked in phase, hence the term mode locking. This can be achieved in different ways [12], but one of the more elegant is utilizing the Kerr lens effect. When the lasing modes are in phase, the resultant pulse is at its shortest, and thus the peak intensity its highest. The non-linear refractive index of the gain medium is intensity dependent, resulting in a higher index of refraction on axis. This acts as a lens, focusing the beam in the crystal and leading to a smaller beam diameter, with improved coupling to the pump volume.

The shortest pulse that can be generated is directly related to the width of the gain curve of the lasing medium. Titanium-doped sapphire is a material with one of the widest gain bandwidths, and has very good mechanical and thermal properties; it is therefore extensively used for short-pulse lasers.

2.1.2 Chirped-pulse amplification

When amplifying ultra-short laser pulses from a mode-locked oscillator, they soon reach intensities that could damage the optical components. Propagation of light with too high intensity through materials also induces non-linear effects, such as self-phase modulation, and degrades the beam quality. The intensity can be lowered by expanding the beam diameter, but this means that the optics have to be made larger by the same factor. The cost of optical components is very size dependent, and soon tends to become astronomical.

An alternative way of reducing the laser intensity, is to stretch the pulses in time. This can be done in a controlled way, by introducing a frequency chirp to large bandwidth pulses. After amplification, the pulses are recompressed to (almost) the same duration. The technique, originally used for radar applications, is referred to as chirped pulse amplification (CPA) [13]. The stretching and compression are usually achieved using dispersive elements, such as gratings [14].

The temporal structure of the linearly stretched pulse has the same shape as its spectrum. For a given stretcher configuration, the stretched pulse duration is determined by the bandwidth of the pulse. This can be of some concern; if the oscillator, for some reason, starts lasing with reduced bandwidth, the intensity impinging on the amplifier optics rises accordingly.

2.1.3 Amplified spontaneous emission

For a laser pulse to gain energy from an amplifier crystal, it must reach population inversion before the pulse arrives. As soon as the crystal is optically pumped, it starts emitting spontaneously. These photons become amplified in the same way as the main pulse and form undesirable background radiation. Careful timing of the pump lasers and fast pulse switching using Pockels cells are required to minimize the level of amplified spontaneous emission (ASE). Normal designs of CPA laser systems limit the ratio of the main pulse to ASE intensity to the order of 10^6–10^7.

2.1.4 Diagnostics

Useful diagnostic instruments for characterizing ultra-short laser pulses are power/energy meters, which measure the total pulse energy, and spectrometers which give the spectral bandwidth. The bandwidth determines the shortest pulse that can be obtained, but does not give the actual pulse duration. Normal measurement devices, such as power meters and photodiodes do not respond quickly enough to resolve the ultra-fast pulses generated by mode-locked lasers. Instead, various types of autocorrelation are used. The simplest type is the second-order autocorrelator. It can be used in single-shot mode—always

a great advantage—by splitting each pulse into two and combining them in a doubling crystal under a certain angle. The spatial width of the doubled light pulse then corresponds to the duration of the pulse. A drawback associated with second-order autocorrelation is that it gives a symmetric trace and cannot be used to determine prepulses or asymmetric temporal pulse profiles.

The solution is to use third-order autocorrelation. After splitting the beam, one part is doubled and then the two pulses overlapped in a tripling crystal. Since the pulses are not the same, it can be determined in which order they arrive and the trace does not have any time ambiguity. More energy is needed to give a signal than for second-order autocorrelation, and this type of autocorrelator is often of the scanning type. A very good signal-to-noise ratio can be achieved at the third harmonic and it is possible to obtain a dynamic range in excess of 10^{10} for this type of measurement.

It is very difficult to measure the intensity of a tightly focused high-power laser directly. Instead, the intensity is inferred from measurements of the pulse energy, duration, and beam profile at the focus. Beam profiling can be carried out either in the actual focal spot of the experiment, or with a separate, more idealized, focusing system. In both cases the beam must be heavily attenuated, and it can not be guaranteed that the beam quality will be retained when returned to its full energy. A high dynamic range is desirable for the camera recording the focal intensity distribution in order to determine the amount of energy outside the central spot.

2.2   The Lund multi-TW laser

The multi-terawatt Ti:sapphire femtosecond laser at the Lund high-power laser facility has been used for many of the experiments described in this thesis. The laser is based on CPA, has a central wavelength of 800 nm, 10 Hz repetition rate and can deliver up to 1 J on target in 35 fs. In this section the laser system is described in some detail. Figure 2.1 shows a schematic of the laser system including the major components.

2.2.1   Amplification chain

The broadband, Kerr-lens mode-locked Ti:sapphire oscillator generates an 80 MHz train of short, ~ 20 fs, pulses. It is pumped at 532 nm by a 5 W CW solid state laser. Before entering the stretcher the pulse train is modulated by an acousto-optic dispersive filter, a Dazzler from the French company Fastlite. It acts as a programmable, wavelength-dependent, diffractive element by sending an RF acoustic wave through an acousto-optic crystal, where the RF standing wave pattern creates a volume Bragg grating. A grating-based stretcher, with 10 % throughput, lengthens the pulses by 10 ps/nm, so a pulse with 30 nm bandwidth becomes 300 ps.

One pulse is selected from the pulse train leaving the oscillator every 0.1 s for further amplification in three steps. The three amplifiers each have a Ti:sapphire crystal, pumped by frequency-doubled, flashlamp-pumped, Nd:YAG lasers. All of the amplifiers are driven to saturation in order to minimize unnecessary pulse-to-pulse energy fluctuations. These fluctuations are then limited by the
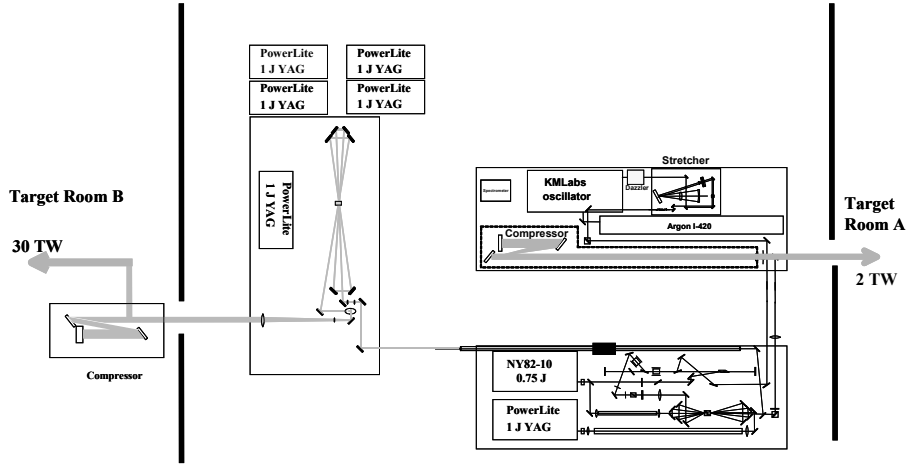
Figure 2.1: A schematic overview of the Lund multi-TW laser system.

Figure 2.2: A photograph of the final amplifier of the multi-TW laser system when pumped by 5 frequency-doubled YAG lasers, each giving 1 J. The Ti:sapphire crystal is inside the housing of the cryogenic cooler.

energy stability of the Nd:YAG lasers, $\sim 10\,\%$. After each amplifier, the beam diameter is expanded by a telescope to avoid self-phase modulation and damage to the optics.

The first step is a regenerative (regen) amplifier—a switchable optical cavity—which provides the bulk of the gain. The pulse energy is increased from tens of pJ up several mJ after ~ 11 round trips in the regen cavity. Fast Pockels cells switch the pulse to be amplified in and out of the cavity. Weak prepulses originate from the finite extinction ratio of the Pockels cell polarizers (typically 10^3:1), leading to the reflection of a small part of the pulse in each round trip in the cavity. Two extra Pockels cells follow the regen amplifier to suppress these prepulses and also to remove most of the ASE produced in the amplifier.

The second amplifier is of the multi-pass type, where the pulse to be amplified is directed through the Ti:sapphire crystal several times by means of an array of mirrors. Small angles between the different passes are needed to efficiently extract the pump energy. This limits the usefulness of the multi-pass design to a few passes (~ 6). After the first multi-pass amplifier, the pulse energy is $300\,\mathrm{mJ}$ and the beam is split into two. One part, containing $\sim 200\,\mathrm{mJ/pulse}$, is sent to a compressor for use in experiments not needing the highest laser powers (such as high harmonic generation, laser-produced X-rays, etc.).

To improve the beam quality of the remainder, the pulses are sent through a conical glass spatial filter. A final multi-pass amplifier then increases the pulse energy to $1.5\,\mathrm{J}$. The amplifier crystal is pumped by $5\,\mathrm{J}$ of green light at $10\,\mathrm{Hz}$, i.e. $50\,\mathrm{W}$ average power, leading to a significant thermal load. Since the refractive index of the crystal is temperature dependent, and the pump profile has a maximum at the center, a thermal lens is created. These problems are solved by cryogenic cooling of the crystal down to $100\,\mathrm{K}$, a temperature at which sapphire has very good thermal conductivity. Temperature gradients in the crystal are then effectively eliminated, allowing the output energy of the laser to be varied by simply changing the amount of pump energy. Finally, the beam is expanded to $50\,\mathrm{mm}$ diameter and a grating compressor, with $\sim 65\,\%$ throughput and placed in a vacuum chamber, restores pulse duration to $35\,\mathrm{fs}$. The peak power is then $\sim 30\,\mathrm{TW}$.

2.2.2   Contrast control

Thin-foil solid-target experiments, such as those discussed in Papers V–XII, are very sensitive to prepulses and ASE preceding the main laser pulse. As soon as the radiation level reaches above $\sim 10^{11}$ W/cm^2, the target material starts to ionize and a plasma is formed. The radiation ablates the surface and a shock wave is launched into the bulk by the reaction force. If the shock wave has a high enough amplitude when it reaches the back surface of the target, it will be vaporized, ruining the steep density gradient required for efficient proton acceleration [15, 16].

In view of this, we have devoted considerable attention to eliminating any prepulses and to gaining control of both the duration and level of the ASE generated by the laser system. A total of three Pockels cells are employed in
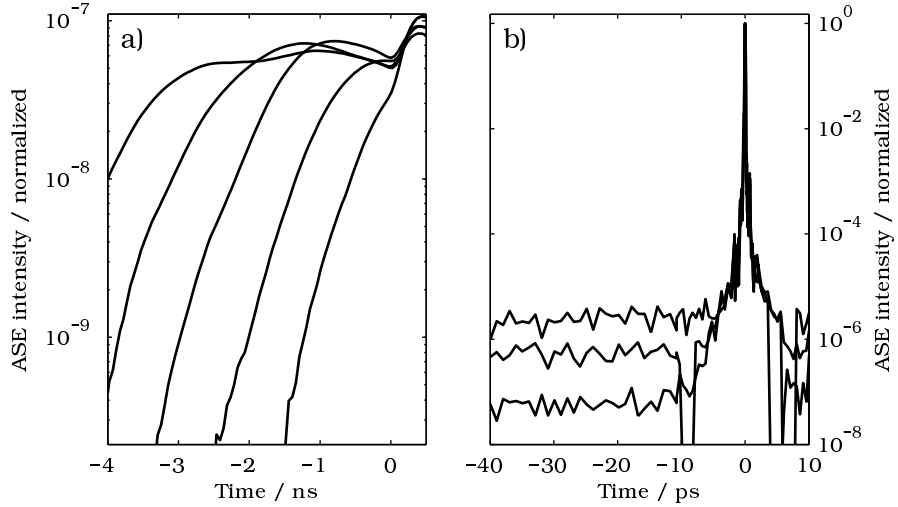
Figure 2.3: a) Typical shape of the ASE intensity on a ns timescale for four different timings of the Pockels cells, corresponding to 1–4 ns ASE duration. The measurements were performed with a fast photodiode and oscilloscope and normalized to a third-order autocorrelation scan. b) ASE shape on a ps timescale for three different seed energies to the regen amplifier. The ASE intensity is controlled over more than one order of magnitude and was measured with a high-dynamic-range third-order autocorrelator.

the amplification chain, removing any prepulses on the nanosecond timescale. The rise time of the drivers of these Pockels cells is around 1 ns, so by adjusting the timing relative to the main pulse, it is possible to control the duration of the ASE in the range 1–4 ns. The upper time limit is given by the duration of the high-voltage pulse switching the Pockels cells.

The bulk of the ASE is generated in the regen amplifier, and to minimize it, the seed beam must be carefully aligned so as to overlap the optical axis of the cavity. Also, the higher the seed energy, the more efficiently the stored energy in the gain medium can be extracted. In fact, the amount of ASE is found to depend linearly on the seed energy to the regen amplifier. This can be used to directly control the ASE level, and is particularly simple with the Dazzler. The diffraction efficiency of the crystal is determined by the amplitude of the acoustic wave, and this parameter is software controlled. Figure 2.3 illustrates the effectiveness of the ASE control, both in terms of duration and amplitude. Even with a perfectly aligned laser, the contrast is in the range of 10^8:1. One way to further improve the contrast is to use a plasma mirror; this is discussed in more detail in Section 4.5.1.
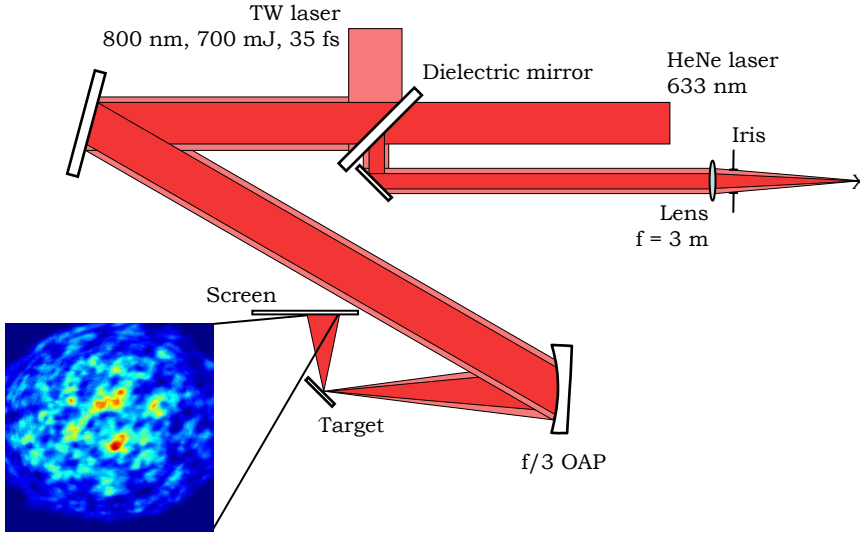
Figure 2.4: Experimental setup for ensuring on-target focus. Red light from a HeNe laser is inserted into the beam path through a dielectric mirror and made co-axial with the main IR beam (the beams have been drawn with different diameters for illustrative purposes). The speckle pattern (the inset showing a typical example) originating from target irregularities is projected onto a screen.

2.2.3 Focusing

In experiments on laser-driven proton acceleration, the laser is fired onto a thin (a few μm) target foil. The conversion of laser energy to proton energy is highly intensity dependent. This means that tight and accurate focusing is required to ensure repeatability in the experiments. With f/3 optics, the Rayleigh range, λ_R, (i.e. the distance from the focal plane to the point at which the area of the beam has doubled [12]) is only $10\,\mu$m. A number of specific problems are encountered when designing the focusing aid for experiments with such thin foils. The laser burns a hole in the target, so the target has to be repositioned for every shot. Since the target surface is in general not perfectly flat, it is necessary to focus locally where the shot is to be taken. As the target has a thickness of only a few tens of μm or less, it is fragile, and a contact-free means of measurement is required.

One approach to the focusing problem is to image backscattered light from the focal spot [17]. This requires meticulously aligned optics to ensure reliable positioning. For the proton acceleration experiments using the Lund multi-TW laser, we instead used the speckle pattern formed by laser light reflected from the target surface, which is typically uneven on the scale of the laser wavelength. It is well-known that the size of individual speckles in the speckle pattern grows as the illuminated spot becomes smaller. This is because the number of surface

Figure 2.5: Pictures of the speckle pattern a) in focus and b) after focus, for a $6\,\mu$m thick aluminium target. In c), the graph generated by the analysis software is shown.

structures contributing to the interference pattern also becomes smaller, and the far-field pattern is given by the 2D Fourier transform of the ra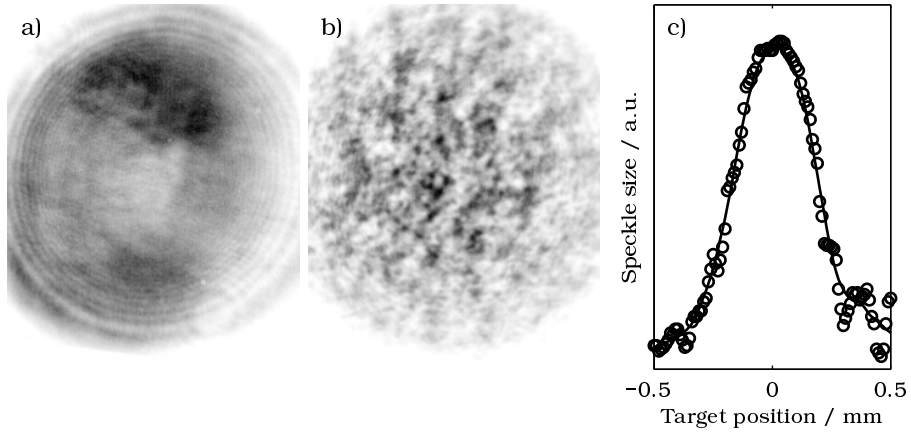diation field at the surface. If the spot size is smaller than the scale of the unevenness of the surface, only a single large speckle will be seen. The speckle method has its greatest advantage in that the optimum focus is found without the need for additional optics. It does, however, not work if the target surface quality is very high.

To create a visible speckle pattern, an expanded and collimated 633 nm HeNe laser beam is injected into the beam path through a dielectric mirror. It is co-axial with the 800 nm beam and both are focused by an off-axis parabolic mirror to the same spot on the target (see Figure 2.4). Alignment of the two beams is checked using infrared light leaking through the dielectric mirror and HeNe light reflected from the same surface. The HeNe laser is reflected from the target surface and a speckle pattern projected on a screen. A charge-coupled device (CCD) camera images the pattern and sends it to a computer for analysis. During the focusing procedure, a stepper motor moves the target through the focus, and a sequence of images is captured.

It is possible to find the position of best focus with an accuracy of $\sim$ 50–150 μm by eye, depending on the target material. Greater accuracy and reproducibility are achieved with computer analysis of the speckle images. An algorithm is applied to each image, generating a number that depends on the distance from the focus. We have used the ratio of low-frequency components to the whole frequency content of the Fourier transform of the image. This ratio will be higher at a position close to the focus (with a few large speckles), than at a position far from the focus (with many small speckles). However, over a considerable range near the focus (50–100 μm depending on target surface quality), the algorithm returns a rather noisy plateau (see Figure 2.5). The position at which the algorithm returns the maximum value is consequently

not necessarily the point of optimal focus. Additional positioning accuracy is instead obtained by fitting an analytical curve to the measured numbers. In this case, we estimate that the target can be reproducibly placed within $10 \, \mu$m of the true focus.

It is difficult to find an analytic curve to fit the data points generated by the algorithm. Close to the focus, there are only a few speckles and statistical models of the speckle power spectrum collapse. Far from the focus, the speckles become so small that they cannot be resolved by the CCD camera. However, since we are only interested in finding the position of maximum speckle size, a polynomial fit is sufficient.

Positioning a new target at the best focus with the present system takes a little less than a minute. This was not a serious issue in the experiments presented in this thesis, since each experimental run typically consisted of only around 20 shots. Focusing times of less than 10 seconds should by achievable by optimizing the algorithm and upgrading the computer.

2.2.4 The interaction chamber

The experiments are set up in a cylindrical vacuum chamber, 1.2 m in diameter and 0.4 m in height. A number of 250 mm diameter ports are located around the chamber. To expand the environment, smaller chambers can be docked onto these ports. The vacuum level, maintained by turbo pumps, is in the range of 10^{-4}–10^{-6} mbar. The mean free path of the gas is then 1–100 m, and collisions between accelerated particles and background molecules can be neglected.

2.3 The Vulcan laser and its target areas

The Vulcan laser is a Nd:glass laser, which has been extensively upgraded over the years. It has been modified to run in CPA mode, with up to 500 J per pulse at 500 fs pulse duration (that is, 1 PW). Around 8 shots are typically fired in a day. To increase the availability, there are two different target areas, called Target Area West (TAW) and Target Area Petawatt (TAP). Experiments can run simultaneously on both target areas, each taking alternating shots. Some of the amplifiers for the lasers are shared, but there are differences, which will be described briefly here.

TAW is the more versatile target area. It can use two short-pulse beams (one is operated with reduced energy) with a maximum of 100 J pulse energy and 1 ps duration (100 TW). Up to six long-pulse (ns timescale), high-energy beams are available for back-lighting and pump–probe experiments, etc. Apart from the oscillator being Ti:sapphire, the whole amplification chain is based on Nd:glass [18].

TAP is geared towards ultra-high-intensity experiments. After a Ti:sapphire-based oscillator, the first set of amplifiers is based on optical parametric chirped pulse amplification (OPCPA) in BBO crystals. The reason for not having a pure Nd:glass system is that gain narrowing would not permit the required 500 fs pulse duration [19]. The OPCPA amplifiers provide a large bandwidth for the rest of the chain of rod and disc amplifiers, which are shared with the TAW. The final stage consists of 208 mm disc amplifiers from the old
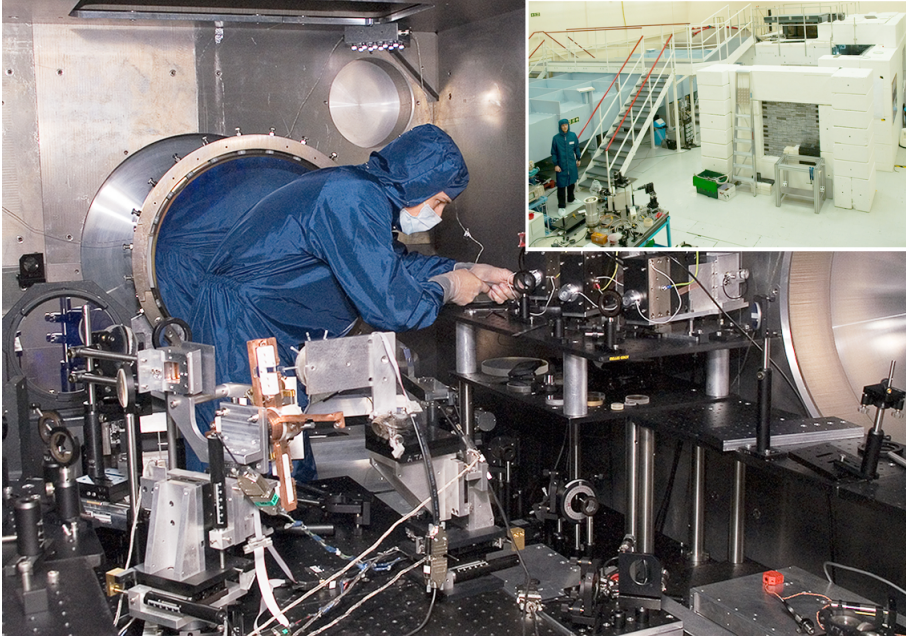
Figure 2.6: The Vulcan PW target chamber is large enough that people can walk in for experiment setup and access. Clean room attire is worn due to the expensive nature of 1 m diameter optics. The inset is an outside view of the target chamber with the concrete radiation shielding. The tank at the back houses one of the compressor gratings.

NOVA laser. Adaptive optics improve the phase front of the beam and makes it possible to reach an almost diffraction-limited spot size at the focus. The intensity there can be up to 10^{21} W/cm^2. At the very high energy levels encountered here, huge diameter optics are needed to avoid damage. Thus, the compressor gratings and f/3 off-axis parabolic mirror are 1 m and 0.6 m in diameter, respectively. Both TAW and TAP have been used for the experimental work in this thesis.

2.4 Radiation safety

Radiation hazards must be addressed when dealing with ultra-high focused intensities. Immediately after a shot is fired at a solid target, a burst of gamma rays is emitted together with high-energy electrons, protons and possibly even neutrons. The charged particles produce bremsstrahlung when they hit surrounding materials. Secondary neutron emission and activation of the experimental chamber are also possible as a result of the interaction. The main mechanism is (p,n) reactions (with Q-values in the range ~ 5 MeV), with some contribution from (γ,n).

Due to the difference in pulse energy between the Lund and Vulcan laser

systems, the level of radiation protection required differs substantially. The bremsstrahlung is emitted in a narrow cone in the direction of the accelerated particles. The dose here can reach dangerous levels, even for the Lund multi-TW laser. In the opposite direction, the radiation from a single shot is minimal and people can safely remain in the room during shots. To monitor the dose received, personal radiation badges in the form of thermoluminescent dosimeters (TLDs) are worn by all experimenters. However, if experiments were to be run at 10 Hz repetition rate for extended periods of time, the level of radiation shielding would have to be reassessed.

At Vulcan PW, the situation is quite different, and the target chamber is surrounded by 15 cm lead and 60 cm concrete to offer shielding from gamma rays and high-energy electrons. A 10 cm thick layer of high-density polyethylene plastic offers protection against neutrons. Careful selection of materials used in the experimental setup helps reduce the post-shot radiation level. Elements producing nuclides with medium duration half-lives (a few minutes) through (p,n) reactions should be avoided due to the high induced activity on the timescale of chamber access. Some examples of such reactions are: $^{63}\text{Cu}\,(\text{p, n})\,^{63}\text{Zn}$ ($T_{1/2} = 38.5\,\text{min}$), $^{52}\text{Cr}\,(\text{p, n})\,^{52}\text{Mn}$ ($T_{1/2} = 21.1\,\text{min}$) and $^{62}\text{Ni}\,(\text{p, n})\,^{62}\text{Cu}$ ($T_{1/2} = 9.7\,\text{min}$) [20]. Nuclear activation is not only a potential problem, but can also be used as a diagnostic for accelerated particles, mainly protons, as described in Paper XII.

ELECTRON ACCELERATION EXPERIMENTS

3.1 Introduction

Laser-driven electron acceleration is closely connected to underdense plasma, gas-target experiments. The lower electron density compared to solid targets permits the laser to propagate in the plasma, exciting a traveling plasma wave—a wave with a longitudinal electric field and phase velocity close to the speed of light. This is almost the ideal accelerating structure for relativistic particles and also the explanation why protons are not as easy to accelerate; they need to be injected at $\sim 1\,\text{GeV}$ (compared to $\sim 1\,\text{MeV}$ for electrons) in order not to be overtaken by the wave. An underdense plasma has the additional advantage of not being as instability prone as an overdense plasma, leading to less fluctuation and better control. Furthermore, the lower electron density makes simulations more tractable.

This chapter first presents some theory on electromagnetic wave propagation through underdense plasmas and plasma wave structures of interest in electron acceleration. It then details the experimental approach taken for investigating and optimizing the acceleration process. Finally, the results from these investigations are presented and discussed.

3.2 Propagation in an underdense plasma

3.2.1 Ionization

For ultra-high intensity lasers, the rising edge of the pulse, and possibly even the ASE have high enough intensity to ionize the target medium. This means that the peak of the pulse is always interacting with a preformed plasma. The primary ionization mechanism is multiphoton ionization at these intensities and pulse durations. Helium gas, the target medium for the electron acceleration experiments described in this thesis, has an appearance intensity for He^+ in the

range of $1 \times 10^{15}\,\mathrm{W/cm^2}$ [21]. This is probably too high for pre-ionization by the ASE pedestal for normal laser conditions (10^7 intensity contrast, $10^{19}\,\mathrm{W/cm^2}$ peak intensity). However, small impurities of, for example, nitrogen will lower the ionization threshold by about one order of magnitude, and a low-density plasma could be created by ASE. The laser heats the plasma and collisions will then transfer energy to the helium atoms and ionize them on a ns timescale. When the main pulse arrives, the plasma has had time to expand. This may be of some concern, as will be shown in Section 3.5.2.

3.2.2   The ponderomotive force

An electron starts to oscillate when subjected to the electromagnetic field of a laser. The cycle-averaged kinetic energy is given by (for linearly polarized light) [22]

$$U_p = m_e c^2 \left(\sqrt{1 + \frac{\mu_0 q_e^2 I}{m_e^2 c \omega_0^2}} - 1 \right), \qquad (3.1)$$

where U_p is known as the ponderomotive energy, q_e and m_e are the electron charge and rest mass, respectively, I is the peak intensity in the laser pulse, ω_0 the central frequency of the laser and μ_0 the permeability of vacuum. In the non-relativistic limit ($U_p \ll m_e c^2$),

$$U_p = \frac{\mu_0\, c\, q_e^2\, I}{2 m_e \omega_0^2} \propto I \qquad (3.2)$$

and in the highly relativistic limit ($U_p \gg m_e c^2$),

$$U_p = \frac{q_e c}{\omega_0} \sqrt{c \mu_0 I} \propto \sqrt{I}. \qquad (3.3)$$

For a typical intensity of $3 \times 10^{19}\,\mathrm{W/cm^2}$, $U_p = 1.5\,\mathrm{MeV}$. This means that the electrons oscillating in the electromagnetic field are highly relativistic (the rest mass of an electron is $511\,\mathrm{keV}$). In a homogeneous field, no net momentum would be gained by the electron, as it returns to the oscillation center after each cycle. In a laser focal spot, the field distribution is far from homogeneous (often it is some sort of gaussian). Oscillating electrons then experience a weaker Lorentz force at the endpoints of the trajectory, and do not quite return to the same position. They drift outwards to lower field regions, experiencing a gradient force according to $f_p = -\nabla U_p$. The expression can be derived for weak fields [23], but remains valid for relativistic field strengths by the inclusion of the relativistic electron mass γm_e, provided several conditions are met [24, 25]. In particular, there must be a center of oscillation, so for sufficiently tight focusing, the expression breaks down and electrons will be accelerated from the focal region in less than an optical cycle. The effect of the ponderomotive force is to expel electrons from the focal region of the laser, leaving a positively charged cloud of ions behind. Ions, with mass m_i, are also affected by the ponderomotive force, but the resulting acceleration is a factor m_i/m_e weaker, and ions can be regarded as stationary in most cases.

3.2.3   Self-focusing

For efficient electron acceleration, it is imperative that the laser pulse remains at high intensity for an extended distance. When focusing a laser beam, it normally quickly expands after the focal spot due to diffraction. A measure of the length of the focus is the Rayleigh range, λ_R. Various self-focusing effects during pulse propagation in a plasma, described briefly here, help to prevent this. A comprehensive summary of the encountered phenomena is given in [26, 27]. When a high-power laser beam is focused, the medium will start to ionize at some intensity. The refractive index of a plasma decreases with increasing level of ionization. This can be seen in Eqn 1.4 as the dependence of n_e on the refractive index. The beam usually has an intensity maximum on axis, giving rise to a radially decreasing charge density and thus defocusing of the beam [7]. To minimize the influence of ionization defocusing, which is a problem before the pulse has reached the focus and highest intensity, a sharp change in gas density is desirable. Defocusing can thus be avoided and the gas is exposed to the full intensity of the focused laser.

At higher intensities, the plasma is fully formed. The refractive index is then determined by the local plasma frequency according to Eqn 1.1. When the ponderomotive force "pushes" electrons away from the central part of the beam (electron cavitation), the charge density is lowered, and the beam is self-focusing.

An additional focusing effect is present at sufficiently high laser intensities (around $1 \times 10^{18} \, \text{W/cm}^2$). The electrons then acquire relativistic energies when oscillating in the laser field. Relativistic mass increase reduces the plasma frequency and a refractive index maximum results on the laser axis (see Figure 3.1). This is known as relativistic self-focusing [26, 28]. The effect can be strong enough to balance diffraction and, as a consequence, the laser spot can remain small over many Rayleigh ranges, forming a channel. A typical example can be seen in Figure 3.2. The condition for a relativistic channel to form is, to first order, a laser power exceeding a critical value,

$$P_c = 8\pi\varepsilon_0 c \left(\frac{m_e c^2}{q_e} \right)^2 \frac{\omega_0^2}{\omega_p^2} = 17.4 \frac{n_c}{n_e} \, \text{GW} \qquad (3.4)$$

For a typical electron density $n_e = 1 \times 10^{19} \, \text{cm}^{-3}$ and $\lambda_L = 800 \, \text{nm}$, this translates into $P_c = 3 \, \text{TW}$, a value well within reach of many ultra-fast lasers. The formation of the relativistic lens is not instantaneous, meaning that the leading edge of the laser pulse will be diffracted away as it propagates [29, 30].

If there are inhomogeneities in the plasma or in the laser beam profile, these can cause self-focusing of different parts of the beam separately. The result is filamentation of the beam, with a number of beamlets [31].

3.3   Wakefield acceleration

A high-intensity laser pulse "plows" through the plasma medium, with the ponderomotive force pushing electrons out of the focal region. The restoring force resulting from the electrostatic attraction of the ions left behind sets up
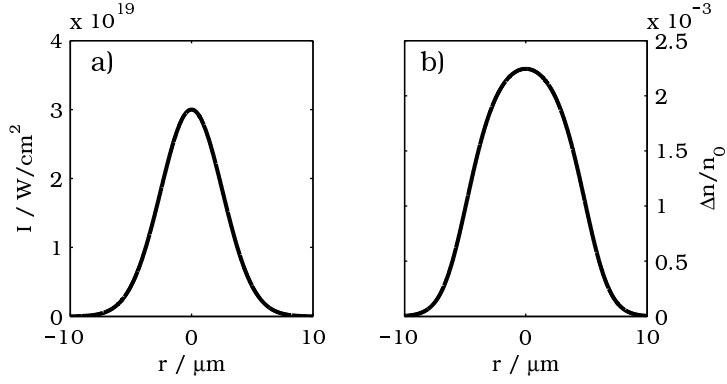
Figure 3.1: Relativistic focusing. The gaussian laser intensity profile in a) gives rise to the refractive index profile in b), assuming homogeneous plasma density. This is not a good assumption in the general case, as the ponderomotive force pushes electrons away from the high-intensity region.
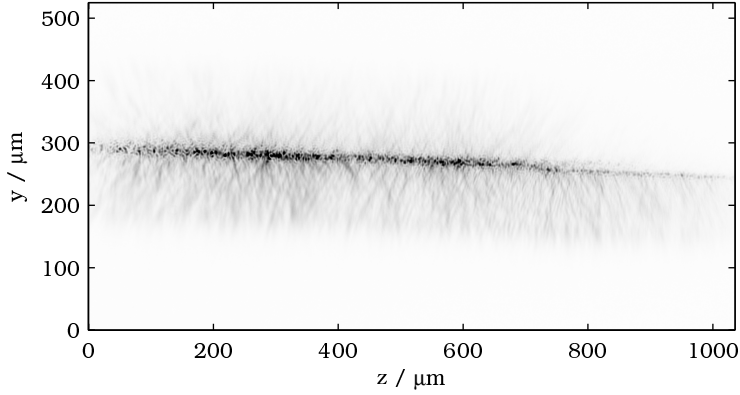
Figure 3.2: Relativistic channel as seen in Thomson-scattered laser light. The small-scale structures are resolution elements of the imaging optics, and the streaks a diffraction effect. The laser beam is traveling from left to right. FWHM of the channel is $15\,\mu$m and the plasma wavelength, λ_p, is $8\,\mu$m. The $1\,$mm length of the channel corresponds to $10\lambda_R$. The image was taken during the experiment described in Paper I.

Figure 3.3: The ponderomotive force of the laser pulse (located at around $z = -10\,\mu$m in the figure, traveling rigth) pushes electrons out of the focal region. The el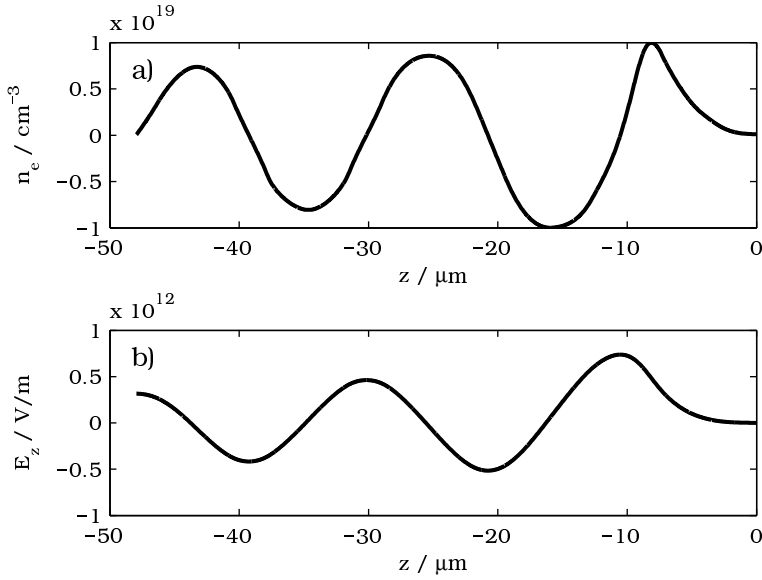ectrostatic restoring force resulting from the ions sets up an oscillating density variation, as illustrated in a). The longitudinal electric field resulting from this charge density distribution is depicted in b). The peak field strength is approaching $1\,$TV/m.

an oscillating charge density in the wake of the laser. The process is illustrated in Figure 3.3. The resulting potential structure is a plasma wave that travels behind the laser pulse. The phase velocity, v_{ph}, of the plasma wave is equal to the group velocity, v_{gr}, of the laser pulse, and the wavelength of the plasma wave $\lambda_p = 2\pi\, v_{gr}/\omega_p$. Electrons injected into this plasma wave can be accelerated to high energies, as first suggested by Tajima and Dawson in 1979 [32].

The generation of the wave is more efficient when the plasma wavelength is greater than the length of the laser pulse ($\lambda_p > c\tau_L$) so that it fits within the first period of the plasma wave, a condition known as the laser wakefield accelerator (LWFA) regime. If the laser pulse is longer than the plasma wavelength, the potential structure of the wave will overlap the laser pulse and start to modulate it via the Raman forward scattering (RFS) instability [33]. The electromagnetic wave will then eventually evolve into a train of pulses, each λ_p long [34, 35]. This is called the self-modulated laser wakefield accelerator (SMLWFA) regime. A drawback of SMLWFA is that the first plasma period is less efficiently excited, so that several periods can attain large amplitude. This is of critical relevance for the generation of narrow-energy-spread electron beams. On the other hand, for LWFA, relativistic self-focusing becomes less effective, and guiding of the laser pulse over longer distances becomes difficult.

3.3.1 Injection and wave breaking

The plasma wave is capable of supporting very high field strengths before breaking. However, the amplitude of the wave may eventually become high enough for electrons taking part in the oscillations to be caught by the next period in the wave structure and subsequently accelerated [36]. This longitudinal wave breaking leads to a (cold) limit of the electric field in the wakefield [37]:

$$E_m = \frac{m_e c \, \omega_p}{q_e} \sqrt{2(\gamma_{ph} - 1)}, \quad \gamma_{ph} = 1/\sqrt{1 - (v_{gr}/c)^2}. \tag{3.5}$$

γ_{ph} is the Lorentz factor associated with the plasma wave. Wave breaking can also take place transversely to the direction of propagation [38]. In this case it is the increasing curvature of the wings of the potential structure that collapses the wave. The limiting electric field in this case is smaller than that predicted by Eqn 3.5.

Injection by means of an external accelerator is also possible [39], but is experimentally difficult. Hitting the micron-sized plasma wakefield presents a considerable technical challenge, in terms of both spatial and temporal overlap.

3.3.2 Dephasing

When the wave breaks, the injected electrons are accelerated by the plasma potential. However, since the plasma wave is traveling at the group velocity of light, v_{gr}, in the medium—which is always less than c—the electrons will eventually outrun the wave. This is referred to as dephasing. It will decelerate the electrons and also increase their energy spread. This means that it is important to terminate the plasma wave, for example, by selecting a suitable length of the gas medium, before the electrons have dephased.

The dephasing length is given by

$$l_{dph} = \frac{1}{2} \frac{\lambda_p c}{c - v_{gr}} \tag{3.6}$$

and is around $2 \, \text{mm}$ for $n_e = 1 \times 10^{19} \, \text{cm}^{-3}$. Since v_{gr} approaches c as n_e decreases, a natural way to increase the dephasing length is by lowering the pressure of the gas. For $n_e \ll n_c$, the dephasing length can be written as $l_{dph} = \lambda_p \frac{n_c}{n_e}$. However, decreasing n_e also increases both the critical power needed for self-focusing and the wave breaking threshold, and it thus places higher demands on the laser. Clearly, a compromise has to be found depending on the laser parameters of the laser being used.

3.3.3 Mono-energetic beams

Early experiments on wakefield acceleration were performed in laser–plasma conditions implying SMLWFA. The energy spectrum of the electron beam then becomes maxwellian, having $100\,\%$ energy spread, and can be fitted to an effective temperature. Distributions of this type are not very desirable; for most applications a narrow energy spread is required. During early experiments, we saw evidence of non-maxwellian spectra already in 2002 (see Paper IV), but were

not able to pinpoint the conditions needed to reliably reproduce them. Now, quasi-mono-energetic electron beams are easily generated, see e.g. [40, 41]. The main differences are that the conditions are now in the LWFA range, and that the acceleration is terminated before the dephasing length is reached. By using $f/10$ focusing optics (Paper I), instead of $f/3$ optics (Paper IV), the self-focusing of the laser can be made more gradual. Simulations suggest that tighter focusing gives rise to a filamented channel and less effective wakefield generation [42].

The process leading to a mono-energetic electron spectrum can be described as follows (see also Figure 3.4). As the laser pulse propagates, it is compressed both longitudinally and transversely, evolving into what is called the "bubble" regime [43]. The ponderomotive force arising from the laser fields then evacuates the electrons in a bubble behind the pulse. The plasma wake then increases in amplitude until it undergoes transverse wave breaking. Electrons are injected at the top of the potential crest of the wave and accelerated. Beam loading of the injected electrons dampens the amplitude of the plasma wave, causing the injection to stop. All the accelerated electrons then experience approximately the same potential. The plasma wave is terminated at the end of the gas jet, before dephasing. A narrow-energy-spread electron beam emerges from the interaction. It was noted during experiments that the mono-energetic features often coincided with a very low divergence of the electron beam.

3.4 Experimental setup

This section describes the hardware used for the electron acceleration experiments described in this thesis and the different diagnostics used to characterize the interaction. Figure 3.5 shows an overview of the setup used in the experiments presented in Papers I–III, showing the general layout of the equipment.

3.4.1 The gas jet

The medium in which electron acceleration takes place is often helium gas. This will be completely ionized by the laser, providing a single ion species plasma; a useful feature when trying to analyze the interaction. Hydrogen is an alternative, but it is dangerous to use as it is flammable. Since the laser must propagate in vacuum after it has been compressed, some sort of containment of the gas is required. A cell with thin walls would be an option, but the laser would burn a hole after the first shot and cause leakage. The gas density would then have a smooth gradient, which is undesirable because of refraction of the laser in the plasma.

Instead, a pulsed gas jet is used (see Figure 3.6). The nozzle orifice is closed by a small Teflon poppet that can be lifted momentarily by a solenoid. When released, the poppet is pushed back into the orifice by the applied backing pressure. A few ms before a shot, the solenoid lifts the poppet and a puff of gas is ejected. The gas expands down the nozzle, forming a supersonic jet with a well-defined boundary. The laser can then be focused onto the edge of this jet. The density profile can be measured with an interferometric technique (see, for example, [45] for a description), and a typical example is shown in Figure 3.7.
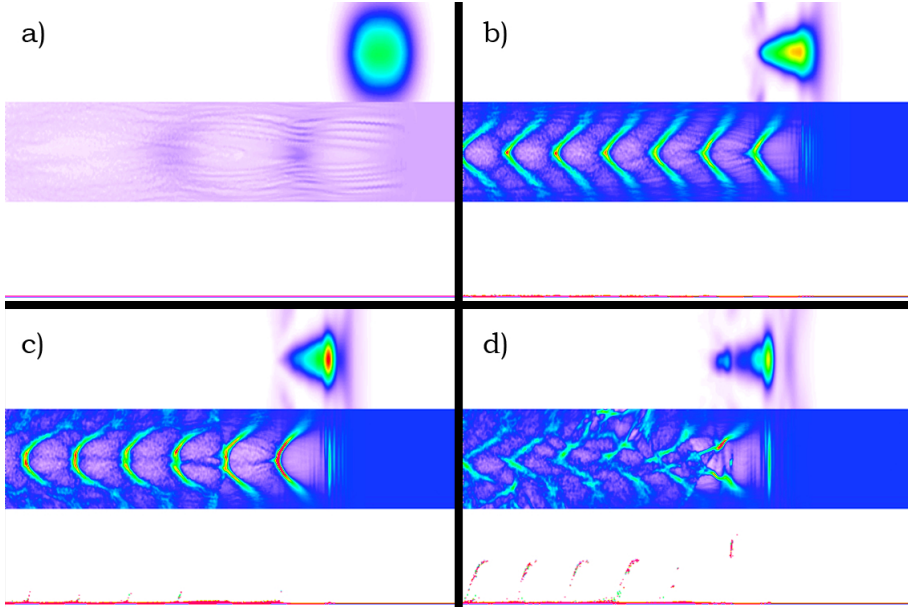
Figure 3.4: A sequence of images showing a particle-in-cell (PIC) simulation with the code OSIRIS [44] (courtesy of S. P. D. Mangles) of the laser–plasma interactions involved in wakefield acceleration. Each frame, a-d, is divided into three parts. The top part shows the laser pulse, the middle part shows the electron density and the bottom part shows the longitudinal phase space of electrons. a) The plasma wake is starting to form. b) As it grows in amplitude, the fields modulate the laser pulse. c) At a threshold electric field, the wave breaks and electrons are injected into the accelerating structure. d) Beam loading prohibits further growth of the plasma wave. If the acceleration is terminated before reaching the dephasing length, an electron beam with low energy spread can be generated.

Some of the laser light can be tapped off after the interaction and sent to a spectrometer. Provided that the spatial extension of the pulse, $c\tau_L$, is longer than the plasma wavelength, part of the laser will be modulated by the plasma frequency via Raman scattering. This is seen as side bands in the spectrum, and can be used to estimate n_e in the plasma. When performing these electron density measurements, the pulse duration is first increased by moving one of the gratings in the compressor. Figure 3.8 shows a calibration curve obtained for one of the experiments described in Paper I. The calibration should be checked intermittently because of the tendency of the poppet to deform.

3.4.2 Side-view imaging

In the experiments presented in Papers I–III, a high-quality f/2 lens, yielding a resolution of about $2\,\mu$m at 800 nm, is employed to view the interaction from the side. As the laser propagates through the gas, it will ionize it and produce a
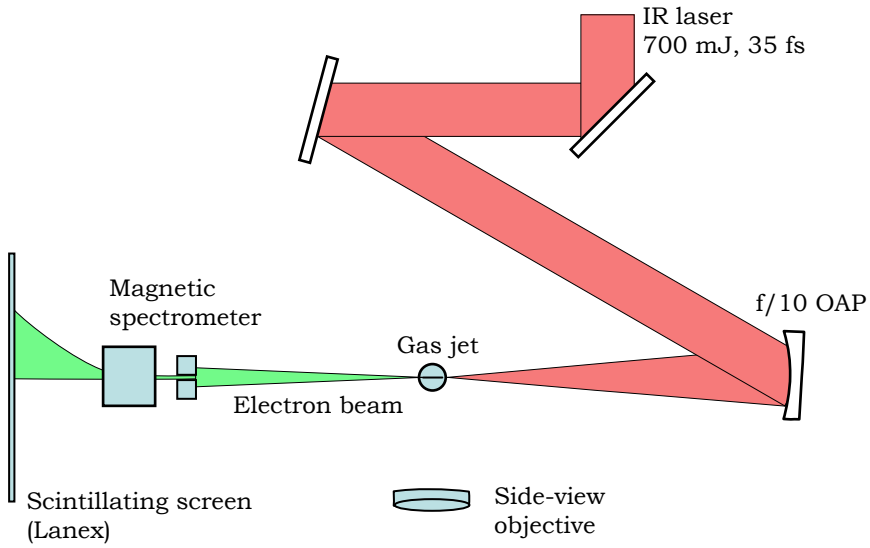
Figure 3.5: Typical setup of an electron acceleration experiment.
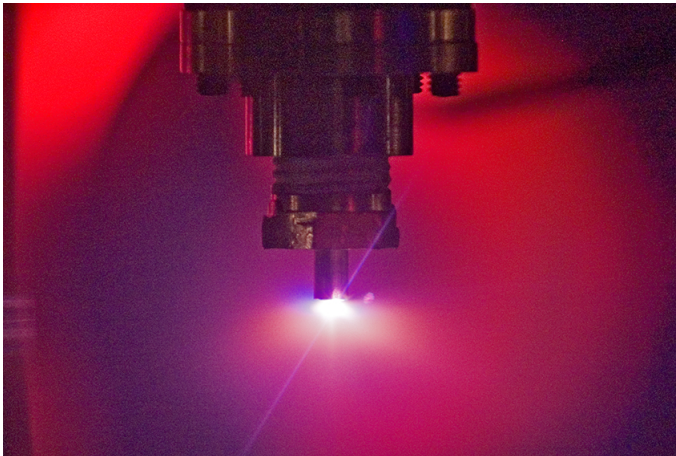
Figure 3.6: A view of the supersonic nozzle during a laser shot. The interaction of the laser with the gas jet is seen as a bright flash of Thomson-scattered laser light and plasma emission. The reddish glow in the background is from a HeNe alignment laser. The outer diameter of the tip of the nozzle is 3 mm. (Figure 3.2 shows a zoomed-in version, with the plasma light filtered out.)
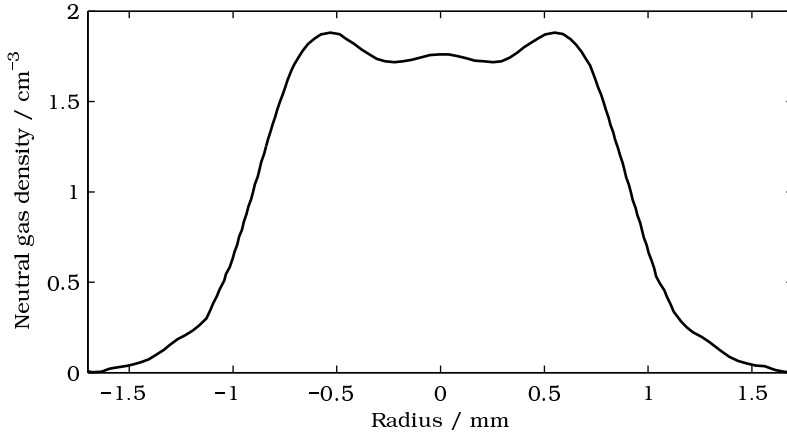
Figure 3.7: The gas density profile obtained from a supersonic nozzle with a 2 mm diameter opening, measured 1 mm from the nozzle exit. The density increases rapidly for ~ 0.5 mm and then remains approximately flat. (Data courtesy of S. P. D. Mangles.)
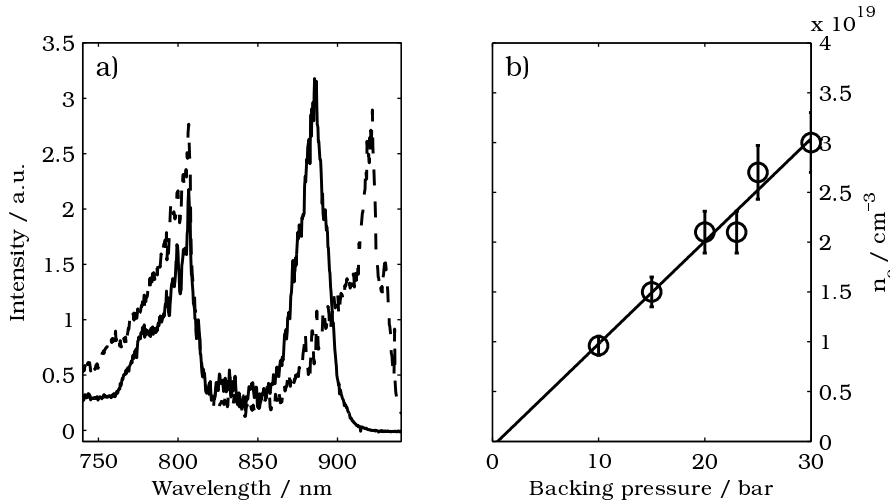
Figure 3.8: In a), typical Raman-shifted spectra are shown. The solid line shows a backing pressure of 15 bar, and the dashed line 30 bar. The laser is centered around 800 nm, but the spectrum is heavily modulated by the Raman process. Large wavelength shifts of 86 and 122 nm are seen for the Raman peaks. The intensity of unshifted laser light is much higher than the Raman shifted, but it has been reduced by means of a filter before entering the spectrometer. b) shows a calibration curve for n_e vs. gas backing pressure. The circles are measured values and the line a least-squares linear fit to the data. Error bars show $\pm 10\%$, the estimated uncertainty in the measurement.

plasma. The plasma expands and the ions and electrons will eventually recombine (on a ns timescale [46]), emitting radiation. The laser itself, will, however, also scatter off the plasma electrons through Thomson scattering [47]. The intensity of the emitted radiation (in the case of incoherent Thomson scattering, which is what we have here) is proportional to the electron density. In regions with small numbers of electrons, such as extensive electron cavitation, the signal will be greatly reduced and may even disappear. In addition, the laser is usually affected by the "sausaging" instability, i.e. variation in spot size during propagation, when self-focusing. The combination of these two phenomena results in the Thomson scattered light appearing as a sequence of bright beads. A typical example of a relativistic channel, seen with side-view imaging, can be seen in Figure 3.2. The streaks are a diffraction effect, caused by the very small size of the emitting volume (the linear dimension of the channel is on the order of λ_p, typically $\sim 10\,\mu$m).

3.4.3 Scintillators and semiconductor diodes

To detect the electrons, a scintillator made of gadolinium oxysulfide, known by the trade name Lanex regular, is used. Its normal application is in medical X-ray detection. In this type of scintillator the active material is mixed with a polymer base to provide structural stability. Additional layers of plastic sandwich the active volume. Scattering of the emitted light limits the resolution that can be obtained. Tests have shown that with the electron flux levels encountered here, quenching (i.e. non-radiative de-excitation) is not a problem and the response can be considered linear [48].

To obtain absolute calibration for the scintillator light level as a function of the number of electrons, semiconductor diodes with known response to electrons can be used. They are placed after the scintillator at points behind the magnetic spectrometer (to prevent γ-rays and other high energy radiation from disturbing the signal), covering half of the exposed width. The scintillator output is then compared with that of the diodes. However, this form of calibration was not done in the experiments described here, and only relative signal levels can be compared. Since the diodes are much more sensitive than the scintillator, they have the additional advantage of being very useful when optimizing the electron signal from extremely low levels.

3.4.4 Magnetic spectrometers

The energy spectrum of the electrons can be determined in a simple magnetic spectrometer. Knowing the field distribution, which has been mapped out with a Hall probe, the motion of the electrons in the spectrometer can be traced numerically, using relativistic dynamics. The more energetic an electron is, the less it is bent in the field, and the resolution of the spectrometer decreases for higher energies. The upper detection limit is determined by the dispersion of the magnets and the size of the pinhole in front of them. For some shots in our experiments, in particular when generating mono-energetic beams, the divergence of the electron beam is smaller than the angle subtended by the pinhole. This increases the resolution, but adds the problem of the accelerated

Table 3.1: Properties of the magnetic spectrometer, for a current $I = 1.4\,\mathrm{A}$ through the field coils, used in the electron acceleration experiments. The maximum energy is defined as the point where the energy spread caused by the pinhole size is half of the detected energy.

Property	Value
Pinhole diameter	8 mm
Distance pinhole–gasjet	560 mm
Minimum detectable energy, W_{min}	20 MeV
Maximum detectable energy, W_{max}	200 MeV
Resolution at W_{min}	0.7 MeV
Resolution at W_{max}	100 MeV

particles actually hitting the pinhole. The lower detection limit is where the electrons are bent to such an extent that they hit the edge of the detector. The properties of the magnetic spectrometer used in the experiments described in Papers I–III are summarized in Table 3.1.

3.4.5 The beam profile monitor

In a simple arrangement, an aluminium plate, with a piece of scintillator on the back, can be lowered into the beam. The plate shields off the laser light, but high-energy electrons can easily pass through it and excite the scintillator. A CCD camera with a lens records the beam profile. This diagnostic tool is mutually exclusive with the spectrometer, but is used in conjunction with the side view.

3.4.6 Cameras

Essential features for cameras capturing images from pulsed laser experiments are external hardware trigger and progressive scan. Cameras with video output are normally interlaced. Thus only half of the image is recorded in the vertical direction, effectively cutting the resolution in half. They are also most often free running, and not synchronized with the laser, with the trigger functionality provided by the frame grabber. On occasion, the laser is fired during readout of the previous frame on the camera, leading to a missed shot. More than 8 bits, i.e. 256 levels of gray, are usually not possible. The ideal camera should have a high bit depth (≥ 10 bits) and progressive scan. The number of pixels is in general not that important, but rather the size of each pixel.

3.5 Results and discussion

3.5.1 Parameter space for mono-energetic electron beams

As stated in Section 3.3.3, a dephasing length longer than the interaction length is needed to generate mono-energetic electron spectra. This can be achieved by

lowering the plasma density. When n_e is lowered even further, the plasma wave does not break or provide injected electrons. For a particular laser intensity (i.e. the wave breaking threshold), there should then be an optimum electron density and a range that gives mono-energetic spectra.

To investigate this (Paper III), the backing pressure was varied from 10 to 15 bar, giving electron densities spanning the range 0.9–1.5 × 10^{19} cm^{-3}. For each setting, the electron spectrum for on-target laser energies in the range 0.3–0.7 J was recorded. Figure 3.9 shows the evolution from maxwellian energy distributions to mono-energetic, having a peak at around 100 MeV. Electron energies in this range were readily reproduced, with occasional shots of up to 170 MeV. The relative number of shots at a particular setting that gave mono-energetic electrons, using the term quite loosely (i.e. peaked spectra), is shown in Figure 3.10. Lower electron density requires higher laser energy to achieve wave breaking, but once the condition is fulfilled the accelerated electrons are likely to be mono-energetic. The energy of the electrons in the peak produced with low n_e was at least as high as that for higher n_e, but this is not visible in the figure. At electron densities in the upper part of the range, the spectra were mostly maxwellian with only occasional shots producing a peaked distribution. Also, here a large number of shots had an electron spectrum with several peaks. This can be interpreted as the breaking of trailing plasma periods, each producing a mono-energetic beam but with different energy.
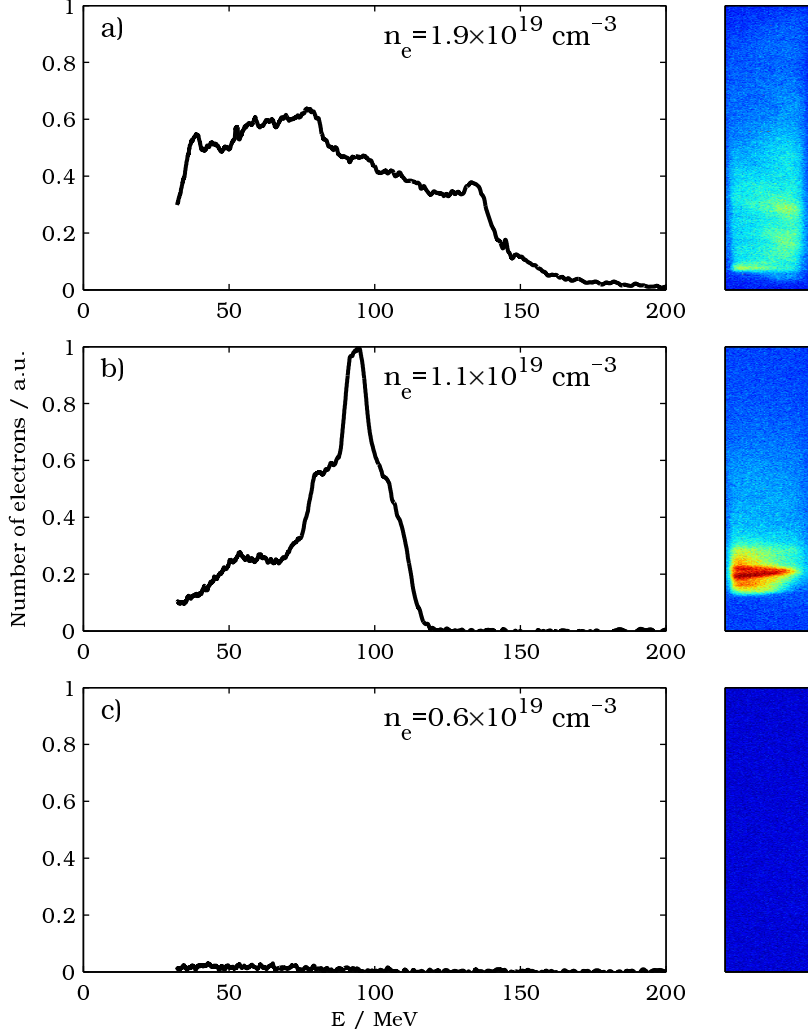
Figure 3.9: A critical parameter in achieving mono-energetic electrons is the electron density. This sequence of graphs shows the evolution from a maxwellian to a quasi-mono-energetic spectrum as the electron density, n_e, is decreased. If n_e is decreased even further, the plasma wave does not break and no energetic electrons are detected. The raw scintillator image from that shot is shown beside each graph. The electron energy is increasing from top to bottom of the raw images.
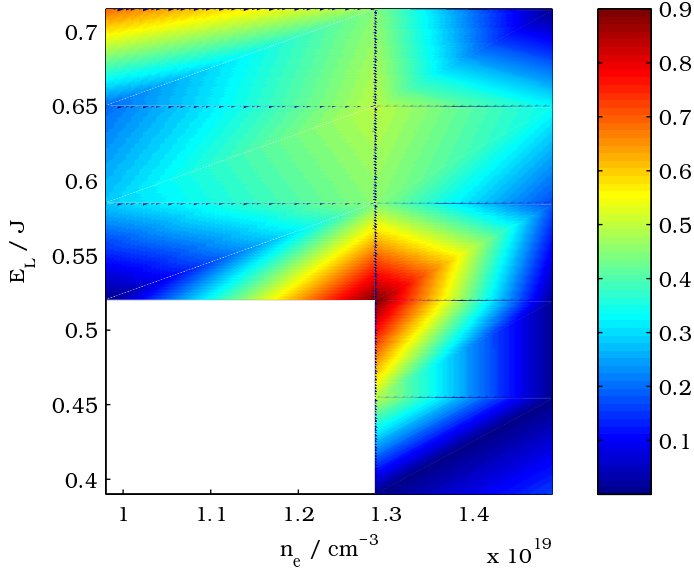
Figure 3.10: Regions in parameter space showing mono-energetic features. The color scale is the relative number of shots for a given combination of on-target laser energy and electron density that produced mono-energetic electron spectra. Clearly, there is an optimum at $n_e = 1.3 \times 10^{19} \, \mathrm{cm}^{-3}$. At higher electron densities, the spectra are mostly maxwellian. At lower densities, a higher laser energy is required to achieve mono-energetic acceleration. No data were taken for the white region in the lower left corner.
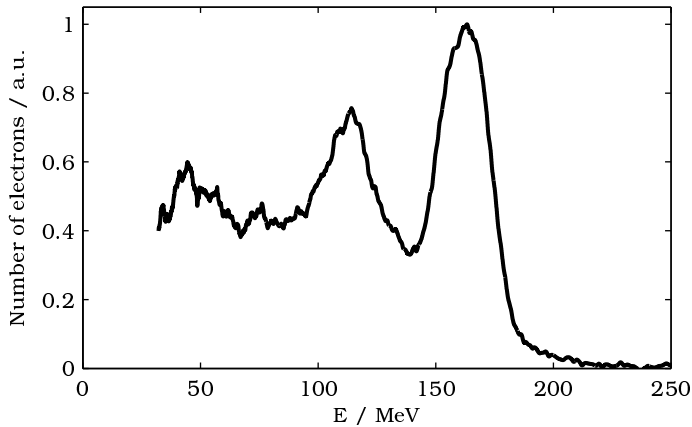
Figure 3.11: Electron spectrum showing multiple peaks. Parameters for this shot are $E_L = 0.6 \, \mathrm{J}$ on target and $n_e = 1.3 \times 10^{19} \, \mathrm{cm}^{-3}$. The three peaks can be interpreted as the successive breaking of three plasma periods.

Figure 3.12: In a), the position of the centroid of the electron beam on the profile monitor is plotted for a few laser contrast settings. The position is seen to move both horizontally and vertically. At the lowest contrast, no high-energy electrons are produced. The pointing stability, represented by the error bars, is greatly enhanced at the highest contrast setting. In b), the integrated energy in the electron beam is plotted against laser contrast. The energy is crudely estimated as the integral of the pixel intensities of the scintillator signal. After a steady increase in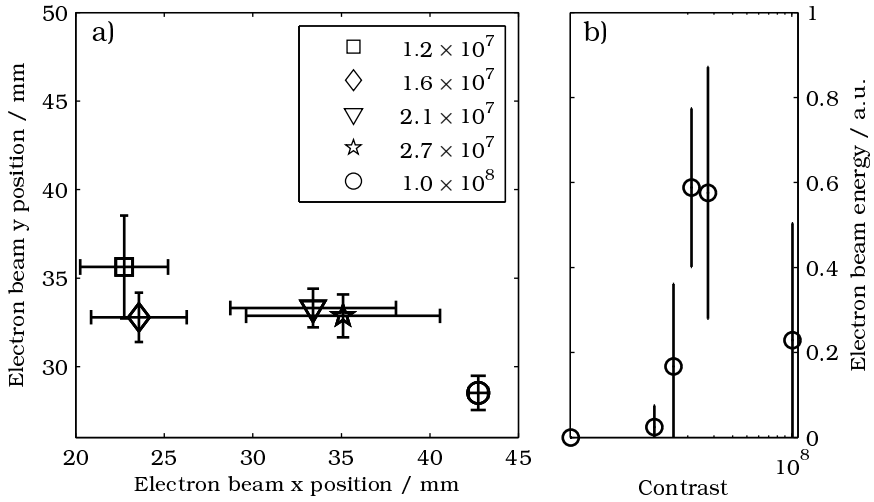 energy, it falls slightly for the highest contrast setting. The error bars represent one standard deviation of the fluctuations in the data set for each contrast setting (typically 7 shots).

3.5.2 Contrast dependence

With temporal contrast ratios in the range 10^6–10^8, values commonly found in many laser systems, and focused intensities on the order of $10^{19}\,\mathrm{W/cm^2}$, the ASE reaches 10^{11}–$10^{13}\,\mathrm{W/cm^2}$ on target. These intensity levels can be high enough to pre-ionize the gas. The plasma created will then have time to evolve and expand before the main pulse arrives. Since an expanding plasma is prone to develop various instabilities, it can be expected that the reproducibility of the main pulse interaction will be affected.

To investigate this, the ability to control the contrast of the Lund multi-TW laser was put to use (Papers II and III). Either the beam profile monitor or the electron spectrometer was inserted into the electron beam and the corresponding beam characteristic measured. By changing the laser contrast systematically and recording the direction of the accelerated electron beam for each setting, a contrast-dependent effect was indeed observed (Figure 3.12). Shot-to-shot fluctuations in the electron energy spectra were also greatly reduced at the best laser contrast.

Though not normally considered an important factor for electron acceleration in gas jets, these observations highlight the need for good control of the
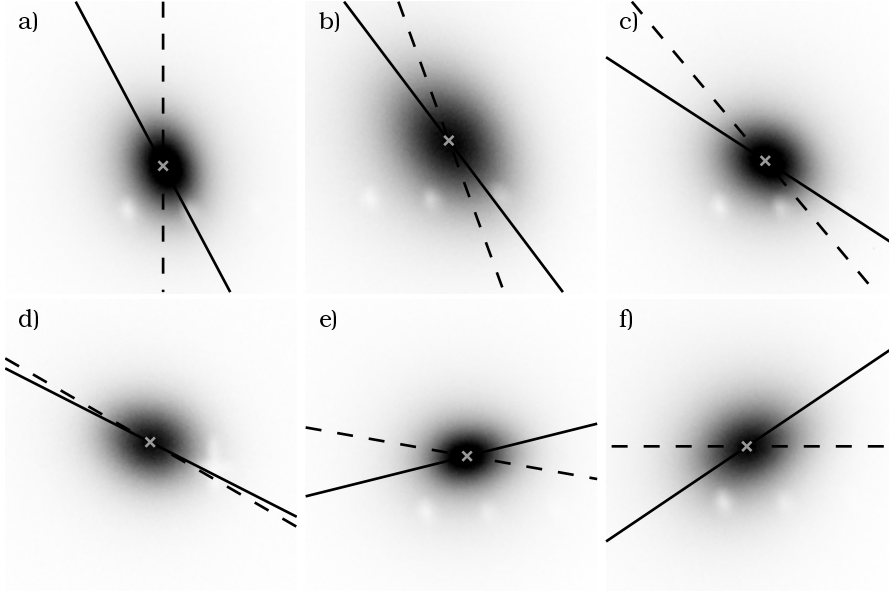
Figure 3.13: A sequence of images showing elliptical electron beam profiles, rotated by changing the polarization direction of the laser. The major axis of the ellipses is shown by solid lines. Dashed lines indicate the orientation of the $\lambda/2$ plate used to rotate the polarization direction of the laser. The systematic offset between the ellipse and laser axis is attributed to misalignment of the optical axis of the $\lambda/2$ plate. Experimental parameters: $E_L = 700\,\text{mJ}$ on target, $\tau_L = 68\,\text{fs}$ and $n_e = 2.1 \times 10^{19}\,\text{cm}^{-3}$.

laser contrast, even in underdense plasma experiments.

3.5.3 Polarization dependence

In the description of mono-energetic electron acceleration in an underdense plasma in Section 3.3.3, the laser pulse forms a bubble, void of electrons, around itself. When the plasma wave breaks, electrons are injected into the back of this bubble and subsequently accelerated as they "surf" down the potential of the plasma wakefield. The electrons will then pass through the region occupied by the laser pulse, and interact with the oscillating electromagnetic fields present there. In this process, the electrons acquire transverse momentum in the direction of the electric field component of the laser (i.e. the polarization direction). The electron beam profile then becomes elliptical with the major axis along the laser polarization.

To investigate this, a zero-order mica $\lambda/2$ plate was placed in the unfocused laser beam path (Paper I). By rotating the plate, the polarization direction of the laser could be controlled. At conditions (n_e and E_L) where the laser pulse duration was shorter than the plasma wavelength, the elliptical contour of the electron beam was recorded on the beam profile monitor. The results

essentially confirmed the theory, with the axis of the ellipse closely following the laser polarization (see Figure 3.13).

In addition, if λ_p was shortened (by increasing n_e), the ellipticity of the electron beam was increased. This can be seen as indirect evidence that the electrons are accelerated in the first plasma period, since the laser pulse then occupies a larger part of the bubble and interacts more strongly with the accelerated electrons. The duration of the electron bunch can then be inferred to be shorter than the plasma wavelength, i.e. 25 fs for the experimental parameters used (Paper I).

3.5.4 Longitudinal mapping of the plasma wave

The results of the experiment on longitudinal mapping have not yet been published, but will be described here for completeness. The idea was to map out features of the plasma wakefield by detecting the wavelength shifts of a co-propagating probe pulse. In regions where the slope of the plasma electron density is positive, the light would be shifted towards shorter wavelengths (blue shift), and in regions with a negative slope it would be red shifted. This effect is known as photon deceleration/acceleration [49, 50].

To be able to discern the probe light from the transmitted main pulse, a different wavelength is required. Part of the main beam was therefore tapped off inside the last amplifier and separately compressed. A huge advantage of not using a separate laser for the probe, is that it will be perfectly synchronized and jitter-free. During frequency doubling in a KDP crystal, the pulse duration was somewhat lengthened to around 100 fs. A special dielectric mirror, transmitting at 400 nm and reflecting 800 nm, was used to insert the resulting blue beam into the path of the main beam. With a delay stage, the doubled probe pulse could sample the structure of the plasma wave at various positions. The effect of the wakefield on the probe was monitored with a spectrometer.

The group velocity of light in plasma is wavelength dependent, see Eqn 1.5. For typical values, i.e. $n_e = 1 \times 10^{19} \, \text{cm}^{-3}$ and $l_{channel} = 1 \, \text{mm}$, the blue pulse will have advanced by $2 \, \mu\text{m}$ relative to the infrared pulse after the interaction. The plasma wavelength was $10 \, \mu\text{m}$, so the effect is small.

Figure 3.14 shows the evolution of the spectrum of the transmitted probe as the position was scanned through the plasma wave structure. The spatial extent of the probe pulse ($30 \, \mu\text{m}$) was longer than λ_p ($10 \, \mu\text{m}$), causing a splitting of the center wavelength both up and down in wavelength. After around $60 \, \mu\text{m}$, the splitting disappears, indicating a plasma structure of roughly the same dimensions (convolved with the $30 \, \mu\text{m}$ probe), i.e. ~ 4–$5\lambda_p$. At positions close to the front of the structure, the red shifted part dominates, with the converse for positions at the end of the structure.
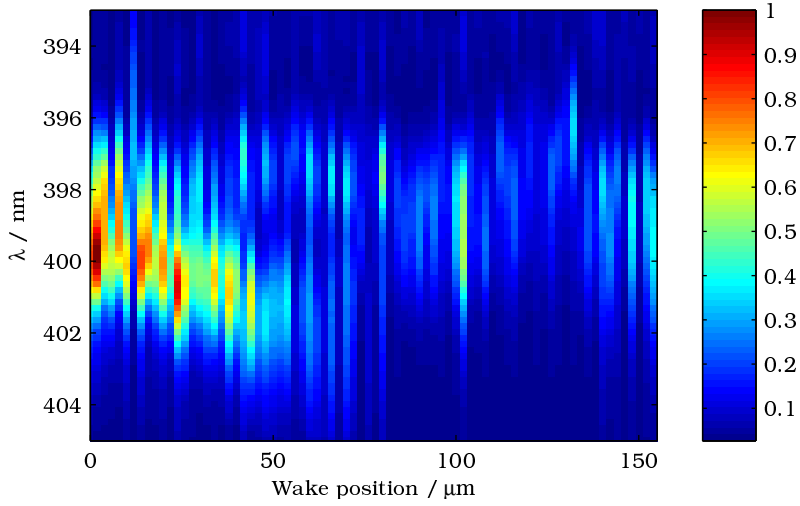
Figure 3.14: Results from the blue beam plasma probing. The recorded laser spectrum after the interaction is shown on the y-axis and the x-axis gives the position of the probe in the wake. This sequence is for $n_e = 1.1 \times 10^{19}\,\mathrm{cm}^{-3}$ and $\lambda_p = 10\,\mu\mathrm{m}$. When the probe starts to overlap the plasma wake, at around $20\,\mu\mathrm{m}$ into the scan, the spectrum splits into two portions a few nm apart. Unfortunately, the pulse duration of the probe (spatial extent $\sim 30\,\mu\mathrm{m}$) is longer than the plasma wave period. As a result, detailed mapping of the wave structure was not possible. The splitting is seen to decrease further downstream and a structure of $\sim 60\,\mu\mathrm{m}$ is evident.

PROTON ACCELERATION EXPERIMENTS

4.1 Introduction

The plasma waves generated in the underdense plasma experiments described in the previous chapter could, in principle, be used to accelerate protons (and other charged particles) as well. However, this requires them to be injected into the plasma wave at close to the speed of light, i.e. at kinetic energies $\sim 1\,\mathrm{GeV}$ for protons. The large mass of protons compared to electrons means that they do not move appreciably in the electromagnetic fields of today's lasers ($I < 10^{21}\,\mathrm{W/cm^2}$). Focused intensities on the order of $10^{24}\,\mathrm{W/cm^2}$ are needed for protons to achieve relativistic velocities in oscillating laser fields [10]. There is thus no chance of self-injection of protons in the wakefield.

Since non-relativistic protons cannot surf on the traveling wave of a wakefield, they are instead accelerated by establishing a (quasi-)stationary field gradient. To obtain a high field strength, a sharp gradient with high charge density is required [51]. For this reason, most of the experiments on proton acceleration have been carried out using solid targets, in particular thin foils (a few μm thick). Laser-accelerated protons from foil targets with up to $58\,\mathrm{MeV}$ kinetic energy have been detected [52].

This chapter first describes the process of proton acceleration from thin foil solid targets. ASE-induced effects, such as shock waves, will then be discussed. The experimental equipment and detectors used for the experiments will be detailed, followed by a discussion of the experimental results.

4.2 Front surface conditions

As the laser is incident on the front of the target foil, direct laser–matter interaction takes place here. The target surface is quickly ionized, usually already by the ASE, and an expanding plasma is formed, with a density gradient from 0 to solid density. Since the plasma is expanding at the ion sound speed [6](which de-
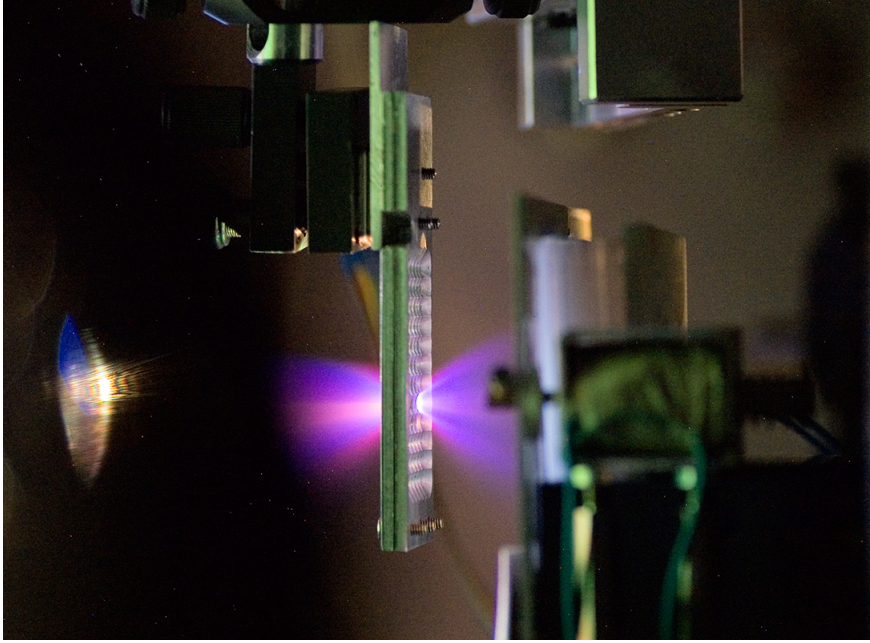
Figure 4.1: Photograph of the interaction of a high-intensity laser pulse with a thin foil target. The laser is traveling from left to right, hitting a $6\,\mu$m Al foil. The colorful light is from plasma emission after the shot. The target foil is sandwiched between two pieces of aluminium with a grid of $1.5\,$mm diameter holes. The movable frames provide support for the foil and make it possible to shoot up to ~ 50 shots in one run. To the right, the CR-39 detector stack is visible (see description in Section 4.8.1).

pends on the electron temperature, but is typically on the order of $\sim 10\,\mu$m/ns), the scale length of this gradient increases over time on a ns timescale. For over-dense conditions, the coupling between plasma and electromagnetic radiation is exceedingly complicated. A number of phenomena takes place, such as hole boring, induced transparency, ponderomotive push, etc. These effects act to deform the plasma and blur the differences between different polarization directions and angles of incidence of the laser. Keeping this in mind, two main mechanisms for energy transfer from laser to plasma electrons can be identified: resonance absorption and $\mathbf{v} \times \mathbf{B}$ heating. In addition, plasma waves can be excited and driven to wave breaking by the laser in the underdense region, similar to that described in Chapter 3.

The laser propagates through the underdense plasma, preformed by the ASE, until it approaches the critical surface, where $\omega_L = \omega_p$. Here, the pulse is reflected, and substantial energy is transferred to the plasma electrons. The preplasma can extend several μm out from the target, depending on the ASE conditions [15]. At the critical surface, electrons are driven resonantly—hence the term resonant absorption—by the electric field of a p-polarized laser, and a plasma wave is excited. The wave energy is eventually thermalized by collisions
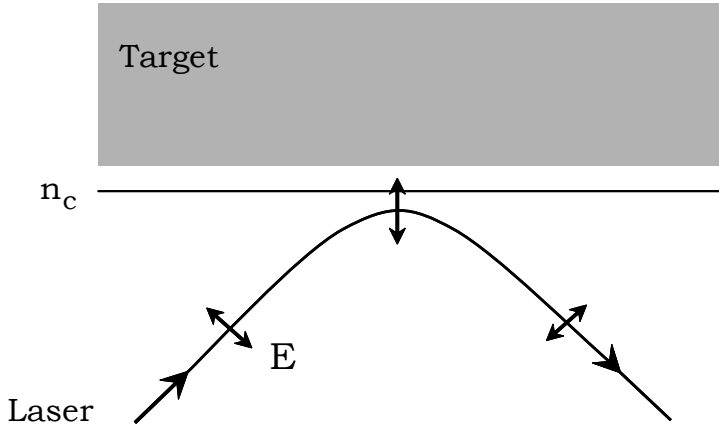
Figure 4.2: A p-polarized laser pulse incident at an oblique angle is continuously refracted and turns over near the critical surface. Here, the electric field of the laser can resonantly drive plasma electrons.

(low intensities) or wave breaking (high intensities). The process is schematically illustrated in Figure 4.2.

Resonance absorption is the dominant channel for energy transfer at lower laser intensities, with a hot electron temperature scaling as $T_{hot} \sim (I\lambda^2)^{1/3}$ [53]. The heated electrons are on average directed into the target, normal to the surface, with a cone angle of $\sim 30°$ [54].

When the plasma density gradient is very steep, the amplitude of the plasma electrons can be larger than the Debye length, rendering resonant absorption ineffective. A related absorption mechanism, called vacuum heating, or Brunel heating [55], then takes over. In this case, the electrons are dragged from the plasma out into the surrounding vacuum. When the laser fields change direction, the electrons are accelerated back into the overdense region, where the laser fields are damped and the electron energy is transferred to the plasma through collisions.

At higher intensities, the electrons have relativistic velocities when oscillating in the laser's electromagnetic field. The magnetic part becomes important and makes the velocity component of the electrons in the laser propagation considerable. The electrons are then pushed into the overdense region twice per optical cycle.

This results in hot electrons with an effective temperature of $T_{hot} \approx U_p$, i.e. scaling with laser intensity as $T_{hot} \sim (I\lambda^2)^{1/2}$ for relativistic intensities (see Eqn 3.3). The direction of these electrons is coaxial with the incoming laser, in contrast to the electrons heated by resonance absorption. This distinction becomes important in explaining the experimental results in Papers V and X, as discussed in Section 4.9.1.

The total conversion of laser energy into hot electrons is given by the em-

pirical formula [56]

$$\eta = 4.7 \times 10^{-9} \, (I\lambda^2)^{3/4} \tag{4.1}$$

with a maximum of 0.5, and where I and λ are in SI-units.

The two electron populations, with their different directions, have been experimentally confirmed with the use of a Čerenkov-emitting material [57].

The efficient coupling of laser energy to hot electrons creates charge separation in the interaction region. In the subsequent Coulomb explosion of the positively charged volume, protons can be accelerated to energies on the order of the ponderomotive potential.

4.3 Back surface conditions

The back of a thin foil target does not see the direct laser radiation, as it is reflected when reaching the critical surface. The back is, however, indirectly affected by the laser. The heat from the deposited energy will eventually reach the back surface and vaporize it. On a shorter timescale, the hot electrons generated at the front surface traverse the target and reach the back. There, they will set up a huge electrostatic field at the sharp solid–vacuum interface. The density gradient is much larger than at the front surface, where a preplasma is present, and consequently the field strength at the back is higher. Hydrogen atoms (and other atoms) at the surface are field ionized and accelerated by this field. The electrons do not transfer any heat to the protons, which consequently remain cold during the acceleration [2]. Potentially very low transverse emittance beams are thus possible. Since the plasma created by the field ionization is a good conductor, the electrostatic field is always perpendicular to the target surface. This leads to acceleration of the protons in the direction of the target normal, and the mechanism is called target-normal sheath acceleration (TNSA). The TNSA mechanism makes it possible to steer the protons by tilting the target. If the target surface is curved, this can lead to focusing of the proton beam [15, 16, 58].

4.3.1 Recirculation

After an initial build-up of the electron sheath, electrons leaving the front with energies lower than the potential energy of the sheath, will be reflected back to the laser interaction region. There they are reflected again, possibly with some additional energy gained from the laser. Upon returning to the back surface once more, their increased energy enhances the electrostatic field present there. This process is known as recirculation [59–61]. In order for it to have an effect, the transit time of the electrons back and forth through the target must be shorter than the laser pulse duration. For a given τ_L, this places a restriction on the target thickness d: $d < \frac{c\,\tau_L}{2}$.

4.3.2 Shielding and heavy-ion acceleration

The same mechanisms that generate energetic proton beams, are equally suited for heavier ions. When discussing different ion species, it is convenient to normalize the charge-to-mass ratio to atomic units $q_e/u = 95.9 \times 10^6$ C/kg, i.e.
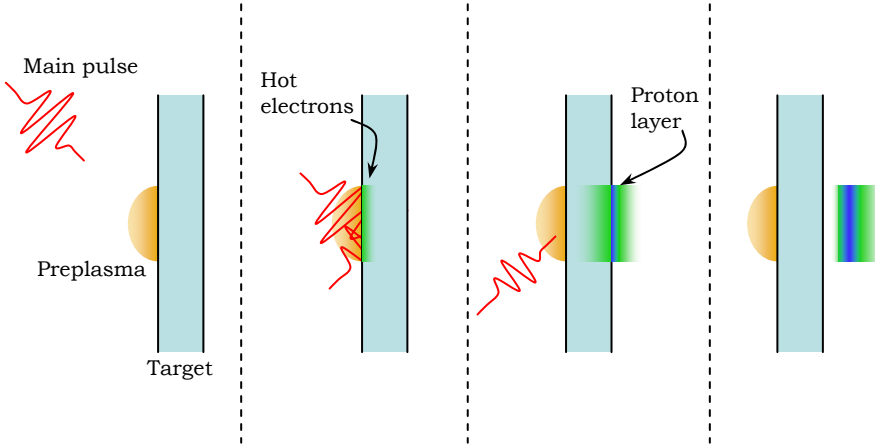
Figure 4.3: Schematic overview of the target-normal sheath acceleration mechanism. The laser heats up electrons at the front surface and in the ASE-generated preplasma to MeV temperatures. The electrons pass through the bulk of the target and appear on the other side. The first, most energetic, electrons escape, but the rest are trapped by the Coulomb force and form a sheath, with an extent on the order of λ_D, on the back surface. An electrostatic field is generated, and atoms at the surface are field ionized and subsequently accelerated by the field. Note that the laser is incident at an oblique angle, but the accelerated protons are directed along the target normal.

$\left(\frac{q}{m}\right)_{protons} = 1$. Protons have at least twice the $\frac{q}{m}$ of any other ion, and are thus accelerated at least twice as fast. Protons will therefore quickly take the lead over heavier ions. Another factor is the geometrical layering of the ions; the protons being located directly on the surface. This is due to the main proton source being adsorbed contaminants, such as water vapor and hydrocarbons. Since the electric field is generated by electrons forming a cloud ahead of the ions, the swiftly accelerated protons will shield this field from the other ions and "steal" most of the energy.

To be able to see appreciable numbers of heavier ions, care has to be taken to remove the proton contaminants, see Section 4.6.1. Even with no protons, the higher $\frac{q}{m}$ ions will shield off the lower $\frac{q}{m}$, and the ion energy spectra are heavily dependent on this parameter ([62] and also Paper XI).

4.4 Laser-induced shock waves

The intensity contrast of most CPA laser systems is on the order of 10^6–10^8. When focused to intensities of $\sim 10^{19} \, \mathrm{W/cm^2}$, the ASE level is in the range 10^{11}–$10^{13} \, \mathrm{W/cm^2}$, i.e. above the ionization threshold for most solid materials. Once seeded, ionization grows quickly (on a ns timescale) through collisions.

Laser energy is effectively transferred to the target, ablating material at the surface. The hot ionized particles are ejected at high speed, and exert very high pressure on the target due to momentum conservation. The rapid onset of the pressure leads to a shock wave being launched into the target. This type of experiment is a research field of its own, connected to equation of state (EOS) studies. As we have found these shocks to play an important role in the proton acceleration dynamics, see e.g. Papers V and X, they are briefly discussed here.

Shock and particle velocities can be deduced analytically in a one-dimensional case assuming conservation of mass and momentum [8] resulting in

$$u_s = \frac{c_0}{2}(\sqrt{1+x}+1), \tag{4.2}$$

$$u_p = \frac{c_0}{2\alpha}(\sqrt{1+x}-1), \tag{4.3}$$

where the dimensionless variable $x = \frac{4\alpha}{\rho_0 c_0^2}P$ has been introduced. P is the applied pressure, ρ_0 and c_0 are the material constants for un-shocked density and speed of sound, respectively. The parameter α relates the shock speed, u_s, to the particle speed, u_p, according to $u_s = c_0 + \alpha u_p$, and usually has a numerical value of ~ 1.

The ablation pressure produced by the laser is found to depend on intensity according to $P = \zeta I^{\frac{2}{3}}$ [63]. The material constant ζ is ~ 1 if SI units are used.

Upon reaching the back of the target, the shock wave breaks out and the target starts to expand with a velocity given by

$$u_e = 2u_p. \tag{4.4}$$

At the same time, a rarefaction wave is reflected back into the target. It will travel back to the front, be reflected again, and so on.

The rapid compression of the target material in the shock front, leads to a temperature increase and possibly a change of state [64]. For a given shock pressure, the temperature behind the shock front reaches a certain material-dependent value, a relationship known as the Hugoniot curve of the material. Figure 4.4 shows an example for aluminium. The melting temperature of solid matter generally increases with pressure. The intersection of the Hugoniot curve with the melting curve gives the maximum shock pressure that can be applied to a solid before it melts. For the example of aluminium in Figure 4.4, this is at $P = 130\,\text{GPa}$. If the shock pressure is below this value, the target remains solid after shock breakout. At higher pressures, melting takes place due to the heat released, and the sharp density gradient at the back surface starts to deteriorate, decreasing the effectiveness of the TNSA.

Figure 4.5 shows a 1D hydrodynamic simulation of a laser-generated shock, obtained with the code MULTI [66]. It uses tabulated EOS data, see e.g. [67], and includes a laser absorption model. The shock traverses a $6\,\mu\text{m}$ thick target foil in 0.75 ns, and the back surface subsequently starts to move with a velocity according to Eqn 4.4, but in this case with the sharp density gradient intact. The laser-irradiated front surface has a smooth density gradient with μm scale length.
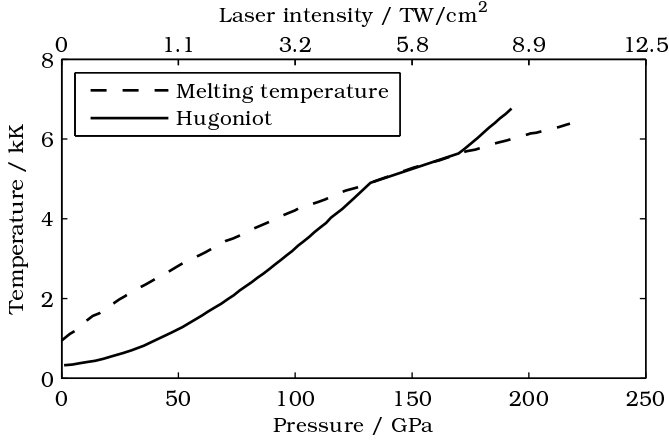
Figure 4.4: Hugoniot and melting curves for aluminium (data adapted from [65]). The intersection of the curves at (132 GPa, 4900 K) indicates the melting pressure and temperature for a shock-heated target. The corresponding laser intensity required to drive a shock with this pressure is $4.8\,\mathrm{TW/cm^2}$.

Since the laser focal spot normally has a spatial intensity distribution resembling a gaussian, the shock pressure will have a similar spatial distribution. This results in a curved shape of the expanding back surface.

4.5 Experimental setup

A typical setup for proton acceleration, used in, e.g., the experiments described in Paper V, is shown in Figure 4.6. The laser is incident on the target at a 45° angle. Normal incidence should be avoided in solid target experiments as the overdense plasma acts as a mirror and reflecting a specular, possibly convergent, reflection that can damage the optics in the laser.

4.5.1 The plasma mirror

Increasing the contrast of the laser, at least the part before the main pulse, can be done rather elegantly by utilizing fact that an overdense plasma is reflective to the incident electromagnetic radiation [68]. If an optically flat piece of glass is placed at an angle close to the Brewster angle, the low-intensity ASE pedestal will pass through it. When the main pulse starts to build up a few tens of ps before the peak, the intensity on the glass surface becomes so large that it ionizes ($\sim 10^{14}\,\mathrm{W/cm^2}$ [69]), rapidly forming a high-density plasma. Upon reaching the critical density, the remainder of the pulse is reflected. On the short timescales considered here, the plasma does not have time to develop instabilities that distort the surface quality [70].

For the incoming pulse to have high enough intensity, the plasma mirror is normally placed in a focusing beam. The time at which the glass is switched to a
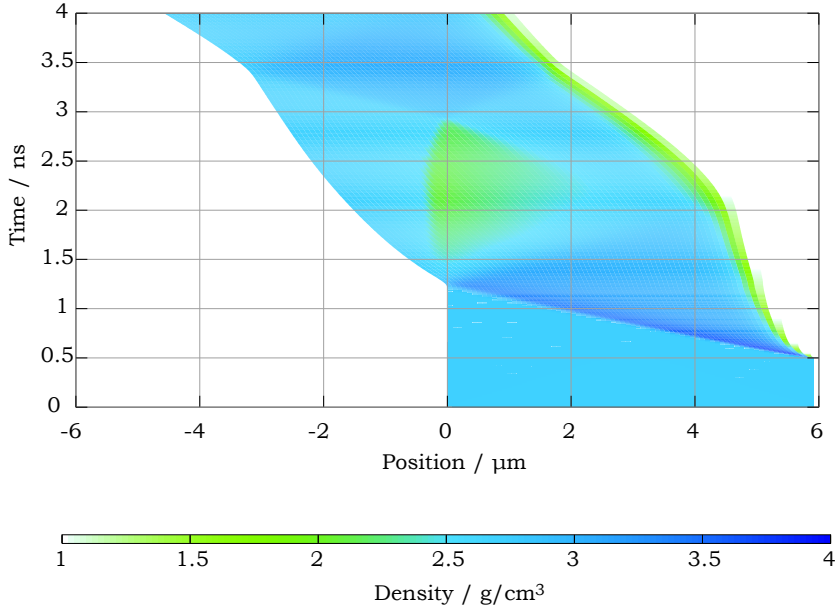
Figure 4.5: Hydrodynamic simulation, from Paper X, of shock transport and breakout in aluminium. A $1 \times 10^{12}\,\mathrm{W/cm^2}$ laser pulse travels in from the right, hitting a $6\,\mu\mathrm{m}$ thick aluminium foil at $t = 0.5\,\mathrm{ns}$. The ablation of material sends a shock wave through the target at a speed of $8\,\mu\mathrm{m/ns}$. Upon reaching the back surface after $0.75\,\mathrm{ns}$, the shock breaks out and continues at a speed of $1.6\,\mu\mathrm{m/ns}$. At the same time, a rarefaction wave is reflected and relaxes the compressed target bulk. Now, the whole foil is moving left, and is slightly compressed to a thickness of around $5.3\,\mu\mathrm{m}$.

reflector can then be tuned to earlier or later in the pulse by moving the piece of glass closer or farther from the focus, respectively. The main drawback of using a glass substrate is that the surface is destroyed after a single shot, and a new area must be positioned. This adds complexity and limits high-repetition-rate operation. In the case of high-energy lasers, such as Vulcan, the whole mirror can actually shatter as a result of the heat load.

This technique was used in the experiment described in Paper VII to achieve the enormous contrast of 10^{10}.

4.6 Targets

The proton acceleration experiments were carried out with thin foil targets, usually made of metal. The exact metal does not appear to be critically important, a beam of protons is produced regardless of the material. Differences in materials may be seen in the number of accelerated particles, their maximum
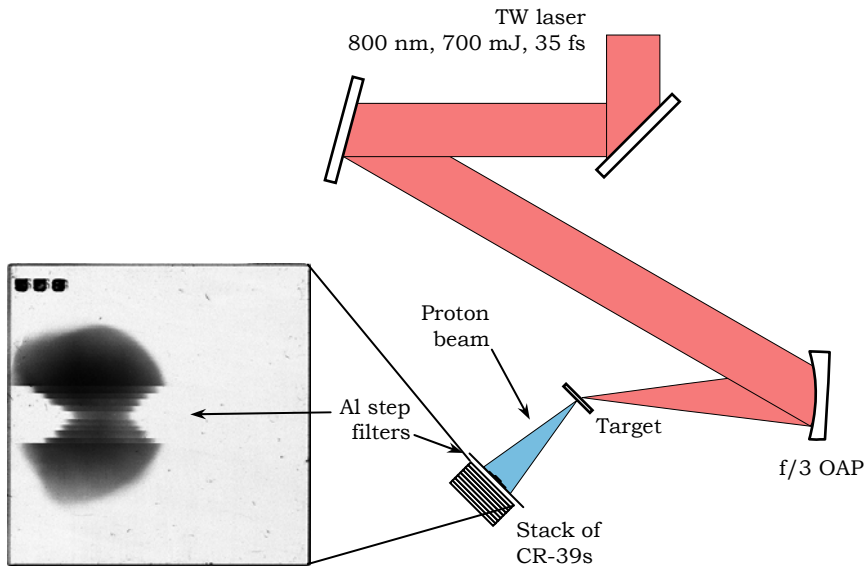
Figure 4.6: Typical setup for a proton acceleration experiment. The protons are accelerated normal to the back surface of the thin foil target. A stack of nuclear track detectors, known as CR-39, makes it possible to make a sequence of shots without breaking vacuum. A filter mask consisting of bands of aluminium foil is placed in front of the detectors; see Figure 4.8 for details. The inset shows a scanned image of an exposed detector plate. The characteristic decrease in divergence with increasing proton energy can clearly be seen.

energy and beam spatial structure. Although this might seem surprising at first, there is always a thin layer of proton-rich contaminants on the foil surface, consisting of water vapor, oil from vacuum pumps, etc.

Foils with thicknesses down to around $1\,\mu$m can be made with normal rolling manufacturing processes. Thinner foils can be made, for example, by using some sort of deposition technique, such as electrochemical or vacuum coating.

Plastic foils, made of, e.g., Mylar can also be used. They are naturally very rich in protons, but also electrically insulating, reducing the electron transport through the bulk material as the cold return current is inhibited [71]. Indeed, the spatial profile of protons from plastic targets is severely filamented compared to metallic targets, with the exception of very thin (sub-micron) foils (Paper VII), in which case the filamentation of the hot electrons probably does not have time to grow before reaching the back of the target.

In the proton acceleration experiments performed with the Lund multi-TW laser, the high repetition rate of the laser makes it possible to fire a shot as soon as a new target is in focus. A good target holder system that allows several shots to be taken in short succession is then needed. We have developed such a system by sandwiching the target foil between two aluminium frames. The frames have a matrix of machined 1.5 mm diameter holes, allowing one
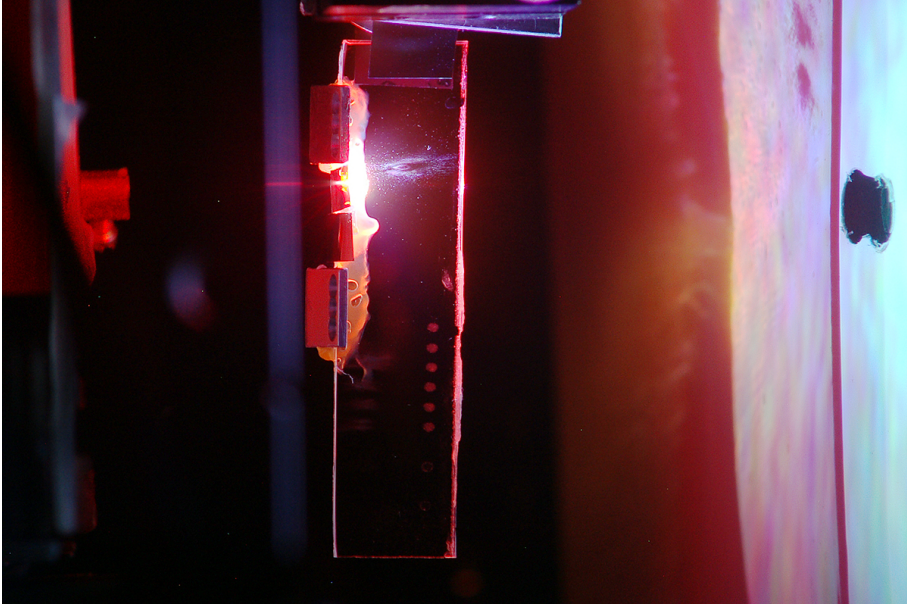
Figure 4.7: Photograph of the plasma mirror, in the form of a vertical glass plate, used in Paper VII during a laser shot. The laser comes in from the right, reflects off the glass and is focused on the target foil. The targets are on smaller holders with three shots each. Just above the flash where the laser hits, a debris mark from the previous shot is seen on the glass plate. The iridescent pattern on the screen at the right side of the picture comes from self-phase modulated laser light reflecting off the target. Dimensions for the whole assembly are 10×3 cm.

shot per hole (see Figure 4.1 which shows a photo of the target holder). With the low-repetition-rate Vulcan laser, we instead made use of targets mounted individually on stalks.

4.6.1 Target cleaning

Several techniques for removing protons from the surface of a target have been tested. The target must be cleaned immediately before a laser shot, as the contaminant layer regrows very quickly (depending on the vacuum level).

One cleaning method is to resistively heat the foil to several hundred degrees C, to remove the contaminants by boiling them off. This obviously only works for electrically conducting materials, and it may deform the foil and also make it thinner due to material loss. Resistive heating was used in the experiment studying palladium ion acceleration (Paper XI). Here we heated the target to $\sim 1000°C$ for a few minutes before and during a laser shot.

Another technique is to ablate the surface atom layers, using either a laser or an ion cannon. An ion cannon is a small accelerator that bombards the target with ions accelerated to appropriate energies to knock out atoms at the surface. An advantage of this method is that one can clean only one or both of

the target surfaces.

4.7 Detectors

Detecting the protons can be quite a problem. When the laser is fired at a solid target, a huge pulse of noise is generated simultaneously with the accelerated protons. Everything from a low-frequency electromagnetic pulse (EMP) up to γ-rays and high-energy electrons flood the experimental chamber. As a result, most electronic detectors are overloaded for a certain period of time. The protons, however, are not relativistic and after a short recovery time, it would be possible to discriminate the proton signal from the noise spike. An additional problem is that electrons co-propagate with the protons as a result of the accelerating process at the back surface. The detector should therefore be either insensitive to electrons and photons, or very fast.

When protons are stopped in solid material, the energy loss per unit length, $\frac{dE}{dx}$, is not constant. Rather, most of their energy is released at the end of the trajectory. This results in a peak, known as the Bragg peak, in the deposited dose, and is in contrast to electrons and photons, which show an exponential energy decrease and do not have a well-defined range. The depth at which the the Bragg peak occurs depends on the stopping material and on the proton energy. Data for the stopping of protons in a wide range of materials can be found in the NIST PSTAR database [72].

4.7.1 CR-39 nuclear track detectors

A detector material that conforms to the requirement of being insensitive to electrons and photons, is the CR-39. It is made of a plastic material commonly used for ophthalmic lenses [73], due to its good optical properties and scratch resistance. It is also used as a nuclear track detector, usually in the form of a 5×5 cm plate, for, e.g., radon measurements [74].

When an energetic baryon ($E_{kin} > 100$ keV) hits the detector, polymer chains in the plastic will be destroyed along the path of the particle. The damage is not immediately visible, but when placed in a solution of warm NaOH, the damaged parts of the plastic are etched much more quickly than the intact parts, and cone-shaped pits are developed. After etching, the plate of CR-39 can then be examined under a microscope and the pits counted and even characterized in terms of size etc. [75]. It is found that heavier ions, due to their higher value of $\frac{dE}{dx}$, make larger pits. These pits to scatter incoming light and if a sufficient number of ions have been recorded, the exposed areas appear milky when examined by eye. As the energy of the incoming particles increases, the distance between polymer damage events will eventually become so large no clear track will be formed, representing the upper limit of the particle energy that can be detected. This is not a sharp threshold, but rather a gradual transition to smaller and smaller pit size. For protons, CR-39 is useful up to ~ 7 MeV. By using filters in front of the detector plate, or a stack of thin detectors, high-energy protons can be slowed down and higher energy protons can be detected.

CR-39 has some very attractive properties, in that it is completely insensitive to electrons and photons, stores the recorded signal indefinitely, and has a practically 100 % quantum efficiency in its energy range. The last point makes it possible to detect very low fluxes. Its disadvantages are the obvious lack of real-time feedback due to the need to develop the plates before the results can be seen (although this might be possible to circumvent [76]). For quantitative analysis, the pits have to be counted, preferably using automated pattern recognition hardware, such as the TASLIMAGE system developed by Track Analysis Systems Ltd. This system was used to obtain the results presented in Papers VII, IX and XI. The dynamic range of CR-39 is quite limited. If the particle flux is too high, the pits start to overlap and can no longer be counted individually. If care is not taken, there is also the risk that overexposed areas, with a very high pit density, will be interpreted as regions with low flux [77]. The dynamic range can be enhanced by developing in short intervals, with microscopic analysis in between. This is because the pit size is small early on, lessening the risk of overlapping pits. Longer development times are needed to resolve low- and high-energy protons. With this technique, a dynamic range of 10^3 was achieved for the proton energy spectra described in Paper VII.

4.7.2   Plastic scintillators

Although CR-39 has several advantages, the inconvenience of breaking vacuum after a few shots and developing the sheets in NaOH for half an hour makes it imperative to seek alternatives.

Using a scintillator is one alternative. Since scintillators are sensitive to other energetic particles besides protons, they should be used in combination with a spectrometer. The short range of protons in solids (see e.g. Figure 4.8 for an example in Al) makes it necessary to use a scintillator without any protective layers over the active material, as is the case for Lanex, to detect protons with a few MeV. A plastic scintillator is then a good option.

On the other hand, the short range can be turned to advantage, to enable the discrimination of protons from X-rays and electrons. The scintillator can be made very thin, thus giving a small signal for high-energy electrons and photons. Another reason for using a thin scintillator, is that the signal should be proportional to either the number of particles or the total energy deposited per unit area. For a thin scintillator, the energy dependence on the deposited energy, and hence the signal strength, is quite weak for protons above a few MeV (see Figure 4.8). The signal is then proportional to the number of protons.

4.7.3   Radiochromic film

Radiochromic film (RCF) is widely used in medical dosimetry applications [78], such as radiation therapy. The film contains sensitive layers of a clear microcrystalline monomeric dispersion sandwiched between polyester layers. When subjected to radiation, the film polymerizes and turns progressively blue. By measuring the optical density (OD) of the exposed area, the absorbed dose can be determined.

RCF is sensitive to photons and electrons, but heavy particles such as protons with their large value of $\frac{dE}{dx}$, deposit a much larger dose in the thin active layer. It has been experimentally confirmed, by comparisons with stacked CR-39 detectors, that the blue region on the RCF corresponds to the profile of the emitted protons. The electron signal is visible in some cases, but only as a weak halo. If a stack of RCFs is employed, the greater range of the energetic electrons also makes it possible to discriminate between the two signals. The shape of the electron signal does not change from one layer of RCF to the next, but the proton signal does.

Attractive features of RCF are that the polymerization is a relatively fast process which does not require development, and the analysis is a straightforward OD measurement. On the other hand, the film requires a fairly high dose to react appreciably, and it is thus not suitable for experiments with low-energy lasers ($\sim 1\,\mathrm{J}$), such as the Lund multi-TW laser. Also, care must be taken not to inadvertently expose the film to UV radiation from, for example, fluorescent lighting.

4.7.4 Alternative detection methods

The successful adaptation of a micro-channel plate (MCP) as a proton detector has been reported [79]. MCPs are somewhat difficult to handle; they require very high vacuum and are susceptible to radiation damage. They are also rather expensive, and should therefore be placed behind a spectrometer to shield them from electrons and photons.

Another alternative is to make use of the fact that the accelerated protons are not relativistic, and therefore have an energy-dependent velocity. A setup based on time of flight using a fast radiation-sensitive diode and an oscilloscope can then be used.

4.8 Instruments

4.8.1 Filter stacks

To obtain energy selectivity when using CR-39 detectors, the fact that protons have a well-defined range in solid matter can be used. Placing an aluminum foil of known thickness in front of the detector ensures that only protons with energies above a certain threshold gets through. If several foils of a certain thickness and of successively narrower width are placed on top each other, a stepwise energy response can be obtained.

Up to ~ 6 filters are practical. By making the difference in width between filters reasonably large, a portion of the spatial profile in each energy interval is recorded. The filter stack can then be seen as a trade-off between energy resolution and spatial profile information, a feature exploited in the experiments described in Papers V, VI and X.
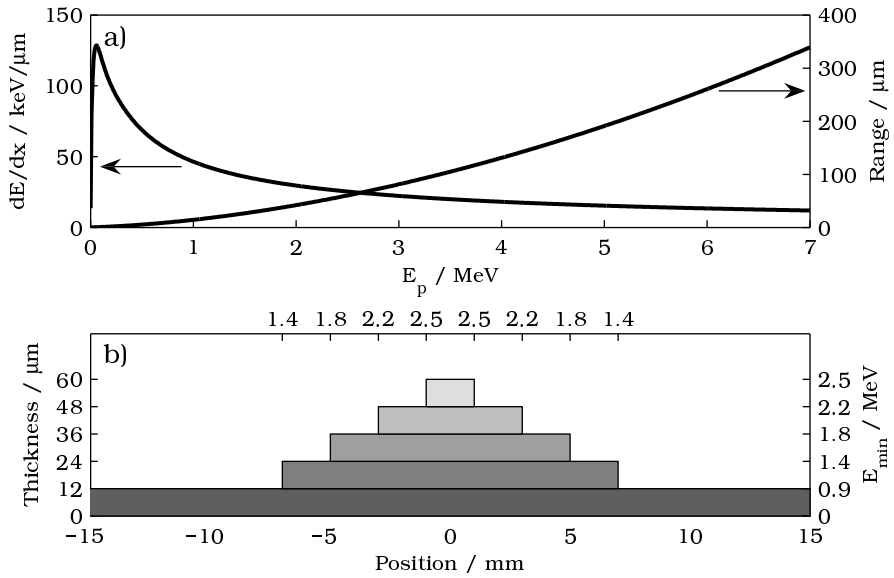
Figure 4.8: In a), the energy loss per unit (left axis) length and range (right axis) of protons in Al are plotted as a function of kinetic energy. Most of the proton energy is deposited near the end of its trajectory. Step filters used for recording spatial and energy distributions simultaneously are illustrated in b).

4.8.2 Magnetic spectrometers

To obtain the continuous energy distribution of the proton beam, a magnetic spectrometer can be used. Figure 4.9 shows a simulation of the magnetic field distribution in the spectrometer used in the experiments described in Paper VII. The simulation accuracy was confirmed by Hall probe measurements, and was found to be within a few percent. With such a homogeneous field, analytical calculations of the dispersion are possible.

Since the response of CR-39 plates, commonly used as detectors after the spectrometers, decrease with increasing energy (the pits become smaller), high-energy protons benefit from being slowed down just before hitting the detector. By calculating the deflection of protons with various energies in the spectrometer, foil filters with a suitable thickness to slow down the incoming particles, can be placed on the CR-39 at the appropriate locations.

4.8.3 Thomson spectrometers

In heavy-ion acceleration experiments, it is necessary to separate the different ion species before they reach the detector. Although the pit size in CR-39 contains some information on the size of the energetic particle, it cannot be used in practice as the resolution is limited and the calibration would be very complicated.
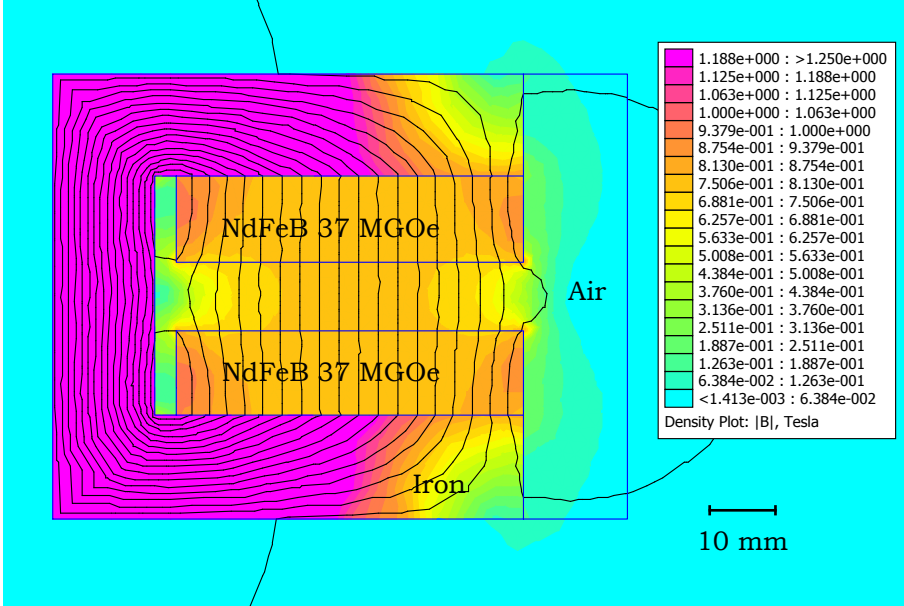
Figure 4.9: Magnetic field in the magnetic spectrometer used some of the experiments (Paper VII), simulated with the freeware program FEMM.

A solution is the Thomson spectrometer (sometimes referred to as a Thomson parabola), the idea for which was originally published in 1911 [80]. It features parallel magnetic and electric fields to disperse the particles according to their charge-to-mass ratio as well as their energy. In this case, the fields are assumed to be along the x-axis, with the particles traveling in the direction of the positive z-axis. Because the deflection of the (non-relativistic) particles scales as $\Delta x_E \sim \frac{q}{m} \frac{W}{m}$ and $\Delta y_B \sim \frac{q}{m} \sqrt{\frac{W}{m}}$ in the electric and magnetic fields, respectively, ions with a specific value of $\frac{q}{m}$ will trace out a parabolic curve on a 2D detector. Note that this means that some ion species, e.g. O^{4+} and C^{3+}, will overlap.

In the ion acceleration experiments presented in Papers IX and XI, a specific Thomson spectrometer configuration was used [81]. As considerable effort was devoted to both the construction of the spectrometer and the analysis of the output, they will be described in some detail here.

To enable a large deflection in the electric field direction, and still maintain high field strength, the instrument was designed with wedge-shaped electrodes. The resulting electric field is not homogeneous, but varies linearly along the length of the electrodes. Since all ion energies experience the same linear field distribution (for small deflections this is a good approximation in this case), it is still possible to assume an effective homogeneous field for the purpose of calculations. The electrodes act as an antenna for the EMP generated during a shot on a solid target. In addition, accelerated electrons will hit the positive plate and charge it up. These effects, if not remedied, lead to massive fluctua-

tions in the deflection of the ions. A high-voltage capacitor was added between the electrodes to act as a charge reservoir, which provided stable operation with only a slight ripple in ion tracks.

The magnets are recessed in the iron yoke to reduce fringe fields. The presence of fringe fields can be regarded as an energy-dependent misalignment of the spectrometer. Unfortunately, this configuration resulted in an inhomogeneous field distribution. It can be approximated by adding a linear term to the magnetic field, but the exact value depends on the relative positions of the entrance pinhole and magnets.

The spectrometer has a rotating CR-39 detector holder, enabling up to four consecutive shots without having to change the detectors.

After developing and counting the pits in the CR-39 detectors, the data can finally be analyzed. Raw data from a typical shot, together with simulated traces for selected ion species, can be seen in Figure 4.10. The presence of a neutral spot helps in the placement of the origin. It consists of neutral atoms that have recombined in flight before reaching the field region. Without a neutral spot, which is normally the case when the spectrometer is placed at an angle to the target normal, the accuracy of the analysis is substantially reduced.

Each x–y coordinate in the detector plane corresponds to a specific combination $\frac{q}{m}$ and $\frac{W}{m}$. A mapping can then be created between the two coordinate spaces (see Figure 4.11). Since a shot normally produces several hundreds of thousands of pits on the detector, a fast transform routine is needed. This was achieved by interpolation between points in a coarse map stored in the computer memory.

4.9 Experimental results

In this section, some of the experimental results presented in the Papers on proton and heavy-ion acceleration (Papers V–XI) are summarized.

4.9.1 Shock-induced target deformation

As has been described in previous sections, the ASE pedestal can send a shock wave through the target before the main pulse arrives. The effect of this shock wave on proton acceleration conditions at the back surface of the target was studied in detail using the Lund multi-TW laser (Papers V and X).

As an example, the particular case of a $6\,\mu$m thick aluminium target is summarized here. A typical ASE level of $10^{12}\,\mathrm{W/cm^2}$ gives a shock wave velocity of $8\,\mu$m/ns, calculated with Eqn 4.2 (see also Figure 4.12). The shock then takes less than one ns to traverse the target, and some effect of the ASE can be expected on the back surface. The temperature behind the shock becomes $1.1\,\mathrm{kK}$, which is much lower than the melting temperature at this pressure (see Figure 4.4). After breakout, the rear surface starts to move at twice the particle velocity, i.e. $4\,\mu$m/ns in this case (Figure 4.12). In general, the shock wave passes through the target quite quickly, but the expansion velocity depends strongly on the pressure and thus on ASE intensity. With these values in mind, it seems
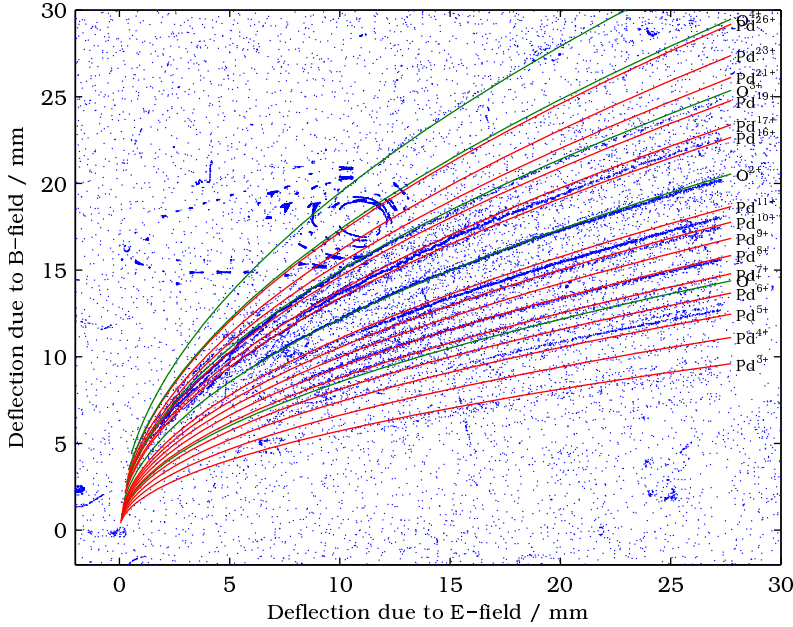
Figure 4.10: Typical output from the analysis program. The solid lines are simulated traces for selected ion species. The "blotch" at $(0.012, 0.0175)$ is an artifact (dried etching residue). This particular CR-39 plate is from the Thomson spectrometer along the target normal, back surface, during the Vulcan PW experiment described in Paper XI. The laser parameters for this shot were $E_L = 122\,\text{J}$, $\tau_L = 1\,\text{ps}$.

likely that an ASE duration of a few ns will result in a significant deformation of the back surface, without disrupting the sharp solid–vacuum boundary.

This was indeed observed, as can be seen in Figure 4.13. When the duration of the ASE pedestal was increased from 1 ns (the minimum value for the laser system) the higher energy protons were shifted progressively from the target normal direction towards the laser axis. In general, although this is not clearly visible in the figure, the divergence of the low-energy protons increased when the impact of the ASE increased.

The two hot electron populations described in Section 4.2, having different directions, explain this energy-dependent deflection. Since the experiment was performed at a $45°$ angle of incidence, the $\mathbf{v} \times \mathbf{B}$ heated electrons were driven in this direction, while the electrons heated by resonance absorption travel along the target normal. An asymmetric electron sheath was then formed on the back of the target. At the laser intensities considered here, the $\mathbf{v} \times \mathbf{B}$ heating mechanism dominates, producing the hottest electrons [57]. It can then be expected that the most energetic protons originate from this area.

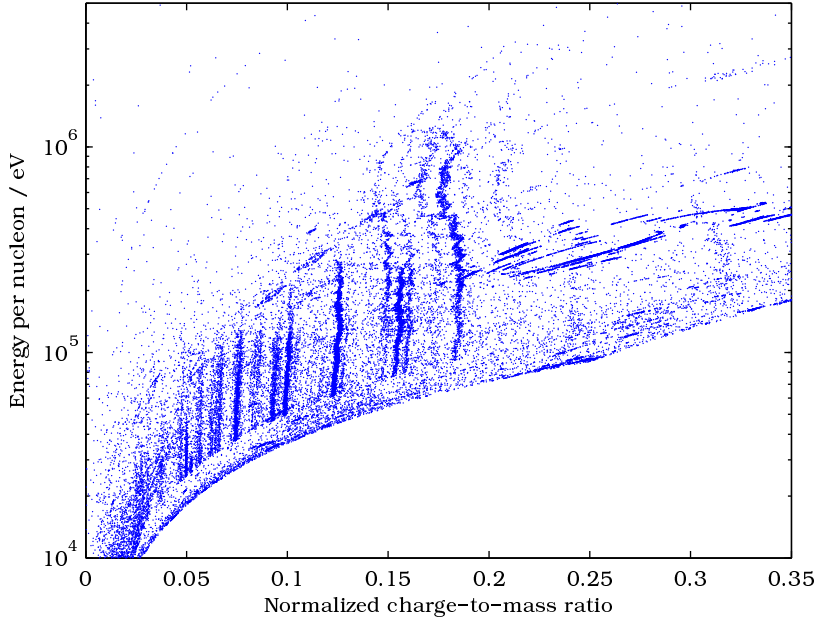The laser-induced shock wave, on the other hand, is launched in the tar-

Figure 4.11: The x–y spatial distribution in Figure 4.10 can be transformed into $\frac{q}{m}$–$\frac{W}{m}$ space for further analysis. The electric field in the Thomson spectrometer was modulated by the EMP and electrons hitting the electrodes. This is seen as wiggles in the traces, and is pronounced at higher ion energies.
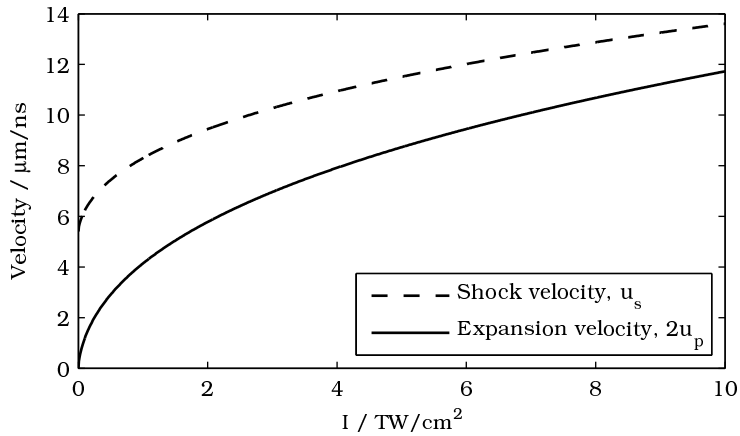

Figure 4.12: Shock and expansion velocity curves for aluminium. For zero laser intensity, the shock velocity equals the sound speed, c_0, of the material, whereas the expansion velocity goes to zero.
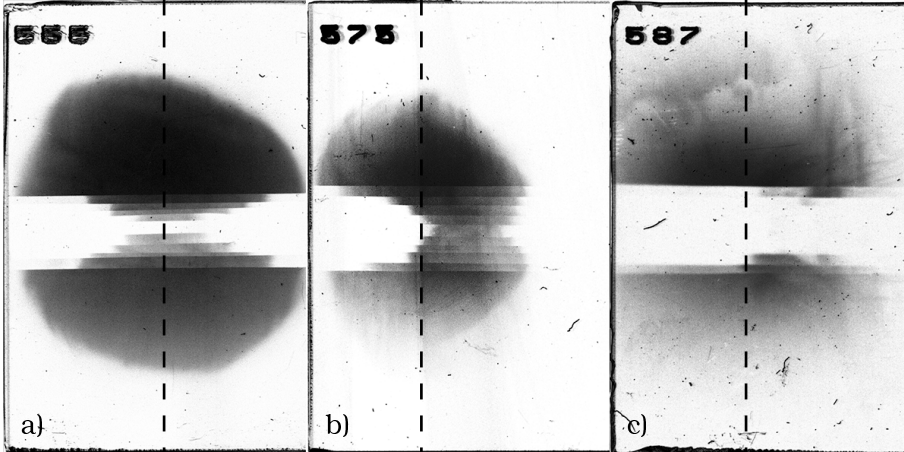
Figure 4.13: Typical example of proton beam profiles, where a filter stack was used to provide some energy information. In a), the ASE level (10^{-8}) was low enough and the ASE duration (1 ns) short enough that shock deformation is negligible. In b) the ASE level was increased (1.5×10^{-7}) and significant deformation is evident. Finally, in c), the ASE duration was increased (3 ns) to the extent that the back surface disrupted. The dashed line in each panel shows the horizontal direction of the target normal. The target was a 6 μm thick aluminium foil. Laser parameters were: 0.7 J on target during 35 fs, focused to a 5 μm FWHM spot. Note that the filter stack used for the shot in a) was different, with a maximum energy of 4.4 MeV, from the one for b) and c). There, the maximum energy is only 2.8 MeV.

get normal direction, and the deformation of the back surface of the target is centered around this axis. As can be seen in the schematic in Figure 4.14, the expected direction of travel of the higher energy protons is then towards the laser axis.

A similar effect was obtained by increasing the ASE intensity (and thus the target expansion velocity after shock wave breakout) for a fixed ASE duration. The intensity cannot be increased too much as the target will evaporate, and the conditions for efficient proton acceleration will be destroyed. When both the duration and intensity of the ASE pedestal were kept constant, and the target thickness was decreased, an energy-dependent deviation was observed below a certain thickness.

Note that this type of experiment is made possible by the use of a spatial beam profile detector, instead of a spectrometer with an entrance pinhole. Under these experimental conditions, the use of a spectrometer with a pinhole placed in the target normal direction would result in the highest-energy protons being undetected altogether.
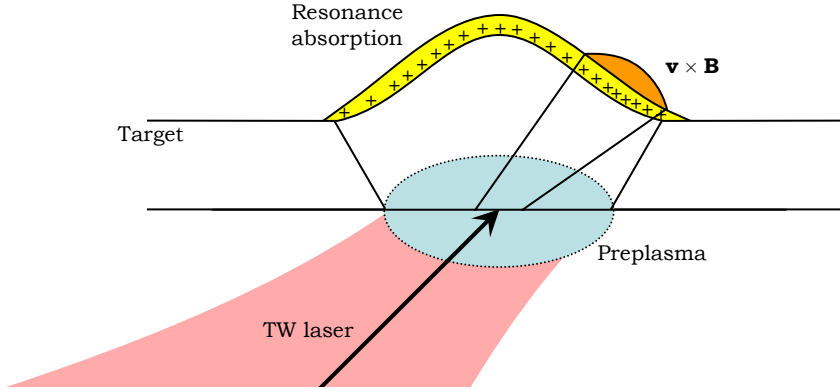
Figure 4.14: Schematic of the generation of asymmetric proton beams. The two hot electron populations generated by the laser–plasma interaction on the front of the target give rise to an asymmetric electron sheath at the back of the target. The electron density is locally enhanced where the energetic $\mathbf{v} \times \mathbf{B}$-heated electrons emerge. This leads to higher-energy protons from that area. Since the target has been deformed by the ASE-induced shock wave, the target normal points towards the laser axis here.

4.9.2 Ultra-thin foils

The idea of electron recirculation makes it very interesting to study thin targets. This was the objective of the the experiment reported in Paper VII. Given the ~ 35 fs pulse duration of the Lund multi-TW laser, which was used for the experiment, a thickness less than $\sim 4\,\mu$m was needed to observe the effect. To eliminate ASE-induced deformation of the back surface, a plasma mirror was placed just before focus, improving the contrast to 10^{10}. The plasma mirror enabled us to use targets as thin as 20 nm and still obtain energetic proton beams. A parametric study of proton acceleration as a function of target thickness, spanning three orders of magnitude, is reported in Paper VII.

By using a CR-39 filter stack sampling the bottom half of the beam, and two magnetic spectrometers simultaneously, the beam profile was estimated as a function of energy by making certain assumptions. The beam cross section was assumed to be circular and the energy spectrum maxwellian along the target normal direction. The number of protons of a certain energy was assumed to decrease linearly as a function of the divergence angle, with a slope determined from the CR-39 filter stack. A measure of the total conversion into energetic protons (the energy threshold was set at 0.9 MeV, the minimum energy detectable by the filter stack) was obtained from the integrated energy distribution.

A clear optimum thickness, at around 100 nm, was observed both in terms of maximum energy (Figure 4.15) and conversion efficiency. The enhancement for thinner targets, while not as pronounced as in a previous study [59], may be the result of recirculation of hot electrons during the laser pulse. There was
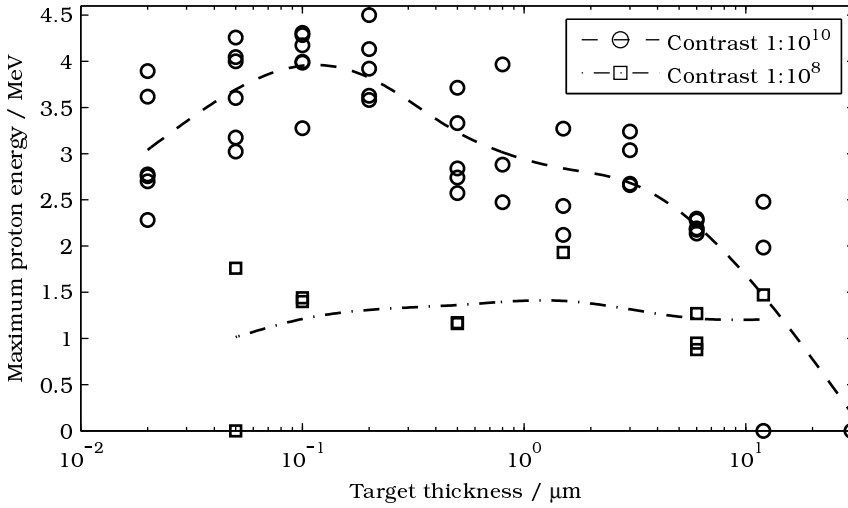
Figure 4.15: Maximum proton energy as a function of target thickness. Data for both high contrast with plasma mirror (circles) and lower contrast (diamonds) are included. The laser energy on target is kept constant at 300 mJ (note that this is a very low energy). The low-contrast shots all have lower maximum proton energy than a high contrast shot on a target with the same thickness.

no clear leveling off for targets thicker than the recirculation time. This can be understood by considering the spreading of hot electrons as they traverse the target bulk. Geometric expansion gives a charge density at the back of the target that decreases with increasing target thickness. If the focal spot is 6 μm at FWHM, and the generated electrons have a 30° divergence, this effect can be expected to play a role for targets thicker than a few μm.

4.9.3 Scaling of proton energy at very high intensities

Previous studies of the scaling of maximum proton energy as a function of laser intensity have revealed a $E_{max} \sim \sqrt{I}$ dependence [82], corresponding to the scaling of the hot electron temperature with the ponderomotive potential in the ultra-relativistic regime. In the experiment described in Paper VIII, the experimental parameter range is extended to laser intensities up to 6 × 10^{20} W/cm^2, available at Vulcan PW. The square root dependence on intensity is confirmed by the data, but the absolute energies were lower than predicted by a simple plasma expansion model [83, 84].

The 1D analytical plasma expansion model in [84] has been widely used to predict proton acceleration, although it has some serious limitations. For example, the cooling of the hot electrons as the acceleration progresses is not taken into account, leading to a diverging maximum energy of the protons. To obtain a finite maximum proton energy, acceleration is usually terminated after a time $\kappa\tau_L$, where κ is a fitting parameter with a value ~ 1 [61] and τ_L is

the laser pulse duration. This is clearly not a good estimate for a short-pulse laser, where the electron cloud is generated very quickly on the timescale of the laser pulse duration. Most of the acceleration then takes place in the ensuing plasma expansion on the much longer timescale of the inverse of the ion plasma frequency [85]. Compared to the extended model in [85], which includes a dynamic electron temperature, the previous model in general overestimates the proton energy.

In the present work it was found that even with the extended plasma expansion model, the maximum predicted proton energy is much higher than the experimental (by a factor of 2). This is discussed in Paper VIII. By extending the plasma expansion model even further, to include lateral expansion of the electrons, the accelerating fields are further reduced. This reduction is only applied conceptually, by stopping the acceleration after an acceleration distance corresponding to the extent of the focal spot.

4.9.4 Heavy-ion acceleration

The heavy-ion acceleration experiment presented in Paper XI resulted in a huge amount of data, due to the deployment of six simultaneously operated Thomson spectrometers: three on each side of the target, along the target normal and at $\pm 10°$. The experiment was conducted at a 45° angle of incidence, with laser energy and pulse duration systematically varied from 41 to 350 J and from 1 to 8 ps, respectively, to cover a large parameter space.

Palladium, in the form of 25 μm thick foils, was used as target material due its good ion acceleration properties [62], i.e. it has a low tendency to form oxides and releases its hydrogen content when heated. The number of protons was much reduced compared to unheated targets and only very weak traces of carbon were seen. However, the most prominent tracks always originated from oxygen ions from the heated target, although many charge states of palladium were also observed.

In the paper we report what appears to be a $\sqrt{I}$ dependence of the maximum ion energy. The shielding of ions with lower $\frac{q}{m}$ by the more swiftly accelerated ions with higher values of $\frac{q}{m}$ is quite evident.

Typical examples of observed target normal ion spectra are given in Figure 4.16. Ions ejected from the front surface have higher charge states than their back surface counterparts. This is due to the immense field strengths in the laser pulse that are encountered at the front surface. Somewhat surprisingly, ions from the front also had higher maximum energy than those from the back. The back surface TNSA is thought to produce higher accelerating fields than the Coulomb explosion at the front, but this is not the case here. The conditions at the back of the target could have been disturbed by the ASE pedestal, although the foil was sufficiently thick for ASE-induced effects not to be expected to interfere with the TNSA mechanism.

The energy of lower mass ions is in general higher than that of higher mass ions with the same charge-to-mass ratio (see Figure 4.16). When subjected to the same accelerating fields, they would experience the same acceleration and should attain the same energy per nucleon. However, for a given electric field, the lower mass atoms are ionized to a higher value of $\frac{q}{m}$ (see Figure 4.17), and
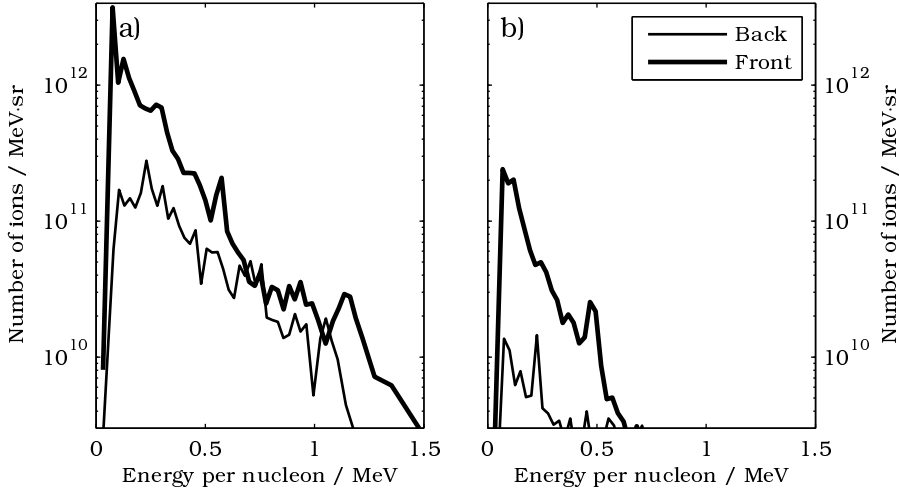
Figure 4.16: Target normal spectra for heavy ions. Panel a) shows O^{3+} from the front and back surfaces, and b) shows Pd^{19+}. Both ion species have similar values of $\frac{q}{m}$ (0.19 and 0.18, respectively, in normalized units), but both the maximum energy and number of ions are clearly much lower for palladium than for oxygen. Laser parameters for this shot were $E_L = 122\,\mathrm{J}$ and $\tau_L = 1\,\mathrm{ps}$.
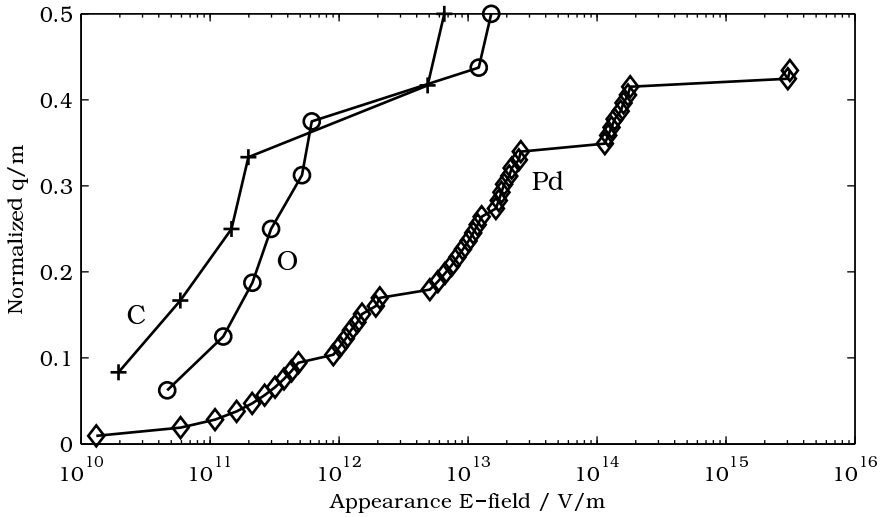

Figure 4.17: Appearance electric field of some of the ions detected in the experiment discussed in Paper XI (compiled from data in [86]). The vertical axis shows the normalized charge-to-mass ratio to emphasize the accelerability of the lower mass ions. The discontinuities in the graphs correspond to closed electronic shell configurations.

are hence accelerated to higher energy per nucleon. An additional effect favoring oxygen acceleration, is that the oxygen atoms are located on the surface of the target. Once ionized, the oxygen ions shield the electric field, generated by hot electrons, from the lower lying layers of palladium atoms. This effect has been seen in simulations [87].

The output from the off-axis Thomson spectrometers has a large uncertainty, due to the lack of a neutral spot on most of the CR-39 plates. This makes it difficult to draw precise quantitative conclusions from the recorded spectra. However, it appears that the maximum ion energy is often higher off-axis. Spectra from the off-axis spectrometers often have strange non-maxwellian distributions, indicating a complex angular dependence of the accelerating fields.

We also observed asymmetry in the ion beam from the front surface towards the incoming laser axis. This asymmetry was more pronounced for longer laser pulse durations. A possible cause is that the laser deforms the plasma at the surface through ponderomotive push, locally changing the surface curvature.

4.9.5   Edge emission effects

On some of the shots in the ion acceleration experiment, several emitting sources were observed. This was particularly evident when looking at the neutral spot; see Figure 4.18 for a typical example. In this case the Thomson spectrometer can be regarded as a pinhole camera. It is then possible, by knowing the magnification, to project the observed pattern back to the source. Apart from emission directly behind the laser focal spot, the edges of the 4 mm wide target foil also emitted energetic ions. The cause of this is the hot electrons from the laser-plasma interaction spreading along the surface of the target. The electrons tend to concentrate at sharp density boundaries, resulting in a locally increased electric field.

Multiple ion tracks were also seen on the CR-39 detectors. As they emanated from specific source points, the ion species and their energy distributions could be identified. This information was used to infer the maximum electric field strength present at the emitting edges, by comparison with the known appearance electric field for different ion species (Paper IX). If, for example, we see O^{2+} but not O^{3+}, the field must be between 0.13 and 0.21 TV/m (data available from Figure 4.17). The technique of using the Thomson spectrometer as a pinhole camera offers an interesting diagnostic tool for extended sources, providing both imaging and spectroscopic information.
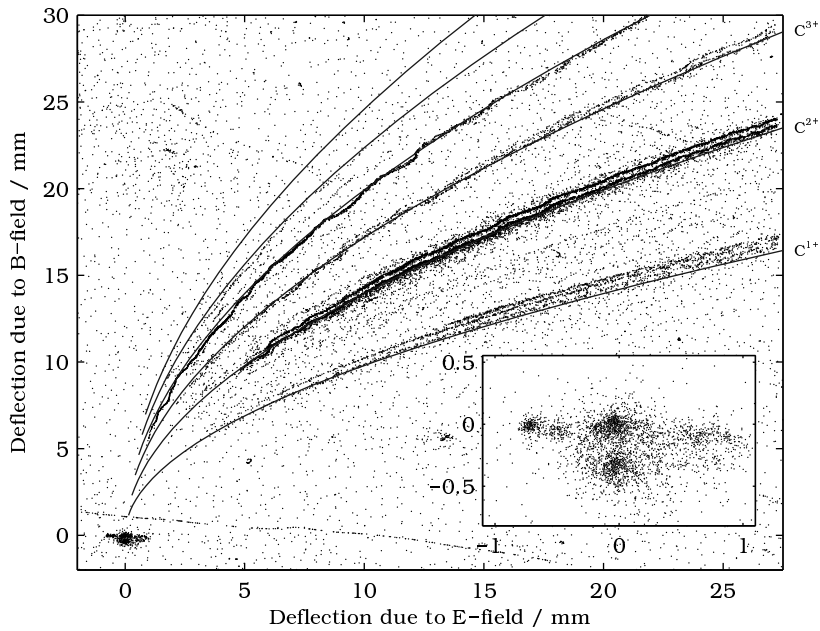
Figure 4.18: Example of multiple sources, showing as carbon tracks with split traces, in particular for the ones with lower charge-to-mass ratio. Inset is a zoomed in view of the neutral spot. Four distinct emitting regions are clearly visible. The details for this shot are: $E_L = 340\,\mathrm{J}$, $\tau_L = 1\,\mathrm{ps}$, $10\,\mu$m gold target.

SOFT X-RAY LASER EXPERIMENTS

5.1 Introduction

The region of the electromagnetic spectrum between several tens of nm down to about one nm is called the soft X-ray regime. It is interesting for applications such as lithography, biological imaging (in the so-called water window, 2.2–4.4 nm) and holography, among others. Following the first demonstration of a soft X-ray laser (SXRL) in 1985 [88], this field of research has evolved steadily. Two comprehensive reviews of plasma-based X-ray lasers are found in [89] and [90].

To obtain electronic transitions with short wavelengths, highly charged ions are needed. This means working in a plasma medium, preferably with a controlled ion species distribution. Popular lasing transitions, for SXRLs that use collisional excitation, include $2p^5\,3p - 2p^5\,3s$ in neon-like ions, and $3d^9\,4d - 3d^9\,4p$ in nickel-like ions. These two types of ions have closed sub-shell ground state electron configurations, with 10 and 28 electrons, and therefore appear in abundance for a range of plasma temperatures and densities. The nickel-like ion transition has the advantage over the neon-like that it has a shorter wavelength for a given ionization state. The lasing wavelength can then be selected by changing the target material. For example, yttrium produces $\lambda = 24.0$ nm [91] and tungsten $\lambda = 4.3$ nm [92] for nickel-like ions.

In general, SXRLs are produced by ASE in a single pass through the amplifying medium.

5.2 Transient collisional pumping

The lifetime of an excited state, τ, scales as λ^{-2}, and the pump power needed to obtain a specific gain coefficient, g, scales as $g\lambda^{-5}$ [90]. Therefore, X-ray lasers must be pumped very hard to overcome spontaneous emission. This can be done with brute force using high-energy lasers, which are expensive and have low repetition rates. Alternatively, by using a traveling pump wave, the gain can be applied only to the X-ray laser pulse, saving a great deal of energy, and

the pump laser can be scaled down considerably, to a few joules. This technique is called transient collisional pumping [93].

The plasma is first created by a long (hundreds of ps) pulse, focused to a line, and allowed to expand for some time. The interesting ionization stages are then populated and a smooth plasma gradient is created. A smooth gradient is needed to prevent the X-ray laser beam from being refracted out of the gain region. After a specific time, a much shorter (~ 1 ps) pump pulse arrives, heating the plasma and producing a population inversion through electron collisions. The gain is present for a very short time, so the pump pulse has to follow the SXRL pulse as it is amplified. This is accomplished by using a traveling pump wave.

5.3   GRIP

In the transient collisional pumping scheme, the direction of the pump laser is perpendicular to the target. The region of overlap between the laser and the lasing ion species is then very short. The coupling can be improved by directing the laser so that it is incident at a grazing angle, so-called grazing incidence pumping (GRIP) [94]. The pump pulse will then be continuously refracted in the plasma density gradient. The electron density at which the pump turns over depends only on the grazing angle, φ, and the laser wavelength (through the critical density n_c) according to [95]:

$$n_e = n_c sin^2\varphi. \tag{5.1}$$

As the pump pulse is refracted, the path length in the gain region is increased. The process is schematically depicted in Figure 5.1. An extra advantage is that the incoming beam creates a traveling pump wave with a speed close to the speed of light, and no measures must be taken to achieve this.

Saturated soft x-ray lasing using the grazing incidence geometry, has been reported using less than a joule of pump energy ([94] and Paper XIII).

5.4   Experimental setup

In the experiments reported in Papers XIII and XIV, the experimental setup illustrated in Figure 5.2 was used. The target consisted of a 4 mm wide piece of molybdenum, producing X-ray lasing at 18.9 nm (66 eV) from nickel-like Mo^{14+}. The plasma-forming long pulse was focused to a 70 μm×5 mm line by a spherical and a cylindrical lens. The pulse was extracted after the last amplifier in the Lund multi-TW laser and used uncompressed ($\sim$ 250–300 ps). A rotatable $\lambda/2$ wave plate followed by a polarizer made it possible to continuously vary the relative energy content in the long pulse and the short pump pulse. The short (ps duration) pump pulse was focused by an on-axis spherical mirror used off-axis. This gave an astigmatic focus, i.e. a 40 μm wide line.

To improve the efficiency of the plasma-forming pulse, a low-energy pre-pulse was introduced in the long-pulse arm through a polarizing beam splitter/combiner. The energy in the prepulse could be varied relative to the long pulse, but was normally 7.5%.
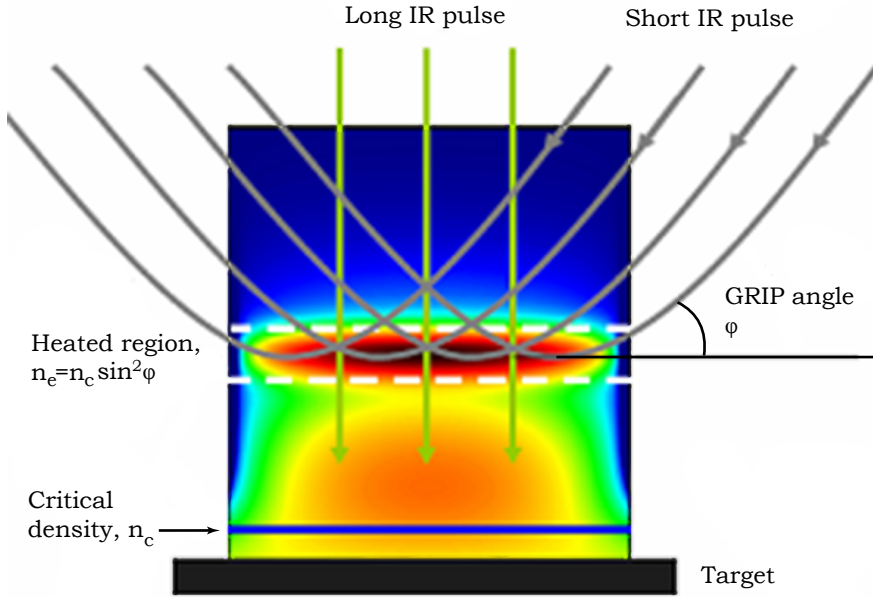
Figure 5.1: Schematic of the GRIP process. A smooth plasma gradient is created by the long prepulse. At some distance from the target surface, the lasing ion species appears in abundance. By varying the angle of incidence, φ, the electron density at which the pump pulse turns over can be selected. The electron density and the distance from the target are related through the time delay between the two pulses. The color scale in the figure depicts the electron temperature (image courtesy of K. Cassou).

An integral part of the experiment was the study of the SXRL output as a function of φ. Normally, this is accomplished by simply tilting the target (see, e.g., [96]), but this also changes the conditions for the long pulse. Instead, the spherical mirror and the last steering mirror were motorized (see Figure 5.2), allowing the angle of incidence to be varied separately from the other parameters.

To ensure that the two line foci were overlapping, the target could be removed and replaced with a ground glass plate. The scattered light from the two beams (heavily attenuated) could then be observed with a microscope objective connected to a camera. The resolution of this setup was limited by the grains in the glass, $\sim 1\,\mu$m in this case. This procedure was repeated after each change in the focusing setup, such as changing the GRIP angle.

The main diagnostic tool used in the experiment was a near-field imaging camera. The exit mode of the SXRL beam was imaged by a curved multilayer mirror onto a back-thinned CCD camera. The beam was attenuated with a series of selectable aluminium filters with thicknesses in the range 1–6 μm,
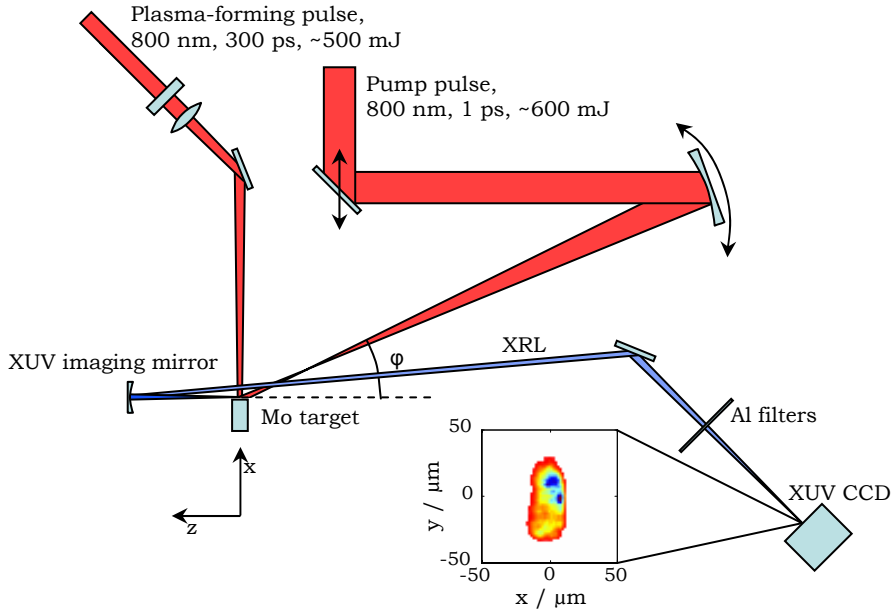
Figure 5.2: Schematic, adapted from Paper XIV of the setup used for the SXRL experiments. The inset shows a typical beam profile obtained with the near-field imaging detector.

corresponding to transmissions of 1.6×10^{-1}–1.5×10^{-4} [97] (including 15 nm of Al_2O_3 on each filter surface). The response of the camera was known through calibration at a synchrotron source. This enabled absolute calculation of the fluence of the soft X-ray laser from the number of counts in each camera pixel.

Additional diagnostic tools included a hard X-ray pinhole camera that viewed the interaction from above. Its purpose was to correlate the position of the gain region as imaged by the near-field camera with the emission of X-rays from hot electrons. A spectrometer was employed to verify that the SXRL was indeed emitting at the correct 18.9 nm line.

5.5   Results

5.5.1   GRIP optimization

A large parameter space was investigated to determine the optimal conditions for SXRL output: GRIP angle, total pump laser energy, relative energy long/short pulse, time delay long/short pulse, and prepulse energy. The results (see Paper XIII) are briefly summarized below.

For a given long pulse energy setting, there is an optimum time delay between the long and short pulses. This is because the expansion velocity of the plasma plume increases with increasing laser energy. The optimum delay is shifted to shorter values for higher values of φ. A pumping beam with a lower
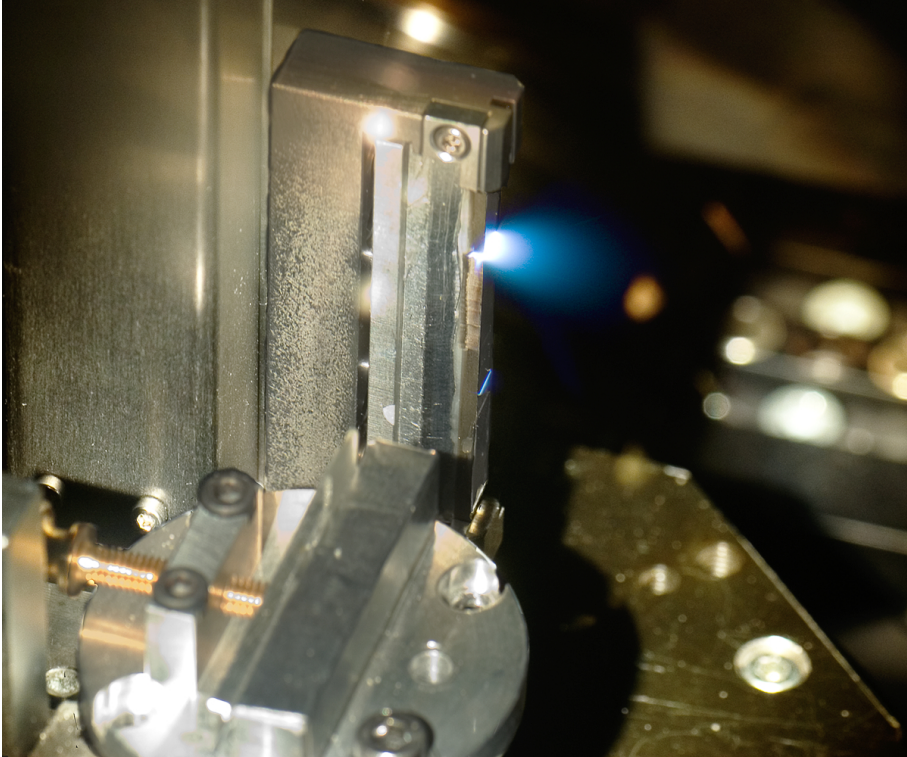
Figure 5.3: Photograph of the laser–plasma interaction in the SXRL experiments described in Papers XIII and XIV. The blue plasma plume generated by the long pulse laser, focused to a line, extends out from the 4 mm wide molybdenum target. The length of the target is 50 mm, allowing several thousand shots before a change is needed. In the foreground, the ground glass plate used to check the overlap of the two driving laser pulses is visible in its holder.

φ is absorbed at a lower electron density, and a longer time is needed for the desired ion species to be populated.

It can be seen in Figure 5.4 that the maximum SXRL output energy is obtained for $\varphi = 19°$. If the angle is small, according to Eqn 5.1, the turning point takes place at a low electron density with a correspondingly small gain. On the other hand, for a greater angle φ, the larger electron density provides higher gain, but at the same time the pump pulse penetrates deeper into the plasma and is exposed to a steeper density gradient. The soft X-ray laser pulse is then refracted out of the gain volume more quickly.

The pulse energy of the SXRL was measured at optimum conditions and found to be $3 \, \mu$J. This is remarkably high in this context, since the total energy of the pump laser was only ~ 1 J (500 mJ in the long pulse and 600 mJ in the short pulse).
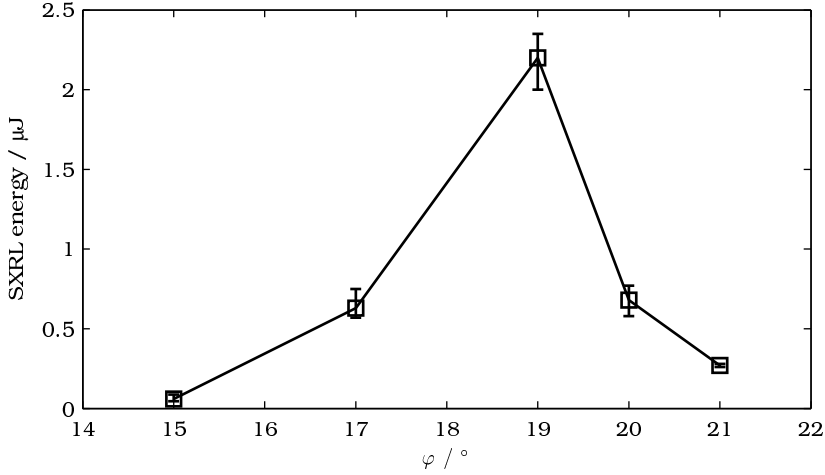
Figure 5.4: Output energy of the soft X-ray laser for optimum delay between the long and short pulses as a function of GRIP angle. There is a clear optimum at $\varphi = 19°$; the energy falling significantly just two degrees on either side of this angle.

5.5.2   High repetition rate operation

The experiment can easily be run at the full 10 Hz repetition rate of the driving laser, as the target does not need to be realigned after every shot. The diagnostic systems, being electronic, also support data acquisition at this rate.

In a series of tests (Paper XIV), the near-field camera was set to record a 46×41 pixel region of interest to enable 10 Hz operation. The target was then either moved continuously at a slow rate, or remained stationary, with the driving laser firing at 10 Hz. With a moving target the SXRL source remained roughly in place, within a $15\,\mu$m shot-to-shot jitter. When the target was stationary, the ablation of target material by the IR laser created a crater and the position of the SXRL exit mode moved steadily inwards towards the target. The rate of movement was $\sim 0.25\,\mu$m/shot. After about 100 shots, the source started to disappear from the field of view of the camera, thus limiting the duration of the sequence. The target was examined with a surface profilometer, and the depth of the crater correlated well with the observed movement of the source. In addition to the expected movement of the source position, towards the target, it was also seen to move slightly upwards. This was quite unexpected, as both driving lasers were in the horizontal plane. No explanation has yet been found for this upward migration.

The SXRL output energy was measured (by integrating the near-field images) for every shot. The moving target produced a steady soft X-ray laser, but with large shot-to-shot fluctuations in energy. When there was no target movement, the average energy increased. The increase lasted for around 50 shots, and then leveled off. A possible explanation of the increase in energy is
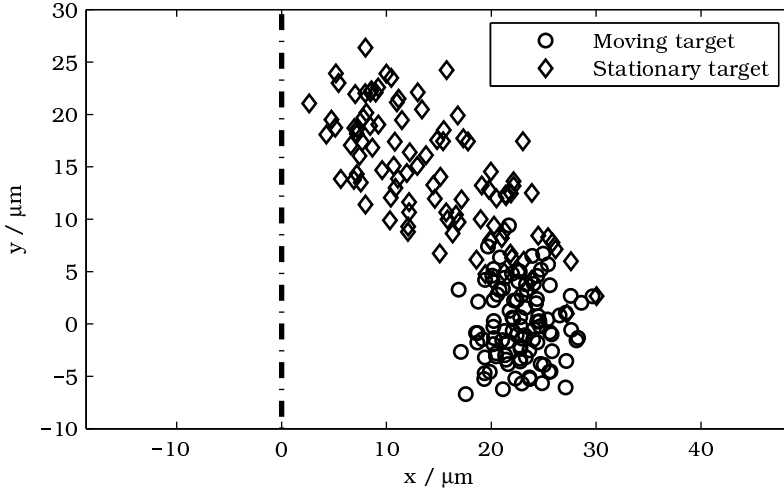
Figure 5.5: Position of the centroid of the near-field beam profile for a moving target (circles) and a stationary target (diamonds). The dash-dotted line represents the original target surface. For a moving target, the position is well contained within a $15\,\mu$m circular region. When the target is stationary, the laser begins to ablate a crater in the target, causing a shift in the position of the SXRL source.

that the line-shaped crater formed by laser ablation could provide a guide for the X-ray laser along the length of the target [98]. At some point, the energy would cease to increase when the crater is too deep, but the limited number of shots recorded on the same target position did not enable us to confirm this.

The large fluctuations in energy were probably due to pointing jitter of the driving laser. The short-pulse focal width was $40\,\mu$m and with an estimated $15\,\mu$m peak-to-peak variation in the position, significant energy fluctuations can be expected.

If the SXRL is operated in saturation, the effect of variations in energy of the driving laser can be minimized. The pointing issue must then be solved, e.g. by using a wider focal spot and adding more vibration damping to the system. In the experiment described here, the long- and short-pulse beams propagated several meters along different paths in the laboratory, reflecting off many optical mounts that could impart mechanical vibration.

OUTLOOK

Electron acceleration

The wakefield acceleration experiments described in this thesis show great potential, with reproducible generation of low-energy-spread electron beams. However, the shot-to-shot fluctuations in energy were quite large. We suspected (and later experiments have strengthened this suspicion) that the gas jet mechanism was largely responsible for these variations. This is clearly an area where large improvements can be made without too much effort.

Instead of using a gas jet, various types of wave guiding structures have produced promising results. These are more stable than gas jets and also make it possible to increase the interaction length. Discharge capillaries, with lengths of several centimeters, have been reported recently, in which electrons were accelerated up to GeV energies [99]. In a capillary, or in a preformed plasma channel, the electron density can be decreased below the threshold for self-focusing and the laser can still be guided. At lower densities, the dephasing length increases and the electrons can be accelerated to higher energies. By extending the acceleration length, energies reaching tens of GeV should become possible with present day's lasers.

At first glance, the relative energy spread in the accelerated beams appears to be quite large ($\sim 10\%$ ($\sim 10\,\mathrm{MeV}$) in Figure 3.9). However, since the electrons are highly relativistic, the short pulse duration of the accelerated bunch will be retained. This makes it possible to accelerate the electrons further while maintaining the *absolute* energy spread. At an energy of $10\,\mathrm{GeV}$, an energy spread of $10\,\mathrm{MeV}$ is not bad. The very short duration of the burst of wakefield accelerated electrons is also a very important asset when designing a free electron laser, where the peak current in the beam is a very important parameter.

Emission from betatron oscillations of the electrons in the ion channel [100] could provide an extremely compact X-ray source. In this scheme, the electrons accelerated in the wakefield also undergo betatron oscillations in the ion channel. Similar to in a wiggler in a storage ring, the electrons will emit a burst of radiation in a narrow beam near the turning points of the oscillation. In the experiments reported in [100] and [101], the number of photons was found to

depend on the laser energy squared.

Proton acceleration

Although the indirect nature of the TNSA mechanism makes it challenging to achieve high conversion efficiency, the very low emittance of the laser-accelerated protons is a key feature that makes it attractive. It is possible to focus the proton beam to a very small spot, resulting in a huge flux.

Various methods of obtaining quasi-mono-energetic proton and ion beams have been demonstrated, e.g. [79, 102], but so far none that actually concentrates the available energy in a narrow range. It has only been possible to remove protons outside of a small region on the target surface to ensure that they all experience the same accelerating fields. This separation could, however, equally well be done with a dispersive element, such as a magnet, followed by a slit. The challenge is to transfer the laser energy to protons within a narrow kinetic energy range without sacrificing the total conversion efficiency.

As laser technology advances, it should be possible to achieve the intensities needed to directly accelerate protons with light pressure, i.e. $I \geq 5 \times 10^{21} \, \text{W/cm}^2$. The technique looks very promising, indicating the possibility to achieve proton conversion efficiencies approaching unity [103].

Among the possible applications of laser-accelerated protons is radiation oncology. Already today, facilities are being built with the main purpose of developing a laser-based proton source for cancer treatment [104]. Proton energies of a few hundred MeV are needed—120 MeV protons have a range of 10 cm in tissue—to treat tumors deep inside the body. Less energy is required to treat tumors in the eye. The energy scaling with laser intensity reported in Paper VIII, tend to indicate that the interesting proton energies would require a very powerful laser. Improving the laser contrast, so that thinner targets could be used, would increase the proton energy and reduce the energy requirement of the driving laser to an extent. A proton beam with small energy spread and tunable energy is essential to be able to deliver a specific dose to a specific location. However, the energy spread should not be too small, to avoid the need for extensive scanning of the beam over the cancerous volume.

Considerably closer in time, is the production of isotopes for positron emission tomography through (p,n) reactions. The Q-values for interesting isotopes are a few MeV, energies already available with today's lasers. The positron emitters have very short half-lives, sometimes only a few minutes, which means that a low repetition rate laser cannot be used to accumulate dose. To increase the number of radioactive nuclides, it is important to have a high repetition rate laser with a high proton conversion efficiency. Thin targets, and hence a very good laser contrast, are therefore needed.

Soft X-ray lasers

The low pump energy requirements of GRIP, and the results on 10 Hz operation described in this thesis, make it very conceivable to operate a table-top high repetition rate soft X-ray laser as a turn-key device in the near future. The cost

of such a system would be potentially quite low compared to a synchrotron, and still provide comparable performance in some respects, such as peak brightness.

Further improvement of the soft X-ray source is possible by seeding the amplifier medium with a high harmonic beam. This improves the spatial coherence of the SXRL, and also serves to lower to pulse duration of the amplified beam [105]. Saturated amplification of a seeded soft X-ray laser at 32.8 nm, using transient collisional pumping, has recently been reported [106].

While not yet demonstrated experimentally, there is nothing fundamental prohibiting the extension of these techniques to the water window, where high contrast biological imaging applications are plentiful.

Comments on the Papers

I **Laser-wakefield acceleration of monoenergetic electron beams in the first plasma-wave period**
This paper describes an electron acceleration experiment using the Lund multi-TW laser, in which the elliptic beam profile of the mono-energetic electrons was used to infer properties of the acceleration mechanism.
I was involved in all parts of the experiment, including setup, running the laser and diagnostics, data analysis and also participated in the discussion of the manuscript.

II **Effect of laser contrast ratio on electron beam stability in laser wakefield acceleration experiments**
The stability of the laser-accelerated electron beam from two different lasers (Lund multi-TW and Astra (RAL)) were compared. It was found that better contrast has a large impact on fluctuations in both energy and electron beam pointing.
I took part in the experiments carried out with the Lund multi-TW laser, including setup, execution and data analysis.

III **On the stability of laser wakefield electron accelerators in the monoenergetic regime**
In this paper, the conditions leading to mono-energetic features in the electron spectra were investigated. Results from two different lasers (Lund multi-TW and Astra (RAL)) were compared. It was found that by matching the focusing and pulse duration of the driving laser to the plasma density used, significantly improved stability of the electron beam can be achieved.
I took part in the experiments carried out with the Lund multi-TW laser, including setup, execution and data analysis.

IV **Particle acceleration using the Lund multi-terawatt femtosecond laser**
Conference proceeding describing relativistic channeling, electron acceleration and proton acceleration experiments. These experiments were performed two years before the ones reported in papers I-III.
I performed large parts of the experiments, in particular the ones concerning electron and proton acceleration.

V **Laser-accelerated protons with energy-dependent beam direction**
Our findings on shock-wave-driven deformation on the back surface of solid targets, and their ability to steer the accelerated protons, are reported in this paper.
I was involved in the planning, setup and execution of the experiment, performed part of the data analysis, and took part in writing the manuscript, in particular producing the figures in the paper.

VI **High-intensity laser-driven proton acceleration: influence of pulse contrast**
Results concerning the influence of ASE on proton acceleration from foil targets are discussed in this paper.
I took part in the planning, setup and execution of the experiment, performed part of the data analysis, and produced several of the figures in the paper.

VII **Enhanced proton beams from ultrathin targets driven by high contrast laser pulses**
This paper describes an experiment on proton acceleration from very thin targets. A plasma mirror made it possible to use sub-μm thick foils and achieve high conversion efficiency.
I took part in the experiment and wrote the software used for the data analysis. I was also involved in the interpretation of the data and the writing of the manuscript.

VIII **Scaling of proton acceleration driven by petawatt-laser–plasma interactions**
In this study, scaling of the maximum proton energy, accelerated from a thin foil target by a laser, was extended to a new intensity range using the Vulcan PW laser. It was found that the proton energy increased less with intensity than predicted by simple plasma expansion models. Some of the discrepancies can be explained by more detailed modeling, including hot electron cooling and expansion.
I took part in the experiment and the contributed to the interpretation of the data.

IX **Lateral electron transport in high-intensity laser-irradiated foils diagnosed by ion emission**

This paper reports on the discovery of multiple ion sources on some of the shots during a heavy-ion acceleration experiment at Vulcan PW. The phenomenon is explained as being the result of hot electrons moving along the surface of the target, creating charge buildup at the edges. The hypothesis is confirmed by simulations.

I took part in the experiment, wrote the software used for the data analysis and performed part of the analysis.

X **Influence of shockwaves on laser-driven proton acceleration**

The results from the shock deformation experiments described in Paper V were extended and presented here in detail. In particular the modeling was improved and the influence of target material was explored.

I took part in the experiments, contributed to the analysis and the discussion of the results.

XI **Comparison of forward and backward directed beams of low- and medium-mass ions driven by petawatt laser–plasma interactions**

This paper describes results from a heavy-ion acceleration experiment using the Vulcan PW laser and heated targets. Characteristics of the energy spectra and observed ion species, from both the front and back surfaces of the foil targets, are reported. It was found that the front surface ions were superior in both energy and number compared to the back.

I was involved in the setup and execution of the experiment, in particular the parts regarding the Thomson spectrometers. I performed the data analysis and wrote part of the manuscript.

XII **Detection of short lived radioisotopes as a fast diagnostic for intense laser–solid interactions**

A technique for diagnosing laser-accelerated protons using induced activation is described.

I participated in the experiment, which was done in parallel with the ion acceleration experiments reported in papers VIII, IX and XI, and contributed to the discussion in the paper.

XIII **Optimization toward a high-average-brightness soft-x-ray laser pumped at grazing incidence**
Results from the building and optimization of an SXRL, pumped by the Lund multi-TW laser using the GRIP technique, are reported in this paper. High pulse energies of up to $3\,\mu$J were detected.
I was involved in the set-up and execution of all parts of the experiment, and contributed to the manuscript.

XIV **Quantitative study of 10 Hz operation of a soft X-ray laser—energy stability and target considerations**
Results from 10 Hz operation of the SXRL presented in Paper XIII are described. Emphasis is placed on target considerations, detailing laser ablation effects and enhanced laser output after several shots on the same target location.
I took part in the experiment, performed the data analysis and wrote the manuscript.

Acknowledgements

REFERENCES

1. M. Hegelich, S. Karsch, G. Pretzler, D. Habs, K. Witte, W. Guenther, M. Allen, A. Blazevic, J. Fuchs, J. C. Gauthier, M. Geissel, P. Audebert, T. Cowan and M. Roth. *MeV ion jets from short-pulse-laser interaction with thin foils*. Phys. Rev. Lett. **89**, 085002 (2002).

2. T. E. Cowan, J. Fuchs, H. Ruhl, A. Kemp, P. Audebert, M. Roth, R. Stephens, I. Barton, A. Blazevic, E. Brambrink, J. Cobble, J. Fernandez, J.-C. Gauthier, M. Geissel, M. Hegelich, J. Kaae, S. Karsch, G. P. Le Sage, S. Letzring, M. Manclossi, S. Meyroneinc, A. Newkirk, H. Pepin and N. Renard-LeGalloudec. *Ultralow emittance, multi-MeV proton beams from a laser virtual-cathode plasma accelerator*. Phys. Rev. Lett. **92**, 204801 (2004).

3. A. J. Mackinnon, P. K. Patel, R. P. Town, M. J. Edwards, T. Phillips, S. C. Lerner, D. W. Price, D. Hicks, M. H. Key, S. Hatchett, S. C. Wilks, M. Borghesi, L. Romagnani, S. Kar, T. Toncian, G. Pretzler, O. Willi, M. Koenig, E. Martinolli, S. Lepape, A. Benuzzi-Mounaix, P. Audebert, J. C. Gauthier, J. King, R. Snavely, R. R. Freeman and T. Boehlly. *Proton radiography as an electromagnetic field and density perturbation diagnostic (invited)*. Rev. Sci. Instrum. **75**, 3531 (2004).

4. M. Roth, T. E. Cowan, M. H. Key, S. P. Hatchett, C. Brown, W. Fountain, J. Johnson, D. M. Pennington, R. A. Snavely, S. C. Wilks, K. Yasuike, H. Ruhl, F. Pegoraro, S. V. Bulanov, E. M. Campbell, M. D. Perry and H. Powell. *Fast ignition by intense laser-accelerated proton beams*. Phys. Rev. Lett. **86**, 436 (2001).

5. F. F. Chen. *Introduction to plasma physics and controlled fusion*. Kluwer Academic Publishers Group Dordrecht 2nd revised edition (1984).

6. W. Kruer. *The physics of laser plasma interactions*. Westview Press Oxford reprint edition (2003).

7. P. Gibbon. *Short pulse laser interactions with matter: an introduction*. Imperial College Press London (2005).

8. S. Eliezer. *Interaction of high power lasers with plasmas*. Institute of Physics publishing Bristol 1st edition (2001).

9. D. B. Melrose and R. C. McPhedran. *Electromagnetic processes in dispersive media*. Cambridge University Press Cambridge (1991).

10. D. Umstadter. *Review of physics and applications of relativistic plasmas driven by ultra-intense lasers*. In *Phys. Plasmas* volume 8 page 1774 Quebec City, Quebec (Canada) (2001).

11. P. Kaw and J. Dawson. *Relativistic nonlinear propagation of laser beams in cold over-dense plasmas*. Phys. Fluids **13**, 472 (1970).

12. O. Svelto. *Priciples of lasers*. Plenum Press New York 4th edition (1998).

13. D. Strickland and G. Mourou. *Compression of amplified chirped optical pulses*. Opt. Commun. **56**, 219 (1985).

14. E. Treacy. *Optical pulse compression with diffraction gratings*. IEEE J. Quant. Elec. **5**, 454 (1969).

15. S. C. Wilks, A. B. Langdon, T. E. Cowan, M. Roth, M. Singh, S. Hatchett, M. H. Key, D. Pennington, A. MacKinnon and R. A. Snavely. *Energetic proton generation in ultra-intense laser–solid interactions*. Phys. Plasmas **8**, 542 (2001).

16. M. Roth, A. Blazevic, M. Geissel, T. Schlegel, T. E. Cowan, M. Allen, J.-C. Gauthier, P. Audebert, J. Fuchs, J. Meyer ter Vehn, M. Hegelich, S. Karsch and A. Pukhov. *Energetic ions generated by laser pulses: A detailed study on target properties*. Phys. Rev. ST Accel. Beams **5**, 061301 (2002).

17. P. McKenna, K. W. D. Ledingham, I. Spencer, C. Ziener and K. Krushelnick. *Characterization of multiterawatt laser–solid interactions for proton acceleration*. Rev. Sci. Instrum. **73**, 4176 (2002).

18. C. N. Danson, J. Collier, D. Neely, L. J. Barzanti, A. Damerell, C. B. Edwards, M. H. R. Hutchinson, M. H. Key, P. A. Norreys, D. A. Pepler, I. N. Ross, P. F. Taday, W. T. Toner, M. Trentelman, F. N. Walsh, T. B. Winstone and R. W. W. Wyatt. *Well characterized 10^{19} W/cm^2 operation of VULCAN - an ultra-high power Nd:glass laser*. J. Mod. Opt. **45**, 1653 (1998).

19. C. N. Danson, P. A. Brummitt, R. J. Clarke, J. L. Collier, B. Fell, A. J. Frackiewicz, S. Hawkes, C. Hernandez-Gomez, P. Holligan, M. H. R. Hutchinson, A. Kidd, W. J. Lester, I. O. Musgrave, D. Neely, D. R. Neville, P. A. Norreys, D. A. Pepler, C. J. Reason, W. Shaikh, T. B. Winstone, R. W. W. Wyatt and B. E. Wyborn. *Vulcan petawatt: Design, operation and interactions at 5×10^{20} Wcm^{-2}*. Laser Part. Beams **23**, 87 (2005).

20. K. S. Krane. *Introductory nuclear physics*. John Wiley & Sons New York (1988).

21. A. l'Huillier, L. A. Lompre, G. Mainfray and C. Manus. *Multiply charged ions induced by multiphoton absorption processes in rare-gas atoms at $1.064\,\mu m$*. J. Phys. B **16**, 1363 (1983).

22. S. C. Wilks, W. L. Kruer, M. Tabak and A. B. Langdon. *Absorption of ultra-intense laser pulses*. Phys. Rev. Lett. **69**, 1383 (1992).

23. T. W. B. Kibble. *Mutual Refraction of Electrons and Photons*. Phys. Rev. **150**, 1060 (1966).

24. B. Quesnel and P. Mora. *Theory and simulation of the interaction of ultraintense laser pulses with electrons in vacuum*. Phys. Rev. E **58**, 3719 (1998).

25. D. Bauer, P. Mulser and W. H. Steeb. *Relativistic ponderomotive force, uphill acceleration, and transition to chaos*. Phys. Rev. Lett. **75**, 4622 (1995).

26. E. Esarey, P. Sprangle, J. Krall and A. Ting. *Self-focusing and guiding of short laser pulses in ionizing gases and plasmas*. IEEE J. Quant. Elec. **33**, 1879 (1997).

27. W. B. Mori. *The physics of the nonlinear optics of plasmas at relativistic intensities for short-pulse lasers*. IEEE J. Quant. Elec. **33**, 1942 (1997).

28. H. Hora. *Theory of relativistic self-focusing of laser radiation in plasmas*. J. Opt. Soc. Am. **65**, 882 (1975).

29. P. Sprangle, E. Esarey and A. Ting. *Nonlinear theory of intense laser-plasma interactions*. Phys. Rev. Lett. **64**, 2011 (1990).

30. P. Sprangle, E. Esarey and A. Ting. *Nonlinear interaction of intense laser pulses in plasmas*. Phys. Rev. A **41**, 4463 (1990).

31. Z. Najmudin, M. Tatarakis, K. Krushelnick, E. L. Clark, V. Malka, J. Faure and A. E. Dangor. *Ultra-high-intensity laser propagation through underdense plasma.* IEEE Trans. Plasma Sci. **30**, 44 (2002).

32. T. Tajima and J. M. Dawson. *Laser electron accelerator.* Phys. Rev. Lett. **43**, 267 (1979).

33. W. B. Mori, C. D. Decker, D. E. Hinkel and T. Katsouleas. *Raman forward scattering of short-pulse high-intensity lasers.* Phys. Rev. Lett. **72**, 1482 (1994).

34. T. M. Antonsen and P. Mora. *Self-focusing and Raman scattering of laser pulses in tenuous plasmas.* Phys. Rev. Lett. **69**, 2204 (1992).

35. P. Sprangle, E. Esarey, J. Krall and G. Joyce. *Propagation and guiding of intense laser pulses in plasmas.* Phys. Rev. Lett. **69**, 2200 (1992).

36. A. Modena, Z. Najmudin, A. Dangor, C. Clayton, K. A. Marsh, C. Joshi, V. Malka, C. Darrow, C. Danson, D. Neely and F. Walsh. *Electron acceleration from the breaking of relativistic plasma waves.* Nature **377**, 606 (1995).

37. T. Katsouleas and W. B. Mori. *Wave-breaking amplitude of relativistic oscillations in a thermal plasma.* Phys. Rev. Lett. **61**, 90 (1988).

38. S. V. Bulanov, F. Pegoraro, A. M. Pukhov and A. S. Sakharov. *Transverse-wake wave breaking.* Phys. Rev. Lett. **78**, 4205 (1997).

39. C. E. Clayton, M. J. Everett, A. Lal, D. Gordon, K. A. Marsh and C. Joshi. *Acceleration and scattering of Injected electrons in plasma beat-wave accelerator experiments.* Phys. Plasmas **1**, 1753 (1994).

40. S. P. D. Mangles, C. D. Murphy, Z. Najmudin, A. G. R. Thomas, J. L. Collier, A. E. Dangor, E. J. Divall, P. S. Foster, J. G. Gallacher, C. J. Hooker, D. A. Jaroszynski, A. J. Langley, W. B. Mori, P. A. Norreys, F. S. Tsung, R. Viskup, B. R. Walton and K. Krushelnick. *Monoenergetic beams of relativistic electrons from intense laser-plasma interactions.* Nature **431**, 535 (2004).

41. J. Faure, Y. Glinec, A. Pukhov, S. Kiselev, S. Gordienko, E. Lefebvre, J.-P. Rousseau, F. Burgy and V. Malka. *A laser-plasma accelerator producing monoenergetic electron beams.* Nature **431**, 541 (2004).

42. A. G. R. Thomas, Z. Najmudin, S. P. D. Mangles, C. D. Murphy, A. E. Dangor, C. Kamperidis, K. L. Lancaster, W. B. Mori, P. A. Norreys, W. Rozmus and K. Krushelnick. *Effect of laser-focusing conditions on propagation and monoenergetic electron production in laser-wakefield accelerators.* Phys. Rev. Lett. **98**, 095004 (2007).

43. A. Pukhov and J. Meyer-ter Vehn. *Laser wake field acceleration: the highly non-linear broken-wave regime.* Appl. Phys. B: Lasers Opt. **V74**, 355 (2002).

44. R. A. Fonseca, L. O. Silva, F. S. Tsung, V. K. Decyk, W. Lu, C. Ren, W. B. Mori, S. Deng, S. Lee, T. Katsouleas and J. C. Adam. *OSIRIS: A three-dimensional, fully relativistic particle in cell code for modeling plasma based accelerators.* Springer Berlin / Heidelberg (2002).

45. V. Malka, C. Coulaud, J. P. Geindre, V. Lopez, Z. Najmudin, D. Neely and F. Amiranoff. *Characterization of neutral density profile in a wide range of pressure of cylindrical pulsed gas jets.* Rev. Sci. Instrum. **71**, 2329 (2000).

46. T. R. Clark and H. M. Milchberg. *Time-evolution and guiding regimes of the laser-produced plasma waveguide.* Phys. Plasmas **7**, 2192 (2000).

47. J. J. Thomson. *Conduction of electricity through gases.* Cambridge University Press Cambridge (1906).

48. Y. Glinec, J. Faure, A. Guemnie-Tafo, V. Malka, H. Monard, J. P. Larbre, V. De Waele, J. L. Marignier and M. Mostafavi. *Absolute calibration for a broad range single shot electron spectrometer.* Rev. Sci. Instrum. **77**, 103301 (2006).

49. S. C. Wilks, J. M. Dawson, W. B. Mori, T. Katsouleas and M. E. Jones. *Photon accelerator.* Phys. Rev. Lett. **62**, 2600 (1989).

50. J. M. Dias, L. Oliveira e Silva and J. T. Mendona. *Photon acceleration versus frequency-domain interferometry for laser wakefield diagnostics.* Phys. Rev. ST Accel. Beams **1**, 031301 (1998).

51. T. Grismayer and P. Mora. *Influence of a finite initial ion density gradient on plasma expansion into a vacuum.* Physics Of Plasmas **13**, 032103 (2006).

52. R. A. Snavely, M. H. Key, S. P. Hatchett, T. E. Cowan, M. Roth, T. W. Phillips, M. A. Stoyer, E. A. Henry, T. C. Sangster, M. S. Singh, S. C. Wilks, A. MacKinnon, A. Offenberger, D. M. Pennington, K. Yasuike, A. B. Langdon, B. F. Lasinski, J. Johnson, M. D. Perry and E. M. Campbell. *Intense high-energy proton beams from petawatt-laser irradiation of solids.* Phys. Rev. Lett. **85**, 2945 (2000).

53. F. N. Beg, A. R. Bell, A. E. Dangor, C. N. Danson, A. P. Fews, M. E. Glinsky, B. A. Hammel, P. Lee, P. A. Norreys and M. Tatarakis. *A study of picosecond laser–solid interactions up to $10^{19}~W~cm^{-2}$.* Phys. Plasmas **4**, 447 (1997).

54. M. I. K. Santala, M. Zepf, I. Watts, F. N. Beg, E. Clark, M. Tatarakis, K. Krushelnick, A. E. Dangor, T. McCanny, I. Spencer, R. P. Singhal, K. W. D. Ledingham, S. C. Wilks, A. C. Machacek, J. S. Wark, R. Allott, R. J. Clarke and P. A. Norreys. *Effect of the plasma density scale length on the direction of fast electrons in relativistic laser–solid interactions.* Phys. Rev. Lett. **84**, 1459 (2000).

55. F. Brunel. *Not-so-resonant, resonant absorption.* Phys. Rev. Lett. **59**, 52 (1987).

56. J. Yu, Z. Jiang, J. C. Kieffer and A. Krol. *Hard X-ray emission in high intensity femtosecond laser–target interaction.* Phys. Plasmas **6**, 1318 (1999).

57. F. Brandl, G. Pretzler, D. Habs and E. Fill. *Cerenkov radiation diagnostics of hot electrons generated by fs-laser interaction with solid targets.* Europhys. Lett. **61**, 632 (2003).

58. P. K. Patel, A. J. Mackinnon, M. H. Key, T. E. Cowan, M. E. Foord, M. Allen, D. F. Price, H. Ruhl, P. T. Springer and R. Stephens. *Isochoric heating of solid-density matter with an ultrafast proton beam.* Phys. Rev. Lett. **91**, 125004 (2003).

59. A. J. Mackinnon, Y. Sentoku, P. K. Patel, D. W. Price, S. Hatchett, M. H. Key, C. Andersen, R. Snavely and R. R. Freeman. *Enhancement of proton acceleration by hot-electron recirculation in thin foils irradiated by ultraintense laser pulses.* Phys. Rev. Lett. **88**, 215006 (2002).

60. Y. Sentoku, T. E. Cowan, A. Kemp and H. Ruhl. *High energy proton acceleration in interaction of short laser pulse with dense plasma target.* Phys. Plasmas **10**, 2009 (2003).

61. M. Kaluza, J. Schreiber, M. I. K. Santala, G. D. Tsakiris, K. Eidmann, J. Meyer-ter Vehn and K. J. Witte. *Influence of the laser prepulse on proton acceleration in thin-foil experiments.* Phys. Rev. Lett. **93**, 045003 (2004).

62. B. M. Hegelich, B. Albright, P. Audebert, A. Blazevic, E. Brambrink, J. Cobble, T. Cowan, J. Fuchs, J. C. Gauthier, C. Gautier, M. Geissel, D. Habs, R. Johnson, S. Karsch, A. Kemp, S. Letzring, M. Roth, U. Schramm, J. Schreiber, K. J. Witte and J. C. Fernandez. *Spectral properties of laser-accelerated mid-Z MeV/u ion beams.* Phys. Plasmas **12**, 056314 (2005).

63. D. C. Swift, T. E. Tierney IV, R. A. Kopp and J. T. Gammel. *Shock pressures induced in condensed matter by laser ablation.* Phys. Rev. E **69**, 036406 (2004).

64. R. Grover and P. A. Urtiew. *Thermal relaxation at interfaces following shock compression.* J. Appl. Phys. **45**, 146 (1974).

65. C. Dai, H. Tan and H. Geng. *Model for assessing the melting on Hugoniots of metals: Al, Pb, Cu, Mo, Fe, and U.* J. Appl. Phys. **92**, 5019 (2002).

66. R. Ramis, R. Schmalz and J. Meyer-Ter-Vehn. *MULTI – A computer code for one-dimensional multigroup radiation hydrodynamics.* Comput. Phys. Commun. **49**, 475 (1988).

67. A. J. Kemp and J. Meyer-ter Vehn. *An equation of state code for hot dense matter, based on the QEOS description.* Nucl. Inst. Meth. A **415**, 674 (1998).

68. H. C. Kapteyn, M. M. Murnane, A. Szoke and R. W. Falcone. *Prepulse energy suppression for high-energy ultrashort pulses using self-induced plasma shuttering.* Opt. Lett. **16**, 490 (1991).

69. Ch. Ziener, P. S. Foster, E. J. Divall, C. J. Hooker, M. H. R. Hutchinson, A. J. Langley and D. Neely. *Specular reflectivity of plasma mirrors as a function of intensity, pulse duration, and angle of incidence.* J. Appl. Phys. **93**, 768 (2003).

70. G. Doumy, F. Quere, O. Gobert, M. Perdrix, Ph. Martin, P. Audebert, J. C. Gauthier, J.-P. Geindre and T. Wittmann. *Complete characterization of a plasma mirror for the production of high-contrast ultraintense laser pulses.* Phys. Rev. E **69**, 026402 (2004).

71. V. T. Tikhonchuk. *Interaction of a beam of fast electrons with solids.* Phys. Plasmas **9**, 1416 (2002).

72. PSTAR database at NIST (2007). URL http://www.physics.nist.gov/PhysRefData/Star/Text/PSTAR.html.

73. PPG website on CR-39 (2007). URL http://corporateportal.ppg.com/NA/chemicals/Optical/CR39/cr39History.htm.

74. D. L. Henshaw. *Applications of CR-39 nuclear track detector in medicine and technology.* Phys. Tech. **13**, 266 (1982).

75. F. H. Seguin, J. A. Frenje, C. K. Li, D. G. Hicks, S. Kurebayashi, J. R. Rygg, B.-E. Schwartz, R. D. Petrasso, S. Roberts, J. M. Soures, D. D. Meyerhofer, T. C. Sangster, J. P. Knauer, C. Sorce, V. Yu. Glebov, C. Stoeckl, T. W. Phillips, R. J. Leeper, K. Fletcher and S. Padalino. *Spectrometry of charged particles from inertial-confinement-fusion plasmas.* Rev. Sci. Instrum. **74**, 975 (2003).

76. S. Kar, M. Borghesi, L. Romagnani, S. Takahashi, A. Zayats, V. Malka, S. Fritzler and A. Schiavi. *Analysis of latent tracks for MeV protons in CR-39.* J. Appl. Phys. **101**, 044510 (2007).

77. S. Gaillard, J. Fuchs, N. Renard-Le Galloudec and T. E. Cowan. *Study of saturation of CR39 nuclear track detectors at high ion fluence and of associated artifact patterns.* Rev. Sci. Instrum. **78**, 013304 (2007).

78. W. L. McLaughlin, J. M. Puhl, M. Al-Sheikhly, C. A. Christou, A. Miller, A. Kovcs, L. Wojnarovits and D. F. Lewis. *Novel radiochromic films for clinical dosimetry.* Radiat. Prot. Dosimetry **66**, 263 (1996).

79. H. Schwoerer, S. Pfotenhauer, O. Jackel, K.-U. Amthor, B. Liesfeld, W. Ziegler, R. Sauerbrey, K. W. D. Ledingham and T. Esirkepov. *Laser-plasma acceleration of quasi-monoenergetic protons from microstructured targets.* Nature **439**, 445 (2006).

80. J. J. Thomson. Philos. Mag. **21** (1911).

81. D. C. Carroll, K. Jones, L. Robson, P. McKenna, S. Bandyopadhyay, P. Brummitt, D. Neely, F. Lindau, O. Lundh and C.-G. Wahlström. The design, development and use of a novel Thomson spectrometer for high resolution ion detection. Central laser facility annual report SUPA, Department of Physics, University of Strathclyde, Glasgow, UK (2006).

82. E. d'Humieres, E. Lefebvre, L. Gremillet and V. Malka. *Proton acceleration mechanisms in high-intensity laser interaction with thin foils.* Phys. Plasmas **12**, 062704 (2005).

83. J. Fuchs, P. Antici, E. D'Humieres, E. Lefebvre, M. Borghesi, E. Brambrink, C. A. Cecchetti, M. Kaluza, V. Malka, M. Manclossi, S. Meyroneinc, P. Mora, J. Schreiber, T. Toncian, H. Pepin and R. Audebert. *Laser-driven proton scaling laws and new paths towards energy increase.* Nat. Phys. **2**, 48 (2006).

84. P. Mora. *Plasma expansion into a vacuum.* Phys. Rev. Lett. **90**, 185002 (2003).

85. P. Mora. *Thin-foil expansion into a vacuum.* Phys. Rev. E **72**, 056401 (2005).

86. T. A. Carlson, C. W. Nestor, Jr., N. Wasserman and J. D. McDowell. *Calculated ionization potentials for multiply charged ions.* At. Data **2**, 63 (1970).

87. A. P. L. Robinson. Private communication (2007).

88. D. L. Matthews, P. L. Hagelstein, M. D. Rosen, M. J. Eckart, N. M. Ceglio, A. U. Hazi, H. Medecki, B. J. MacGowan, J. E. Trebes, B. L. Whitten, E. M. Campbell, C. W. Hatcher, A. M. Hawryluk, R. L. Kauffman, L. D. Pleasance, G. Rambach, J. H. Scofield, G. Stone and T. A. Weaver. *Demonstration of a Soft X-Ray amplifier.* Phys. Rev. Lett. **54**, 110 (1985).

89. H. Daido. *Review of soft X-ray laser researches and developments.* Rep. Prog. Phys. **65**, 1513 (2002).

90. J. J. Rocca. *Table-top soft X-ray lasers.* Rev. Sci. Instrum. **70**, 3799 (1999).

91. Y. Li, J. Nilsen, J. Dunn, A. L. Osterheld, A. Ryabtsev and S. Churilov. *Wavelengths of the Ni-like $4d^1S_0 - 4p^1P_1$ x-ray laser line.* Phys. Rev. A **58**, R2668 (1998).

92. B. J. MacGowan, S. Maxon, L. B. Da Silva, D. J. Fields, C. J. Keane, D. L. Matthews, A. L. Osterheld, J. H. Scofield, G. Shimkaveg and G. F. Stone. *Demonstration of X-ray amplifiers near the carbon K edge.* Phys. Rev. Lett. **65**, 420 (1990).

93. P. V. Nickles, V. N. Shlyaptsev, M. Kalachnikov, M. Schnrer, I. Will and W. Sandner. *Short pulse X-ray laser at 32.6 nm based on transient gain in Ne-like titanium.* Phys. Rev. Lett. **78**, 2748 (1997).

94. R. Keenan, J. Dunn, P. K. Patel, D. F. Price, R. F. Smith and V. N. Shlyaptsev. *High-repetition-rate grazing-incidence pumped X-ray laser operating at 18.9 nm.* Phys. Rev. Lett. **94**, 103901 (2005).

95. G. J. Pert. *Optimizing the performance of nickel-like collisionally pumped x-ray lasers.* Phys. Rev. A **73**, 033809 (2006).

96. B. M. Luther, Y. Wang, M. A. Larotonda, D. Alessi, M. Berrill, J. J. Rocca, J. Dunn, R. Keenan and V. N. Shlyaptsev. *High repetition rate collisial soft X-ray lasers based on grazing incidence pumping.* IEEE J. Quant. Elec. **42**, 4 (2006).

97. Center for X-ray optics website (2007). URL http://www-cxro.lbl.gov/optical_constants/.

98. J. G. Lunney. *Waveguiding in soft X-ray laser experiments.* Appl. Phys. Lett. **48**, 891 (1986).

99. W. P. Leemans, B. Nagler, A. J. Gonsalves, C. Toth, K. Nakamura, C. G. R. Geddes, E. Esarey, C. B. Schroeder and S. M. Hooker. *GeV electron beams from a centimetre-scale accelerator.* Nat. Phys. **2**, 696 (2006).

100. A. Rousse, K. T. Phuoc, R. Shah, A. Pukhov, E. Lefebvre, V. Malka, S. Kiselev, F. Burgy, J.-P. Rousseau, D. Umstadter and D. Hulin. *Production of a keV X-ray beam from synchrotron radiation in relativistic laser–plasma interaction.* Phys. Rev. Lett. **93**, 135005 (2004).

101. K. T. Phuoc, F. Burgy, J.-P. Rousseau, V. Malka, A. Rousse, R. Shah, D. Umstadter, A. Pukhov and S. Kiselev. *Laser based synchrotron radiation.* Phys. Plasmas **12**, 023101 (2005).

102. B. M. Hegelich, B. J. Albright, J. Cobble, K. Flippo, S. Letzring, M. Paffett, H. Ruhl, J. Schreiber, R. K. Schulze and J. C. Fernndez. *Laser acceleration of quasi-monoenergetic MeV ion beams.* Nature **439**, 441 (2006).

103. T. Esirkepov, M. Yamagiwa and T. Tajima. *Laser ion-acceleration scaling laws seen in multiparametric particle-in-cell simulations.* Phys. Rev. Lett. **96**, 105001 (2006).

104. C. M. Ma, I. Veltchev, E. Fourkal, J. S. Li, W. Luo, J. Fan, T. Lin and A. Pollack. *Development of a laser-driven proton accelerator for cancer therapy.* Laser Phys. **16**, 639 (2006).

105. P. Zeitoun, G. Faivre, S. Sebban, T. Mocek, A. Hallou, M. Fajardo, D. Aubert, P. Balcou, F. Burgy, D. Douillet, S. Kazamias, G. de Lacheze-Murel, T. Lefrou, S. le Pape, P. Mercere, H. Merdji, A. S. Morlens, J. P. Rousseau and C. Valentin. *A high-intensity highly coherent soft X-ray femtosecond laser seeded by a high harmonic beam.* Nature **431**, 426 (2004).

106. Y. Wang, E. Granados, M. A. Larotonda, M. Berrill, B. M. Luther, D. Patel, C. S. Menoni and J. J. Rocca. *High-brightness injection-seeded soft-X-ray-laser amplifier using a solid target.* Phys. Rev. Lett. **97**, 123901 (2006).